Relocating Earthquakes using Seismic Networks on Small Islands: Case Studies from Heimaey (Iceland) and Jan Mayen (Norway)

by
Robin André Rørstadbotnen

Thesis for the degree
Master of Science in Geodynamics

Department of Geoscienses
University of Bergen

August 2019

Abstract

The main objective of this thesis is to study different aspects of solving the earthquake location problem and to investigate difficulties in locating earthquakes with sparse networks. This was done by using different velocity models, various ray tracing algorithms, and different location procedures at sparse oceanic island stations. The aim is to investigate how all these factors affect the solution to the earthquake location problem on the two islands Heimaey (Iceland) and Jan Mayen (Norway).

Finding the answer to this research question required that work was carried out through different steps. First, a temporary seismic network was installed on Heimaey. After this, noise analysis and a detection algorithm were applied to the recorded data. Because too few events were recorded on Heimaey, a new data-set from Jan Mayen was included in the research. The data was preprocessed, i.e., arrival times of P- and S-phases were selected in SEISAN. Subsequently, ray tracing algorithms were written for the different velocity models in the two regions. This was done by solving the ray equations numerically using the modified Euler method for the smooth models and using Snell's law for the discontinuous layered velocity model. Two different grid search methods were implemented to solve the earthquake location problem. The first method is called the single-difference grid search method. A traditional grid search method was implemented for comparison. The traditional grid search method uses calculated travel times and origin times to estimate the earthquake hypocenter, whereas the single-difference only requires travel time differences. The relocations obtained from these methods are compared to the catalog locations found by the HYPOCENTER location program available in SEISAN. In addition, the grid search methods can be used in uncertainty analyses. This is illustrated for a few events. Finally, a new velocity model for Jan Mayen, which was obtained from a 2D velocity profile in the literature, was tested.

The arrival time picks of the Jan Mayen data-set were used to relocate 259 events observed after the magnitude 6.7 earthquake on November 9, 2018, and two before. The main result from the relocations was that most events were concentrated in six swarms localized along the fracture zone. These swarms were not as clear after applying the standard HYPOCENTER algorithm in SEISAN. The grid search methods localizes the events more to the Jan Mayen Transform Fault north of Jan Mayen. The location and timing

of one of the swarms north-west of Jan Mayen suggests that the main event triggered it. The seismic activity along the fault returns to regular background seismicity after approximately one month. The ray tracing algorithm for the new 3D velocity model was used to relocate one of the swarms using the two grid search methods. These relocations estimated the swarm further away from the fracture zone, some kilometers south-west compared to the catalog locations. This deviation was probably caused by inaccuracies in the velocity model.

Acknowledgements

First, I would like to thank my supervisors at the University of Bergen, Lars Ottemöller, for all good the guidance and feedback during my thesis work. I would also like to thank my co-supervisors at the University of Bergen, Henk Keers, for his guidance, feedback, and teaching on the different theories needed for this thesis. The thesis could not have been written without your help.

Further, I would like to thank my second co-supervisor Kristín Vogfjörd for her help with the installation of the seismic network on Heimaey and her suggestions for interesting research ideas.

All my friends from university have been important when writing this thesis. The activities that we have done during this year at the university have made my time as a student really enjoyable. A special thanks to the "Utrecht Unicorn bois". The semester abroad was truly unforgettable, and I am looking forward to future adventures with you.

I would also like to express gratitude to my family, who is always there for me.

Finally, I would like to express a special thanks to Tora Haugen Myklebust. You have helped me relax during these stressful times, and helped me through some really tough days.

Contents

List of Figures

List of Tables

Chapter 1

Introduction

1.1 Motivation and Objective

The study of earthquakes is necessary to better understand the physical properties of the subsurface. Earthquakes typically occur in the lithosphere and are generally the result of plate motions. In some cases, however, earthquakes are triggered by volcanism. Analysis of earthquake recurrence and interactions can, therefore, provide valuable information on tectonic and volcanic processes [(Waldhauser and Ellsworth, 2000); (Stein and Wysession, 2003)]. Accurate knowledge of hypocenter locations is essential in such seismicity analyses because the location uncertainty of routinely determined hypocenters usually is larger than the source dimension of the events itself. This puts limits on the study of seismicity. The aim of this thesis is, therefore, to investigate different methods to estimate earthquake locations, as well as providing uncertainty analyses for these. The earthquake location methods are applied to data collected from seismic stations on two volcanic islands: Heimaey (Iceland) and Jan Mayen (Norway). Both islands are located on the Mid-Atlantic Ridge [(Havskov and Atakan, 1991); (Mattsson and Höskuldsson, 2003)].

The original aim of the thesis was to investigate the seismic activity related to the active volcano Eldfell on Heimaey. To be able to estimate more reliable hypocenter locations on Heimaey, the seismic network on the island was extended. The Icelandic Meteorological Office (IMO) had three stations operational on the island. Five additional stations owned

by the University of Bergen (UoB) were installed on Heimaey. The installation process was executed in collaboration with staff from IMO. However, only six events were recorded during the deployment period, and only two of these were of high enough quality for further analysis. None of these were related to Eldfell. Because of the lack of seismic activity on Heimaey, the focus of the thesis changed from deployment to development of methodology. For this new goal, additional data were required. Therefore 262 events recorded from November 2018 to May 2019 near Jan Mayen were included. The Jan Mayen data were included, because of its similarities to the Heimaey data. The stations are located in a small noisy island environment, and events occur outside the network in the oceanic crust.

Relocating earthquakes near Heimaey and Jan Mayen are interesting because previous attempts to locate the earthquakes contain uncertainties. For instance, data from Jan Mayen show outliers south of the island, while the fracture zone is known to be north of the island. On Heimaey, it appears that with the IMO network the hypocenters are located west of Heimaey. This is curious as the waves appear to come from the east and there is a volcanic fissure along the eastern side of Heimaey.

Two different grid search methods are implemented to more accurately locate the events. These will be introduced as the traditional grid search method and the single-difference grid search method. The grid search methods also provide additional tools for uncertainty analysis. For the relocation on Heimaey and Jan Mayen, 1D velocity models will be used. In addition, a new velocity model for Jan Mayen, from a 2D velocity profile given by Kandilarov et al. (2012), is used. The relocations procedures include implementing ray tracing algorithms for the different velocity models and applying the estimated travel times to the grid search methods.

1.2 Outline

The work performed in this thesis is presented in eight chapters. In chapter 2, an overview of the geological background, including the main tectonic features and the historical seismicity of the survey areas, is given. Subsequently, the seismic networks on Heimaey and Jan Mayen are introduced in Chapter 3. The main focus of the chapter will, however,

be on the installation process of the Heimaey network and the recorded data. After this, Chapter 4 introduces the methodology used to do ray tracing. This is followed by the methodology for the earthquake location procedures in Chapter 5. Chapter 5 also includes synthetic tests for the two grid search methods. The real data application, where the different relocation results are presented, is described in Chapter 6. In Chapter 7, a discussion on the different results is given. Chapter 8 provides the conclusion of the thesis work.

Chapter 2

Seismicity and Tectonic frame work - Heimaey and Jan Mayen

This chapter gives background information on Heimaey and Jan Mayen. The background information presents the geological setting, including the main tectonic features, and the historical seismicity. Heimaey is discussed in the first section, followed by Jan Mayen in the final section.

2.1 Heimaey

Iceland is located on the assemblage of the Iceland mantle plume and the Mid-Atlantic Ridge (MAR), a divergent plate boundary moving WNW relative to the mantle plume [e.g. (Lawver and Muller, 1994); (Stein and Stein, 2003); (Mattsson and Höskuldsson, 2003)]. The WNW motion causes periodic relocation of the main rift axis, and the most recent relocation is called the Easter Volcanic Zone (EVZ) [(Sæmundsson, 1974); (Jóhannesson, 1980); (Hardarson et al., 1997)]. The EVZ comprises nine volcanic systems, all of which are seen in Figure 2.1. Heimaey is part of the southernmost volcanic system, also referred to as the Vestmannaeyjar Volcanic System (VVS), and represents the center of volcanism in the system. The volcanic island is located 10 km outside the southern Icelandic coast (Mattsson and Höskuldsson, 2003).

The VVS contains 17 islands and covers approximately 850 km^2 of the southern coast of

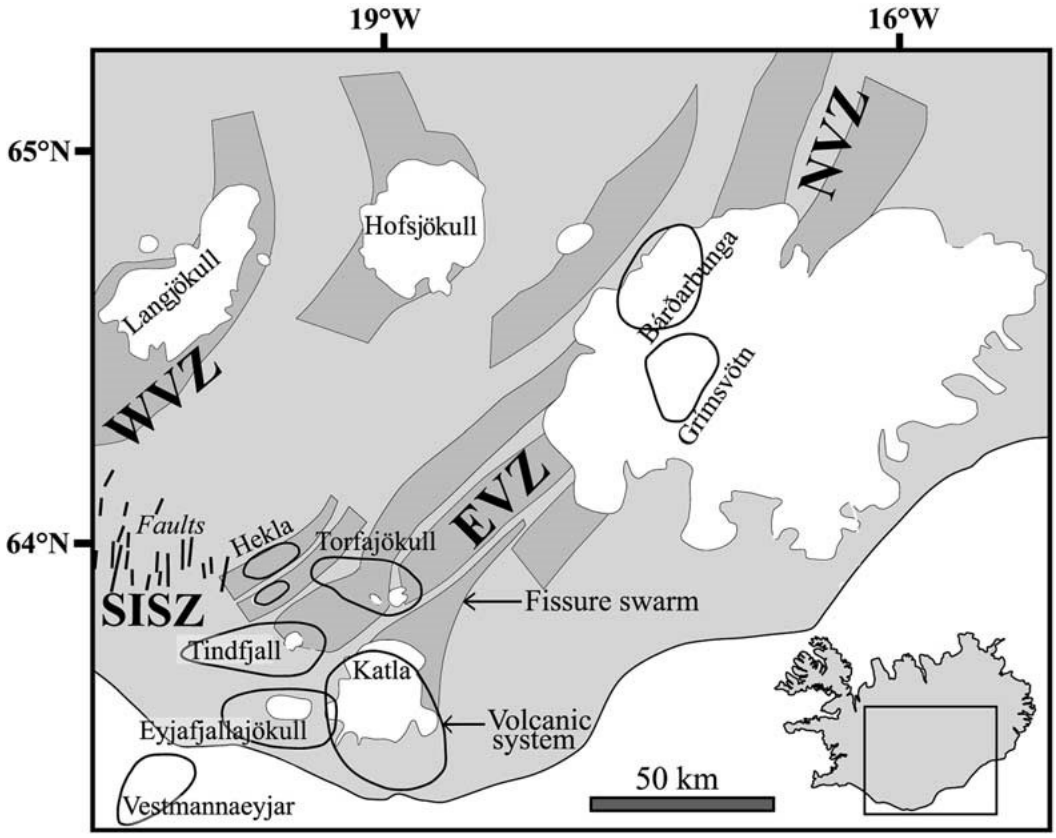

Figure 2.1: Map of the nine volcanic systems in Iceland (indicated by rings), with Bárdabunga in the North and Vestmannaeyjar to the South-West. SISZ = South Island Seismic Zone, WVZ = Western Volcanic Zone, NVZ = Northern Volcanic Zone, EVZ = Eastern Volcanic Zone. (Mattsson and Höskuldsson, 2003)

Iceland (indicated with a red circle in Figure 2.2a). Eruptions in the volcanic system are generally of small volume, on average 0.17 km^3 originating from monogenetic vents, i.e. vents are erupting only once (Mattsson and Höskuldsson, 2003).

2.1.1 Geological setting

Heimaey is the largest of the 17 islands in the VVS. Figure 2.3 shows different eruption sites on Heimaey. These volcanoes started forming underwater through phreatomagmatic volcanic activities, which formed tuff cones or tuff rings. Later, the eruptions shifted to effusive as the vents raised above sea level and were no longer affected by seawater [(Jakobsson, 1968); (Jakobsson et al., 1979); (Mattsson and Höskuldsson, 2003)].

Heimaey can be divided into five geological units. It is clear from Figures 2.3 and 2.4 that

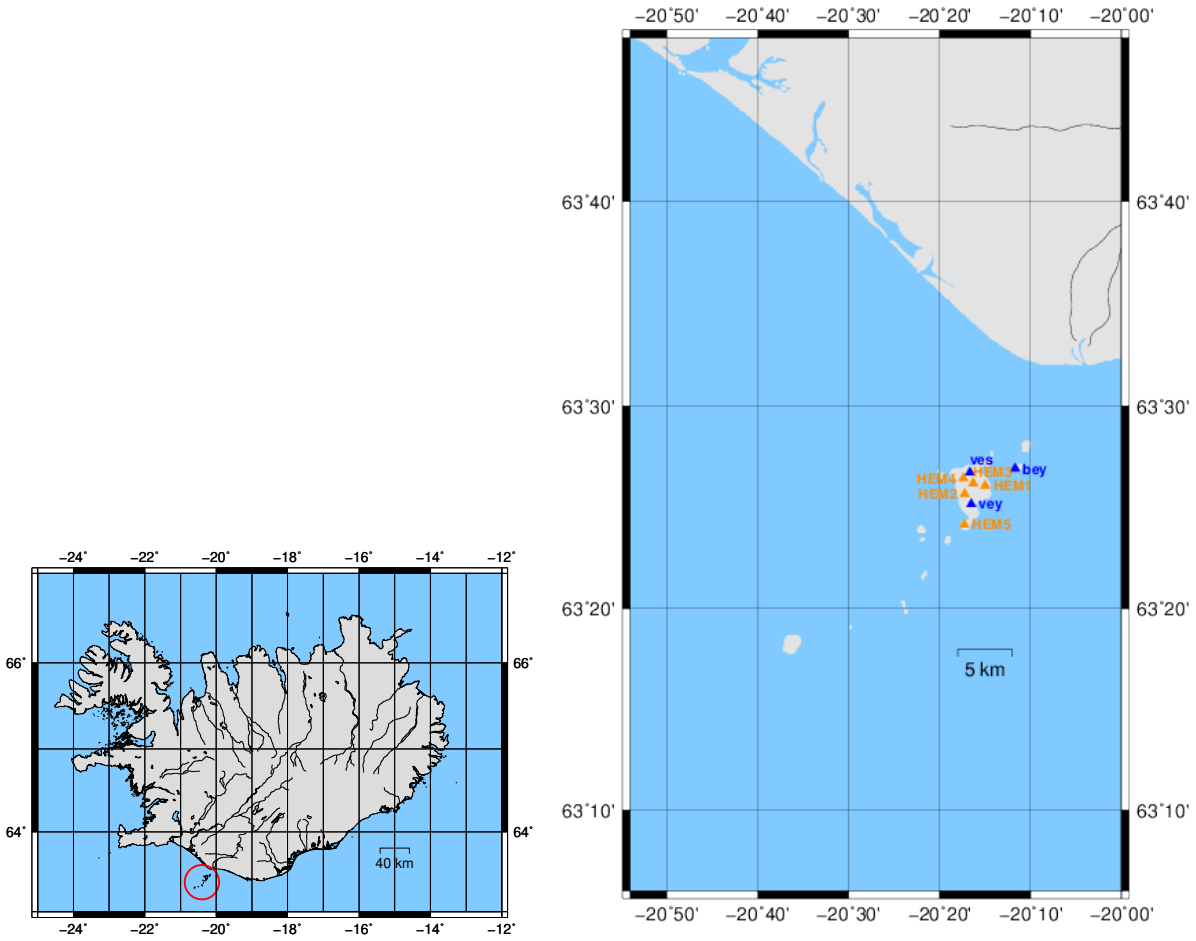

(a) Map of Iceland, red circle shows the location of Vestmannaeyjar.

(b) Map of the Vestmannaeyjar volcanic zone. Blue triangles indicate IMO stations, and the UoB stations are orange (for details of the map see Figure 3.1a).

Figure 2.2: Map of Iceland (a) and a schematic map over Vestmannaeyjar (b).

the geological units coincide with different eruption sites.

To the north is the Nordurklettar formation, which was formed from 6-7 different eruptions and rises 280 meters above sea level (m.a.s.l). This is the oldest unit and the first to rise above sea level (Mattsson and Höskuldsson, 2003).

The Helgafell (228 m.a.s.l) and the Eldfell cone (223 m.a.s.l), in addition to Norduklettar, are the most dominant geological structures of the island. The geological units created by eruptions from the former two volcanoes cover approximately 80% of the island's topography. Helgafell's lava flows, which are 6000 years old, are found in the center and

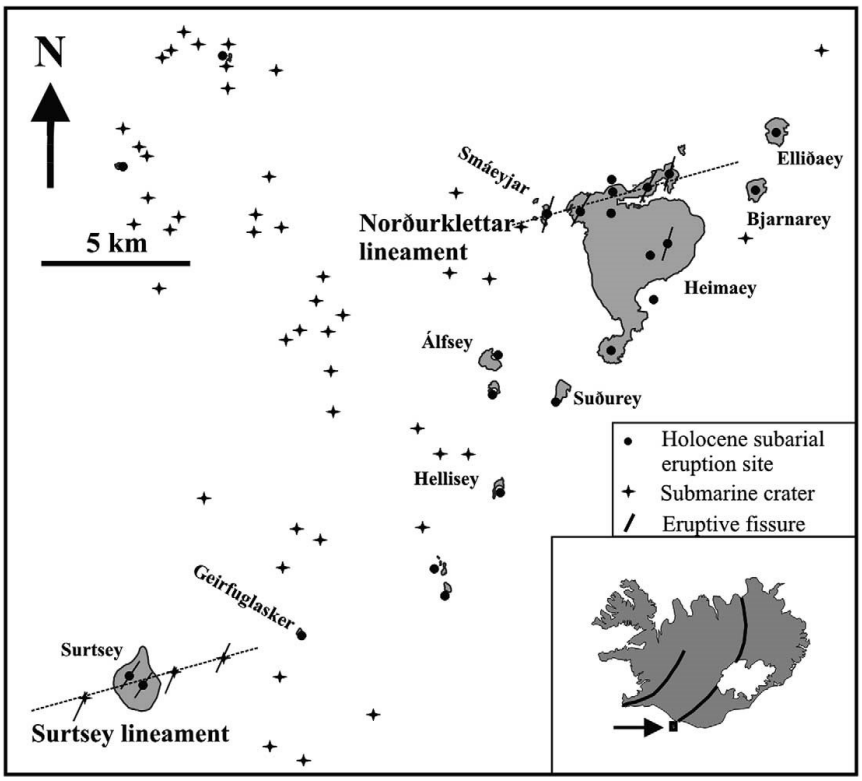

Figure 2.3: Schematic map of different tectonic features in the Vestmannaeyjar volcanic system (Mattsson and Höskuldsson, 2003).

to the west of the island. Eldfell's lava flows, formed 46 years ago, are located in the east and represents the most recent eruption.

A fourth unit is the Sæfell tuff ring (188 m.a.s.l.), created by the Sæfell eruption around 5500 years ago. The Sæfell lava has been subjected to significant marine abrasion, and it is believed that only 50% of the rock remains.

The southernmost geological formation is the Stórhofdi lava. Mattsson and Höskuldsson (2003) believe this geological feature to be slightly older than the Sæfell unit.

Surtsey is the second-largest island in the Vestmannaeyjar volcanic zone. Numerous eruptions from the Surtsey fissures created this island, which is located approximately 22 km south-west of Heimaey. Surtsey started forming in early November 1963 at 130 meters depth. A short submarine fissure raised Surtsey from the ocean floor to breach the surface, on November 14 the same year. The eruptions lasted for about 3.5 years through five different vents. The eruptions ended in mid-1967 and formed an island of approximately 1.4 km^2 (Schipper et al., 2015).

2.1.2 Tectonic Features

Mattsson and Höskuldsson (2003) argued that several of the islands in the Vestmannaeyjar volcanic system are arranged with an N45°E trend, similar to the trend of EVZ seen in Figure 2.1. Figure 2.3 shows that four of the eruptive units on Heimaey also follow this north-east trend. In addition, the figure shows that the Nordurkletta formation and the Surtsey fissures have similar en échelon arrangement. A third observation is that the Heimaey eruptions develop along two main lineaments: The first is the Stórhofdi-Eldfell lineament, which has an N45°E trend. The second Norduklettare lineament trends N65°E.

From distance measurements across the Eldfell's eruptive fissure, planes of maximum compression have been found to be almost identical to the general trend of the EVZ and that fissures are formed due to shear movements (Brander and Wadge, 1973). Later, Sæmundsson (1979) argued that the southernmost part of the EVZ might be a result of sinistral movement, with maximum compression oriented N45°E and the axis of maximum tension subparallel to the spreading direction, i.e., NW-SE.

2.1.3 Seismicity

Figure 2.5 shows the two main areas of seismicity in the Vestmannaeyjar volcanic system. The first is east of Heimaey and the second is north of Surtsey. The largest event occurred north of Surtsey September 2, 1992, with a local magnitude of 3.4. These regions of seismicity are most likely related to the main tectonic features in the vicinity of the islands. The seismicity outside of these regions might be related to smaller tectonic units. The activity may suggest the development of new tectonic structures. It is also possible that the location procedures and the lack of station coverage cause considerable uncertainty in the epicenter location. The location uncertainty might explain the spread in the data and the outliers found over the volcanic system.

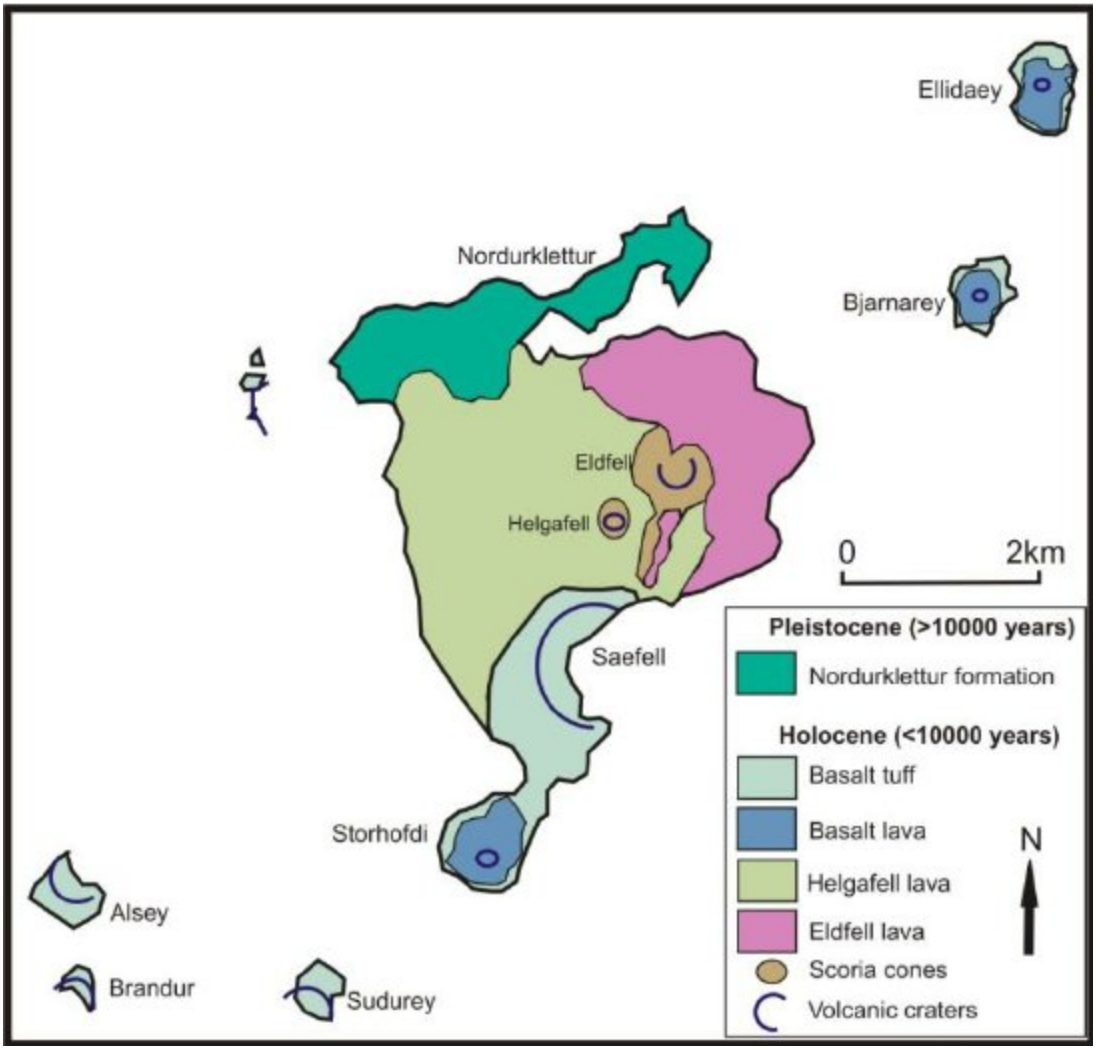

Figure 2.4: Geological map of Heimaey (Andrew et al., 2008).

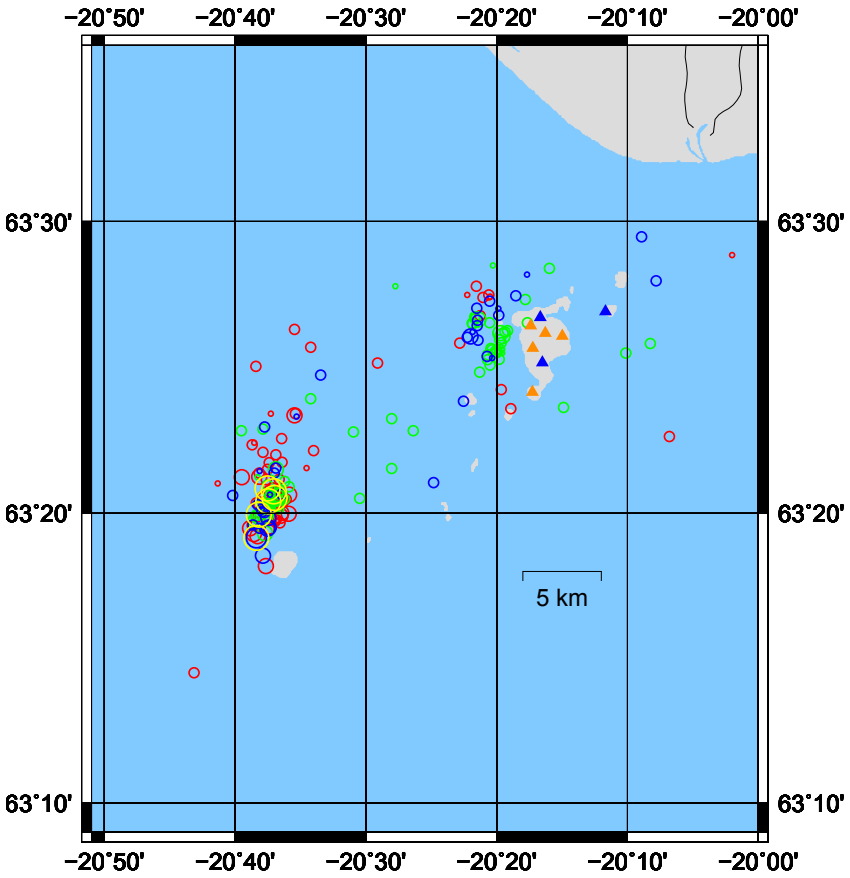

Figure 2.5: Seismicity in the vicinity of Heimaey, from 1991 to 2019. Red circles indicate events that occurred between 1991 and 1999, green circles between 2000 and 2009, and blue circles between 2010 and 2017. The yellow circles indicate events that occurred during the deployment of the seismic network (Oct 2017 - March 2019). The sizes of the circles indicate the magnitude of the events, where the biggest circles corresponds to events with M $>$ 3.0, and the smallest events corresponds to events with, M $<$ 1.0. The orange (UoB) and blue (IMO) triangles indicate the position of the seismic stations (see Figure 3.1a for a detailed station map).

2.2 Jan Mayen

Jan Mayen is a small island (320 km^2) located at the northern mid-Atlantic ridge, where the North American and the Eurasian plates diverge. The Norwegian volcanic island is located between Greenland and Norway (71°N, 8°W), and was created by the world's northernmost active volcano, Beerenberg (2277 m). It is built entirely by volcanic rock younger than 0.7 Myr old (Havskov and Atakan, 1991).

The northernmost tip of Jan Mayen is located at the Jan Mayen Fracture Zone (JMFZ). The JMFZ connects laterally two spreading ridges, the Mohns ridge to the north-east and the Kolbeinsey ridge to the south-west. These two ridges are spreading at a rate of 15-17 mm/yr.

Jan Mayen can also be described as being located at the northern end of the Jan Mayen Ridge (JMR). This can be considered to be a microcontinent, the Jan Mayen Micro-Continent (JMMC), [e.g. (Sylvester, 1975); (Myhre et al., 1984), (Kodaira et al., 1998); (Sørensen et al., 2007)]. It is most likely a detached relic of the Greenland continental rise [(Johnson and Heezen, 1967); (Talwani and Eldholm, 1977)]. Thus, the Jan Mayen region has a complex subsurface structure.

2.2.1 Seismicity

The region is affected by a high seismicity rate, with the occurrence of both tectonic and volcanic events (Rodríguez-Pérez and Ottemöller, 2014). Figure 2.6 shows the distribution of earthquakes recorded between 1901 and 2013 by the Norwegian National Seismic Network (NNSN). It also shows that historic events coincide with the tectonic features of the MAR and the JMFZ. In addition, the figure shows scatter in epicenters, indicating uncertainties in the earthquake locations.

Beerenberg has had several eruptions through historical time. The earliest directly observed eruption was in 1650. The three most recent eruptions were in September 1970, January 1972, and January 1985 (Havskov and Atakan, 1991). Sørensen et al. (2007) argued that low-frequency volcanic events from the January 1985 event had waveforms different from the tectonic waveforms in the area, and are therefore easily identified and

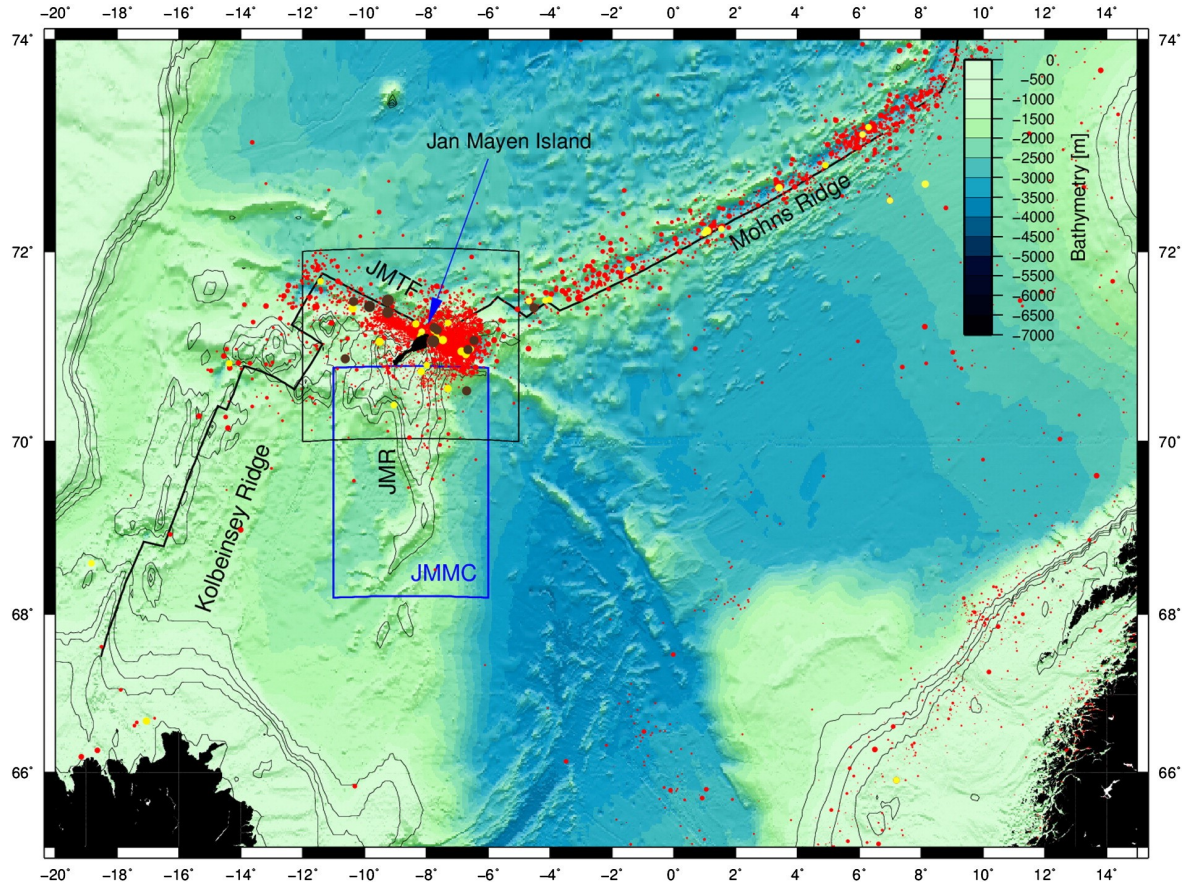

Figure 2.6: Tectonic map of the Jan Mayen area, showing the main tectonic features and historic earthquakes. The dots are the NNSN recorded earthquake between 1901 and 2013 (red $M_w < 5.0$; yellow $5.0 < M_w < 6.0$; brown $M_w > 6.0$). JMR is the Jan Mayen Ridge, JMTF the Jan Mayen Transform Fault, and the blue box outlines the Jan Mayen Micro-Continent (JMMC) (Rodríguez-Pérez and Ottemöller, 2014)

distinguished.

The seismic activity around Jan Mayen can roughly be divided into three groups: (1) swarm activity along the fracture zone, (2) normal tectonic activity along the fracture zone and (3) volcano-related seismicity. Havskov and Atakan (1991) observed uncertainties in the focal depth of the earthquakes because the majority of the hypocenters were located outside the seismic network. The authors also observed that it was particularly hard to find accurate depths for shallow earthquakes (< 10 km). In addition, they showed that events at a depth of 15 km contained an error of about ± 5 km. The hypocenters were generally located at 5-25 km depth, with some events below the Moho at 40 km. These depths suggest that the JMFZ has a thick cool crust, which allows for the possibility of

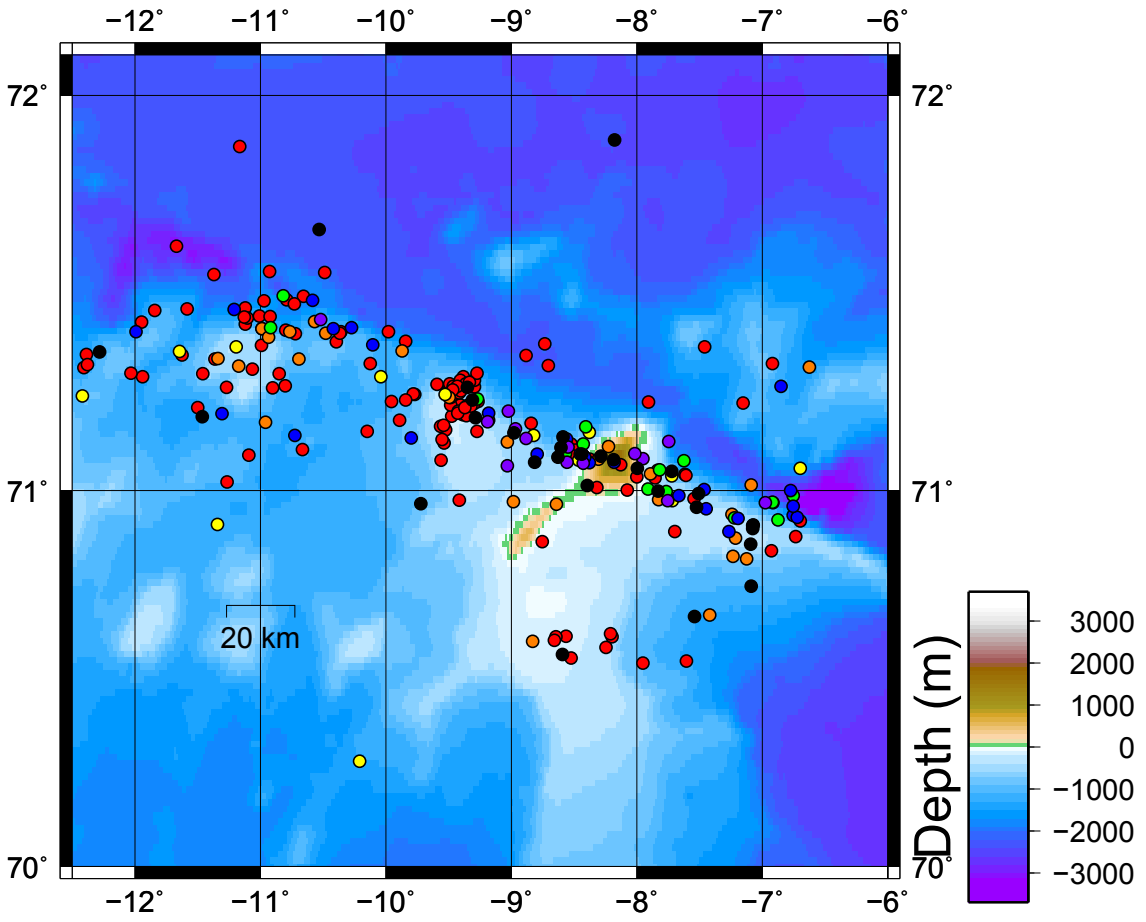

Figure 2.7: A seismicity map with the locations of the seismic events in the vicinity of Jan Mayen from November 2018 and May 2019. These are the events used in this thesis. Earthquakes are shown by filled circles that are color-coded by monthly distribution. The red circles indicate the events in November, December events are orange, January are yellow, February green, March blue, April magenta, and May black.

brittle fractures existing below the Moho (Havskov and Atakan, 1991). It is also possible that these events were mislocated.

Figure 2.6 shows that the south-eastern part of Jan Mayen has higher seismicity than the north-west. This suggests non-uniform seismicity along the plate boundary, which was also observed by Havskov and Atakan (1991).

The majority of the seismic events are aftershocks triggered by the largest events. For example, the main events in 1982 had, on average, 80 locatable aftershocks (Havskov and Atakan, 1991). Similarly, the April 14, 2004, $M_w = 6.0$ event had 110 aftershocks with

Table 2.1: List of all major strike-slip events in the JMTF with M $\geq$ 5.7 (Rodríguez-Pérez and Ottemöller, 2014).

Date (yy:mm:dd)	Time (GMT) (hh:mm:ss)	Lat (°)	Long (°)	Depth (km)	M
51/05/06	16:10:52	71.500	-9.240	0.0	7.0
52/12/10	05:58:05	71.200	-7.640	0.0	6.1
60/10/28	04:18:39	71.380	-9.240	0.0	6.8
61/04/29	09:29:11	71.130	-7.640	0.0	5.8
71/03/23	09:26:29	70.972	-6.855	28.8	5.7
72/09/08	11:34:42	71.420	-10.389	0.0	5.9
75/04/16	01:27:19	71.492	-10.356	15.3	6.2
79/11/20	17:36:09	71.134	-8.164	15.0	5.4
88/12/13	04:01:49	71.080	-7.780	15.0	6.9
00/05/21	19:58:57	71.226	-8.398	15.0	5.1
04/04/14	23:07:42	71.093	-7.472	10.5	6.3
11/01/29	06:55:29	70.990	-6.650	17.0	6.1
12/08/30	13:43:35	71.440	-9.840	24.0	6.7
18/11/09	01:49:35	71.703	-11.628	10.0	6.7

local magnitude larger than 2.7 (Sørensen et al., 2007). Recordings from the November 9, 2018, event and its 120 aftershock, also show this trend. All major events with $M > 5.7$ in the JMTF are listed in Table 2.1.

In addition to the seismic zones, there also is additional seismic activity around the island. These can not be related to geological structures in the area. It is possible that they are related to the island itself or poorly located.

Chapter 3

Seismic Noise Analysis of Seismic Data from Heimaey

This chapter gives an introduction of the two data-sets used in this thesis, Heimaey, and Jan Mayen. It mainly focuses on the Heimaey data-set, as this network was installed to collect data for this thesis. The chapter starts with the introduction of the seismic networks in Section 3.1. In Section 3.2, the deployment of the Heimaey network is discussed. After this, Sections 3.3 and 3.4 gives a noise analysis of the stations on Heimaey. The chapter ends with the event analysis for the Heimaey data-set in Section 3.5.

3.1 Seismic Networks

3.1.1 Heimaey Network

For this thesis, I have deployed five temporary stations on Heimaey (HEM1, HEM2, HEM3, HEM4, and HEM5). This was in collaboration with staff from IMO. The temporary network is referred to in this thesis as the Heimaey Temporary Seismic Network (HTSN). In total there are eight stations in the Heimaey network. In addition to the stations in HSTN, there are three stations (with the operation codes ves, vey, and bey) that are part of the Icelandic Seismic Network (ISN). IMO operates these stations. Figure 3.1a and Table 3.1a provide general information on the network. The figure shows the position of the stations, and the table provides background information.

Table 3.1: Tables with background information on the seismic stations in the Heimaey and Jan Mayen networks.

(a) List with the locations of the seismic station on Heimaey.

Station Code	Latitude°	Longitude°	Elevation (m)	Operator Code	Deployment
HEM1	63.4345 N	20.2388 W	144m	HTSN	10.2017 - 04.2019
HEM2	63.4277 N	20.2873 W	149m	HTSN	10.2017 - 04.2019
HEM3	63.4363 N	20.2617 W	111m	HTSN	10.2017 - 04.2019
HEM4	63.4404 N	20.2946 W	80m	HTSN	10.2017 - 04.2019
HEM5	63.3996 N	20.2882 W	183m	HTSN	08.2018 - 04.2019
ves	63.4429 N	20.2866 W	55m	ISN	2000 -
vey	63.4194 N	20.2754 W	154m	ISN	2017 -
bey	63.4486 N	20.1949 W	100m	ISN	2017 -

(b) List with the locations for the seismic statinos on Jan Mayen.

Station Code	Latitude°	Longitude°	Elevation (m)	Operator Code	Deployment
JMIC	70.9889 N	8.5094 W	211m	NNSN (IMS)	2003 -
JMI	70.9361 N	8.7402 W	211m	NNSN	1972 -
JNE	70.9941 N	8.3058 W	57m	NNSN	1972 -
JNW	71.0367 N	8.4358 W	95m	NNSN	1972 -

3.1.2 Jan Mayen Network

The seismic station network on Jan Mayen consists of four permanent stations (JMIC, JMC, JNW, and JNE). These are part of the Norwegian National Seismic Network (NNSN). The University of Bergen operates three of the stations (JMC, JNE, and JNW), the last station (JMIC) is operated by NORSAR. Figure 3.1b and Table 3.1b provide general information on the network.

3.2 Deployment of the Heimaey Network

The deployment of the HTSN started in late October 2017. At this time four of the five stations were deployed. Three of these stations were installed indoors (HEM2, HEM3,

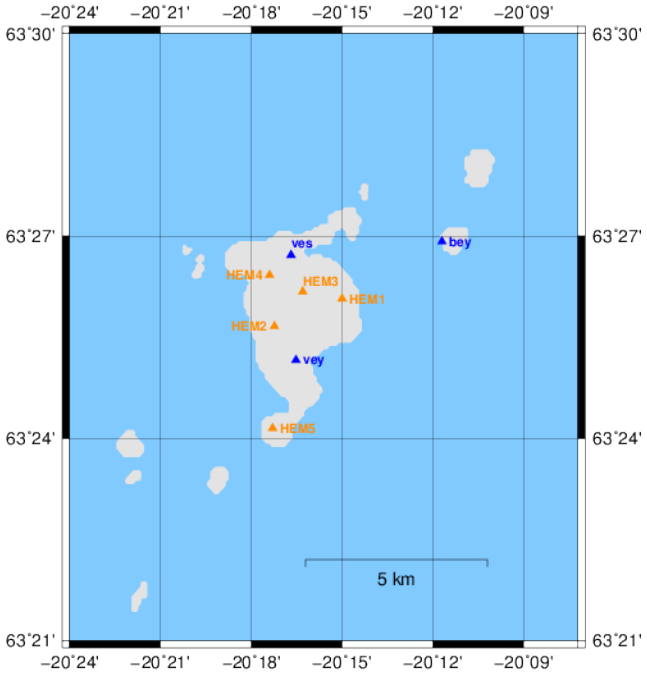

(a) Seismic stations distribution on Hemiaey. Orange triangles indicate UoB stations, whereas blue triangles indicate IMO stations.

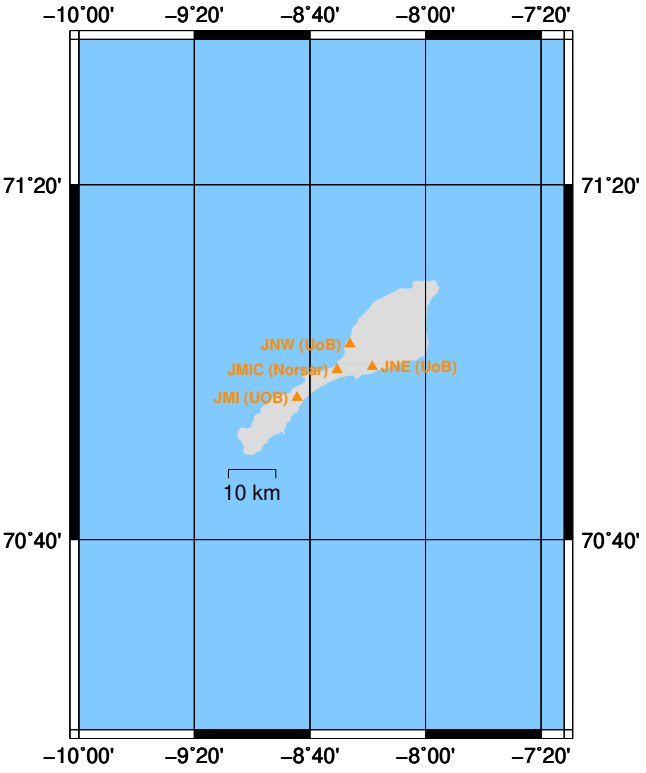

(b) Seismic stations distribution on Jan Mayen.

Figure 3.1: Station location map for Heimaey and Jan Mayen.

and HEM4), and the fourth station was installed outdoors (HEM1). A fifth indoor station was deployed in early August 2018 (HEM5). The seismic network was dismantled in late March 2019. Hence, the total time of deployment was 15 months.

3.2.1 Logistics for the Network Installation

The planning of the deployment took place at the IMO office in Reykjavik. This included contacting potential hosts for the stations, purchasing the relevant equipment and deciding on the installation sites for the five temporary seismic stations. The equipment required for the deployment included:

- plastic buckets,
- rock wool insulation,
- a solar penal,
- batteries,
- regulators,
- cement.

Plastic buckets were used to shield the seismometer from the surroundings, e.g., from human activity and weather. Rock wool was glued to the inside of the buckets, to decrease noise due to temperature variations. A solar panel was used as a power supply for the outdoor station. Batteries were used to provide additional power or to provide temporary power in case of power loss. Regulators were installed so that the batteries would not be overcharged. The cement was used to level the seismometers. The seismic equipment installed owned by UoB consisted of:

- Five 120 second period Nanometrics seismometer (Trillium 120PA),
- Five Nanometrics Taurus digitizer, with a 32 GB compact flash card with a sampling rate of 100 samples per second (sps).

3.2.2 Network installation

After sorting out all the logistics for the station installation, the equipment was transported to Heimaey and installed.

Figure 3.2: Three pictures from the installation on Heimaey. The figure to the left shows the seismometer with operation code HEM2. The other two figures are from the field installation (HEM1). Additional pictures are shown in Figure 9.1 in the Appendix.

HEM1 was placed outdoors on the eastern flank of the volcano Eldfell (see Figure 3.2). The station was placed in a 0.5-meter deep pit. A solar panel supplied the station with power. During periods with minimal sunlight, the use of the solar panel was limited. A battery to power the station during nighttime was therefore essential. Because of the limited power supply, HEM1 was not operational during the winter months (from the end of November to late January).

HEM2 and HEM3 were installed in the basements of two privately owned houses in the west and north on the island, respectively. Both were placed on the Helgafell lava (see the geological map of Figure 2.4). These locations were chosen as they had good contact with the bedrock, and there was power supply throughout the year. The bedrock at the HEM3 site had a rough surface. A concrete foundation was therefore built to level the seismic station.

HEM4 was the final station installed in October 2017. The station was deployed in an office in the north-western part of Heimaey, on the Helgafell lava. It had a continuous supply of electricity, and it turned out to be the station with the lowest noise level.

HEM5 was installed in early August 2018. The station was placed in a small house on the southern tip of the island, on the Stórhödi lava.

In addition to these five stations, two seismic stations from the Icelandic network on Heimaey were available (ves and vey) and one on the neighboring island Bjarnarey (bey). These three stations were equipped with solar panels, just like HEM1, and went offline during the same time period.

The data recorded from these eight stations have been studied in detail. The study includes noise analyses (Sections 3.3 and 3.4), detection of events (Section 3.5), location and relocation of events and an uncertainty analysis (Chapter 6).

3.3 Analysis of data

The data recorded on Heimaey was processed with the analysis software SEISAN developed by Havskov and Ottemöller (1999). Continuous data retrieved from the stations was transferred from the compact flashcards to a local server for easy access. Noise plots for each station were computed. The methodological background for the noise plot computation is presented in the next subsection.

3.3.1 Noise spectrum calculation

Seismic noise can be defined as unwanted energy in seismic data. All seismic data contain noise, and noise is considered to have two origins: instrumental and ambient noise (Havskov and Ottemöller, 2010). The data used in this thesis were primarily affected by ambient noise, which consists of both random and coherent noise.

The methodological focus for this thesis is to solve the earthquake location problem and obtain accurate seismic hypocenter locations (see Chapter 5). It is therefore important to have data with a high signal-to-noise ratio (SNR) so that the various seismic phases stand out in the data and can be accurately picked. In addition, it is interesting to quantify the noise spectrum and spectrogram, to get an overview of the noise level at the stations and the island.

The noise spectra for the Heimaey stations are estimated using the program CONNOI in SEISAN (Havskov and Ottemöller, 1999). SEISAN uses an approach similar to the one suggested by McNamara and Buland (2004) and later presented by McNamara and Boaz (2005). The approach aims to study noise based on the calculation of the distribution of power spectral density (PSD) using a probability density function (PDF). This approach is presented in the flowing paragraph:

In the first main step in computing the noise level, a finite length seismic time series have been sampled evenly N times at an interval of Δt. The data for each station component is divided into one-hour finite-length time segments. These time segments overlap by 50% and are continuously distributed in time (McNamara and Boaz, 2005). In the second main step, PSD preprocessing for each one-hour time segments is executed in four sub-steps. The first sub-step is to improve the Fast Fourier Transforms (FFT) speed by reducing the number of data points. The second sub-step reduces the variance of the final PSD estimates. This is done by dividing the one-hour segments into 13 segments, which overlap by 75%. The third sub-step corrects the data to a zeros mean so that any long period linear trend is removed. The final sub-step suppresses sidelobe leakage resulting from the FFT. This is done by applying a 10% sine taper to the ends of the time series (McNamara and Boaz, 2005). In the third main step the noise spectrum estimation, the noise PSDs are calculated. This is done via a finite-range Fast Fourier Transform (FFT) of the original data. The finite-range Fourier transform of a periodic time series $x(t)$ is given by

$$X(f,T) = \int_0^{T_r} x(t) e^{-i2\pi f t} dt. \tag{3.1}$$

where T_r denotes the length of the time segment. This equation can be rewritten by discretization of the frequency, f_k. The Fourier components are then defined as

$$X_k = \frac{X(f_k,T)}{\Delta t}, \text{ for } f_k = \Big(\frac{k}{N}t\Big) \text{ when } k = (0,1,2,...,N-1). \tag{3.2}$$

Further, the total PSD is calculated using the Fourier components

$$P_k = \frac{2\Delta t}{N}|X_k|^2. \tag{3.3}$$

This process is repeated for the 13 separate overlapping time segments within the one-hour record. After this, the final smooth PSD is calculated by taking the average of the 13 PSD estimates

$$P_k = \frac{1}{q}\Big(P_{k,1} + P_{k,2} + ... + P_{k,q}\Big), \tag{3.4}$$

$P_{k,q}$ is the raw estimate at frequency f_k of the qth time segment. When the smooth PSD has been estimated it is corrected for the 10% preprocessing taper and the instrument response. The final smooth PSD is converted to dB with respect to acceleration ($dB = (m/s^2)^2/Hz$),

$$P_k = 10 * log_{10}(P_k). \tag{3.5}$$

The fourth main step is the generation of seismic noise PDFs from the PSDs. For sufficient sampling of the PSDs, full octave averages are taken in 1/8 octave intervals. Powers are averaged between a short period corner, T_s, and a long period, $T_l = 2 * T_s$, so that the center period, T_c, within the octave is given by $T_c = \sqrt{T_s * T_l}$. The center period works as storage for the average power for the corresponding octave. The next average power is computed by incrementing T_s by 1/8 octave, so that $T_s = T_s * 2^{0.125}$. After this, the T_l and T_c are recomputed, and the average of the power is taken. This process continues until the longest resolvable period is reached, and the process is repeated for all one-hour PSD estimates, resulting in a smooth PSD estimate for each station component. Powers are then accumulated in 1 dB intervals to produce frequency distribution histograms for each period (McNamara and Boaz, 2005). Next, the PDF is used to plot the distribution of powers per period. The PDF can be estimated as

$$P(T_c) = \frac{N_{PTc}}{N_{Tc}} \tag{3.6}$$

for a given center period, T_c, where N_{PTc} is the number of spectral estimates that fall into a 1 dB power bin with a range from -200 to -80 dB. N_{Tc} is the total number of spectral estimates over all powers with a center period, T_c. The probability of a power occurring at a particular period can then be compared to the high and low noise model [(Peterson et al., 1993); (McNamara and Boaz, 2005)].

3.4 Noise Levels on Heimaey

In this section the seismic noise analyses for the Heimaey stations are presented. It starts by introducing the expected noise levels on Heimaey, made from observations during the deployment process, in Section 3.4.1. The noise spectrum and spectrogram for the different stations are then discussed, in the following two Subsections 3.4.2, and 3.4.3.

3.4.1 Seismic noise on the Heimaey stations

Noise spectrum calculated for HEM1, HEM4, and ves using SEISAN are shown in Figures 3.3, 3.4, and 3.5, respectively. The spectrum for HEM2, HEM3, HEM5, bey, and vey are given in the Appendix (see Figures 9.2, 9.3, 9.4, 9.5, and 9.6). The lower and upper black lines in the figures are the new low-noise model (NLNM) and the new high-noise model (NHNM), respectively. These upper and lower levels were obtained by studying the seismic background noise from a worldwide network of seismograph stations. The NLNM and the NHNM are used to indicate the baseline level of earth noise at each location and to detect operational problems for the system (Peterson et al., 1993). The noise spectra show high noise levels close to NHNM for all stations.

On Heimaey, the main noise source is ambient noise. Examples of ambient noise are the noise originating from antennas, construction sites, roads, ocean waves, wind, as well as noise related to cultural activity and meteorological phenomena (Kumar and Ahmed, 2011). Heimaey is affected by both microseismic and cultural noise. The island is located in the Gulf Stream, which is a current that shifts water mass from the Gulf of Mexico to the Arctic. This produces most of the microseismic noise observed on Heimaey. In addition, there is cultural noise from one of the largest ports in Iceland as well as daily activity from Heimaey's 4500 inhabitants. Furthermore, NHNM is a spectrum of average high background noise (Peterson et al., 1993). Peterson et al. (1993) estimated the NHNM using stations in noisy locations, like inland stations placed on alluvium, coastal stations with both microseismic and cultural noise, stations on ice with local interferences and island stations with microseismic noise. Therefore, the noise levels observed at the Heimaey stations were anticipated.

The noise sources for HEM1 are different from the other four stations. It was the only outdoor station and therefore subjected to larger temperature variations. As a precaution, a double layer of insulation was installed to avoid sensor drift during the deployment period. HEM1 was the only station installed in the young Eldfell lava east on the island. The lava is expected to have relatively high porosity because of its young age. In addition, the upper layer of the Eldfell lava is tephra. The coupling for the station is therefore expected to be worse than for the other stations (Mattsson and Höskuldsson, 2003).

Cultural noise sources for the other four stations were similar. HEM2, HEM3, and HEM5

were all affected by work in the houses in which they were installed. HEM4 was affected by noise due to a nearby garage and a golf course roughly 50-100 meters away. All of the stations were affected by activity on nearby roads, either on asphalt roads (HEM2, HEM3, HEM4, and HEM5) or a gravel road (HEM1).

HEM5 experienced additional noise sources. The wind was considerable at the location, and three 10-20 meters high antennas were oscillating in the wind creating high amplitude low-frequency noise. Meteorological equipment was installed in the same room as the seismometer and created noise with its constant vibration. It is worth pointing out that the location of HEM5 improves the aperture of the seismic network and thereby better constraints for the earthquake locations. Other reasons for deploying the station at this site was the continuous access to electricity and the fact that the station was not disturbed during the recording period. Unfortunately, the station went offline after one month of recording data, due to a battery malfunction.

3.4.2 Spectrum Noise Levels

Figures 3.3, 3.4, and 3.5 show the noise spectrum for the temporary stations HEM1, HEM4 and the permanent station ves. The high-frequency band (1-20 Hz) shows high cultural activity on the island, as was suggested in the discussion above. By comparing the permanent ves station in Figure 3.5 and the outdoor and indoor stations in Figures 3.3 and 3.4, we can see that the high frequency noise level for HEM4 and ves have similar dB levels, whereas the noise level for HEM1 is 10 dB higher. This high noise level for HEM1 might be a consequence of the porous Eldfell lava, or because the solar panel was oscillating in the wind.

Other sources of high-frequency noise were running water and wind (McNamara and Buland, 2004). These noise sources were especially clear in the intermediate period range (4-16 seconds). In particular, two distinct peaks were seen in this range, the double-frequency peak (4-8 sec) and the single-frequency peak (10-16 sec). The double-frequency peak was generated by standing gravity waves resulting from superposition of oceanic waves traveling at equal periods in opposite directions, and can easily be identified in Figure 3.3, 3.4, and 3.5. The single-frequency peak was generated in coastal waters, with seismic energy generated directly from the interaction of waves with the shallow

seafloor (Hasselmann, 1963). This peak can also be easily identified on all spectrums. The peak, however, is not as clear as the double frequency peak and it is lower than the NHNM. The peaks depend on the maximum wind speed, and the amount of time the wind has been acting on the ocean (Pierson Jr and Moskowitz, 1964). Because Heimaey is located outside the south coast of Iceland, the maximum wind speed is high (Figure 3.6). Moreover, the wind acts on the ocean over long distances. This caused the high amplitude noise peak at a 4-5 sec period for the double-frequency peak and at a 10-11 sec period for the single-frequency peak.

3.4.3 Spectrogram Noise Levels

Spectrograms are used to evaluate the variation in the seismic noise levels for different time periods. Figure 3.6 shows PSD spectrograms for HEM1 and HEM4 and an average wind speed plot for the whole time period the HTSN was deployed. Figure 3.7 shows the spectrograms for HEM2, HEM3, and HEM5.

The wind-speeds were recorded by an automated observational station, located 118 m.a.s.l at Storhofdi, on the southern tip of Heimaey (for more information see IMO (ndb)). The station took measurements of wind-speed every 10 minutes. A running average filter was used to extract the long term variations in the measurements and to compute the wind speed plot shown in Figure 3.6.

The figures show the noise variation for the recording period of HTSN and a weekly variation in cultural noise can be observed. The contour continuously changes between high (red/yellow) and low (green) noise levels for weekdays and weekends, respectively, in the 1-20 Hz frequency range. This is interpreted to be caused by more human activity during weekdays than in the weekends.

Seasonal variations are also present in the figures. Changes in the weather primarily caused these variations. The weather variation can be observed in the average wind speed plot in Figure 3.6, and a clear correlation between noise level and wind speed is seen. The most significant variation in the low-frequency noise level is observed in the period range: 1 to 35 seconds. During the months from October to March, the noise level was at its highest with a noise (90 dB) and wind (15 m/s) peak in January 2018. The noise

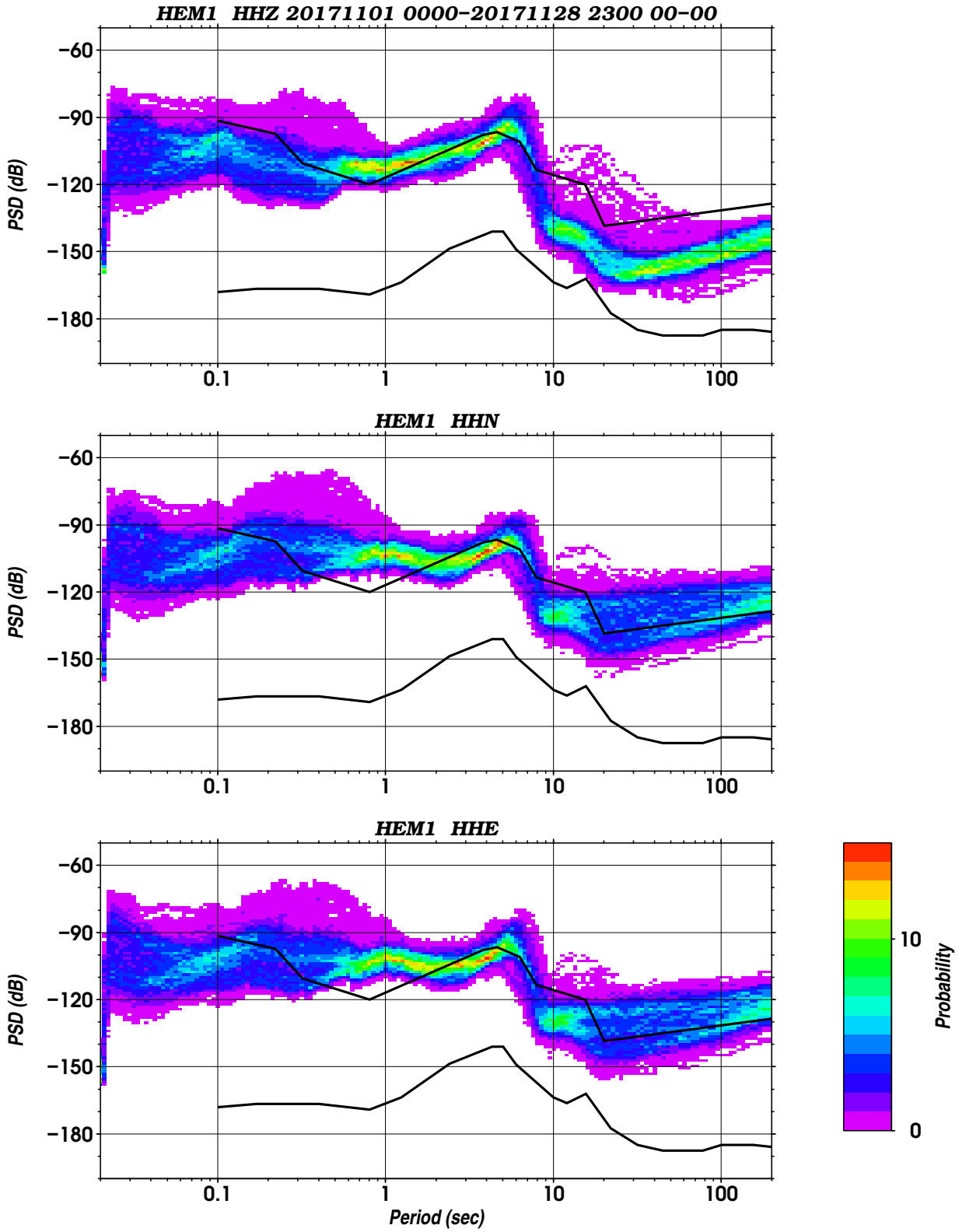

Figure 3.3: Noise plot for November 2017 for HEM1 (the temporary outdoor UoB station).

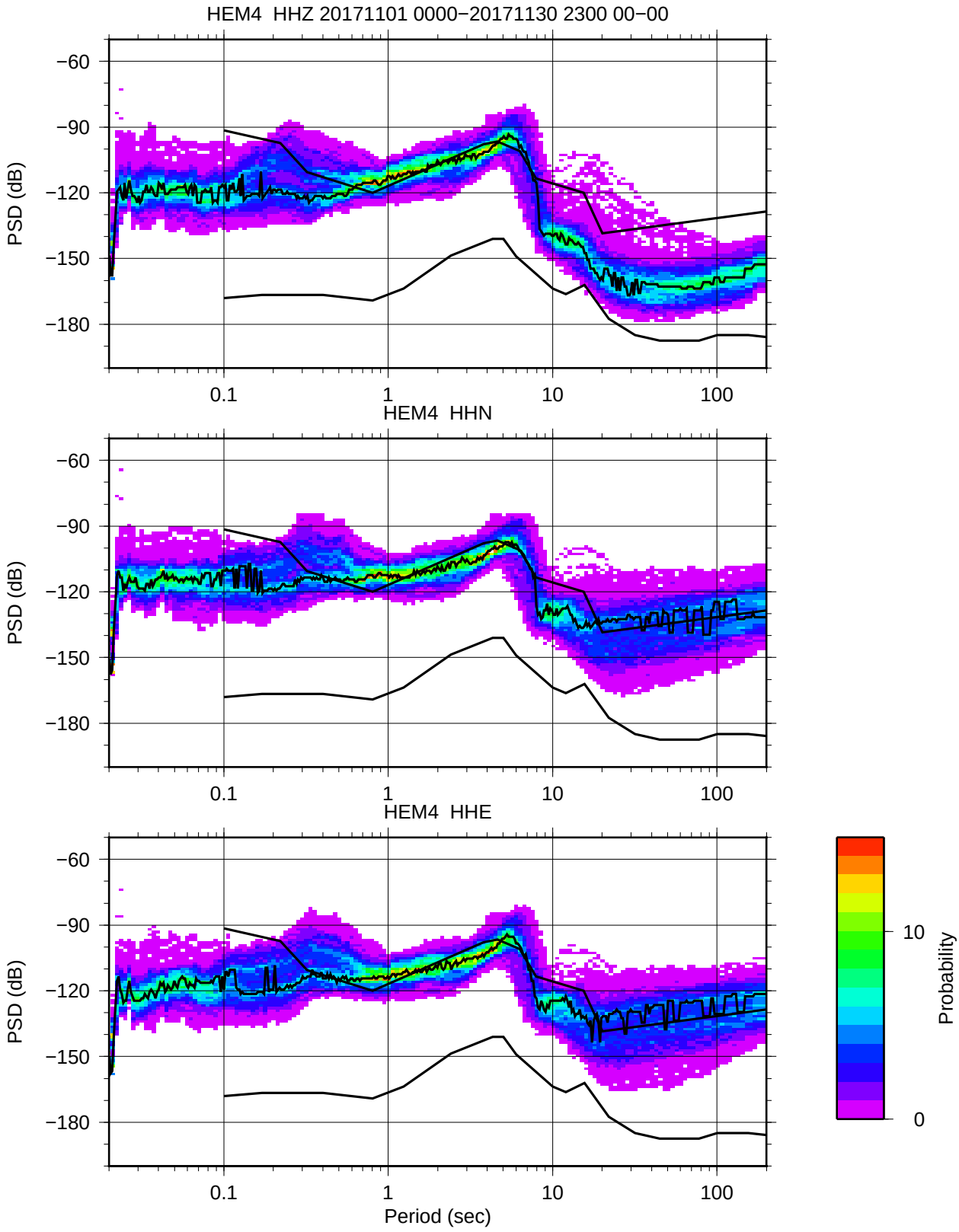

Figure 3.4: Noise plot for November 2017 for HEM4 (the temporary indoor UoB station).

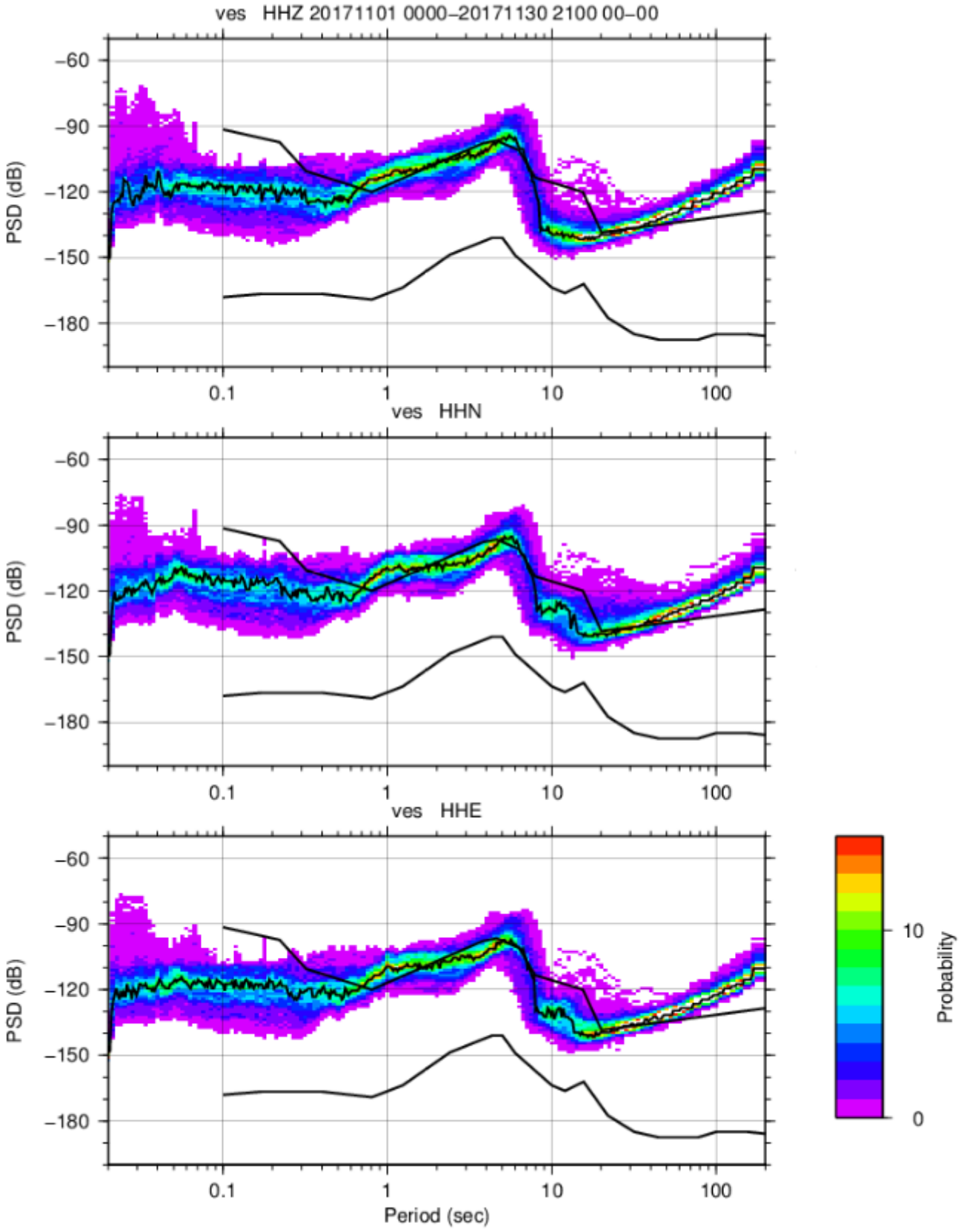

Figure 3.5: Noise plot for November 2017 for ves (the permanent outdoor IMO station).

decreased in May and reached its lowest values at the beginning of June. This is the time period that recorded the lowest average wind speed.

The spectrograms also show that the micro-seismic peaks are shifted towards longer periods during the winter. It has been argued that such shifts in micro-seismic peaks can be related to rougher weather conditions during the winter months, with higher winds creating longer ocean wave periods (e.g., (Bretschneider, 1959)). This phenomenon was also observed by Demuth et al. (2016) in their study on ambient noise levels in Norway.

3.5 Analysis of Seismic Events

In this section, the event detection methodology is explained. It was then applied to the data recorded on Heimaey, which resulted in the detection of two seismic events. More events were expected for the deployment period, because of the swarm in August 2018.

3.5.1 CONDET - Detection program for continuous data

This subsection discusses the detection program used to detect relevant events from the continuous seismic data. IMO located six events in the vicinity of Heimaey from October 2017 to March 2019. This is less than the average for similar periods seen from historical data (IMO, nda). It is possible that some events of interest were overlooked. The detection program CONDET was, therefore, used to detect further events.

CONDET works in either one or two steps. The first step detects events on every single station. The user can then choose to execute a second step that detects events on a minimum number of stations. If the signal is repeated on the minimum number of stations, the detection is saved.

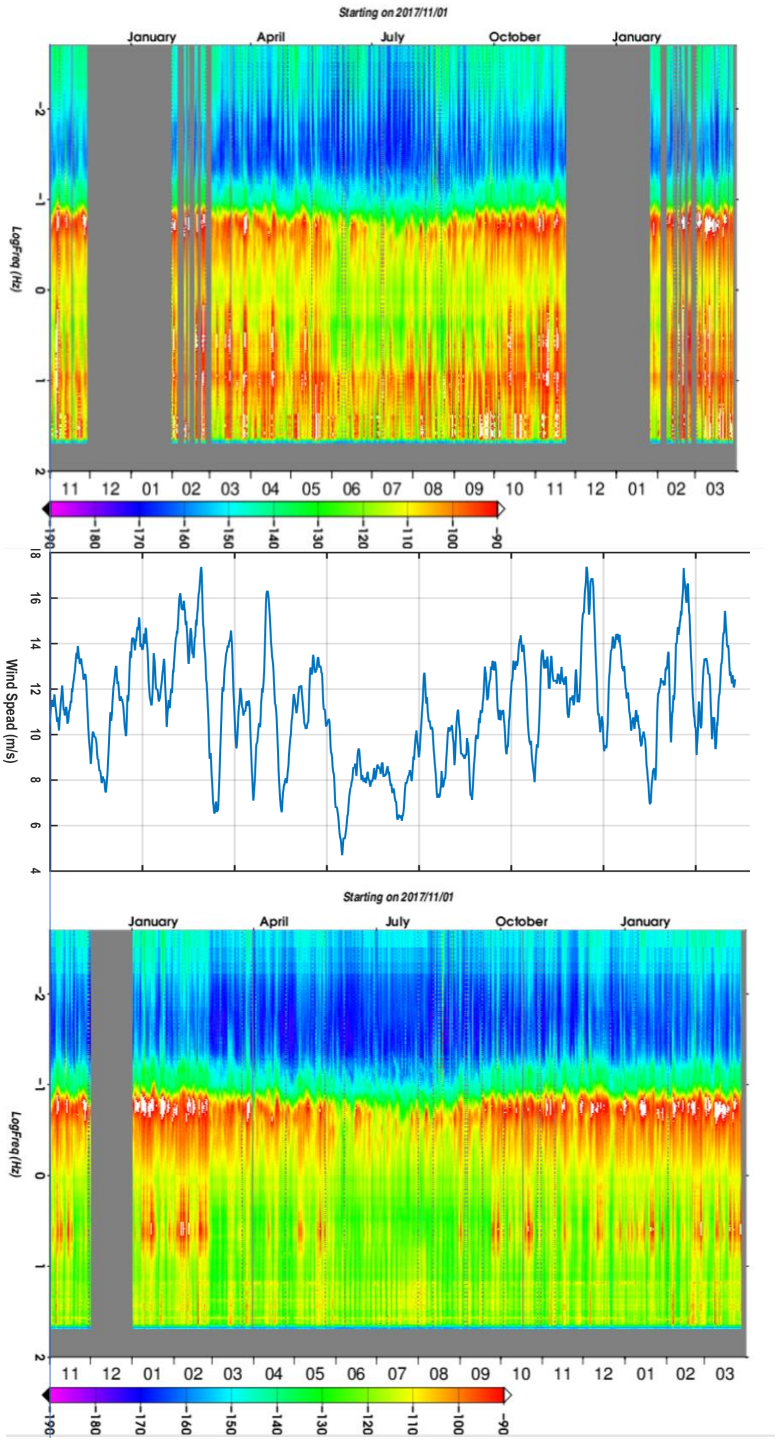

Figure 3.6: Noise spectrograms for HEM1 and HEM4, with average wind-speed over the deployment period plotted in between. A clear correlation between wind-speed and noise can be observed.

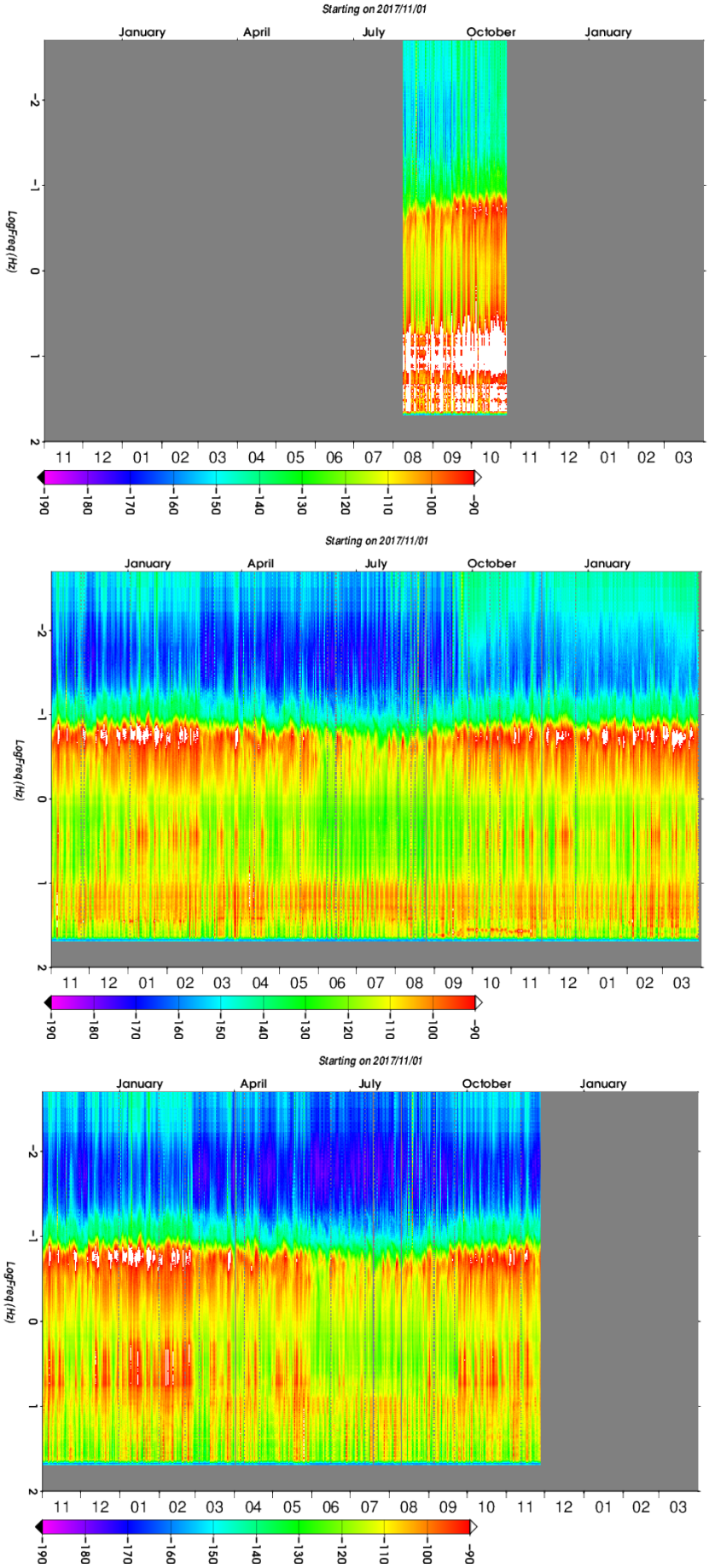

(a) Spectrogram HEM5.

(b) Spectrogram HEM3.

(c) Spectrogram HEM2.

Figure 3.7: Noise spectrograms for HEM2, HEM3, and HEM5 for the whole deployment period.

The Carl Johnson's detector was the detection algorithm in CONDET used to detect further events. It compares the short-time average (STA) and the long-time average (LTA) to find earthquakes in a filtered continuous dataset. First, the STA of the trace was computed for one second time windows. A weighted average of previous STAs was then used to find the LTA. By default, eight STAs were used to compute the LTA. In addition to these averages, rectified averages were required. These were calculated after the LTAs. The short-time rectified average (STAR) was found from the absolute value of the difference between the LTA and the trace, averaged over one second. The long-time rectified average (LTAR) is the weighted average of the previous STAR values. These four averages were combined to determine the station trigger status (TS), with the user specified values 'Ratio' and 'Quiet'

$$TS = STAR - Ratio * LTAR - |STA - LTA| - Quiet. \tag{3.7}$$

If TS > 0 an event is detected and saved.

In practice, the user starts by specifying the parameters used by the program. Running the commando 'condet' then finds triggers for every station in a user specified time window. When the algorithm is executed the user chooses to either extract these events by running the extract script, or by running the network detection 'condet -net' to see whether a detection is repeated over several stations [(Havskov et al., 2009); (trac, nd)].

3.5.2 Detection Result

Running CONDET for the whole time period resulted in a total of 3242 detections. 173 of these detections were studied further (approximately 5.33%), the rest were considered as noise. Not all of the relevant events were seismic. Some are believed to originate from ocean waves that convert to surface waves when hitting the shores. This is similar to the observation made on Svalbard by Köhler and Weidle (2019).

Two seismic events were detected in the vicinity of Surtsey by the Carl Johnson's detector. IMO have previously found these events and located them (from IMO bulletin):

- 2017 April 24 08:49:19, Latitude: 63.34°, Longitude: -20.62°, Depth: 13.60 km, Magnitude 2.49,

- 2019 January 31 01:42:04, Latitude: 63.32°, Longitude:-20.64°, Depth: 14.50 km, Magnitude 3.40.

Additional events on the mainland were also detected. These were not of interest because they occurred outside the survey area, the Vestmannaeyjar Volcanic System. The two events from the Heimaey data-set are further analyzed in Chapter 6.

Chapter 4

Ray Tracing

4.1 Overview

This chapter presents the theoretical and numerical aspects of ray tracing. This is done in two separate sections. First in Section 4.2.1, the theory behind elastic wave propagation is given. Then, in Subsections 4.2.2 and 4.2.3 I discuss the core part of ray theory in elastic isotropic media. In particular the eikonal equations for P-waves and S-waves and the ray equations are given. Section 4.3, discusses how numerical ray tracing implementation is done in this thesis. This section first gives an introduction to essential concepts used for the implementation, e.g. ordinary differential equations, velocity models and interpolation schemes. After this, two different methods for ray tracing are discussed. This is followed by an explanation of the numerical solution of the ray equations. The section ends with a description of one-point and two-point ray tracing.

4.2 Ray Tracing Theory

4.2.1 Elastic wave propagation

The Elastic Wave Equations

Elasticity theory describes how a material rebounds back into its original form after the applied stress acting on it has been released (Snieder, 2002). For an infinitesimal surface

with normal vector $\hat{\mathbf{n}}$ and a surface area ds, the forces acting on ds are given by

$$\mathbf{T_n} = \mathbf{T} \cdot \hat{\mathbf{n}}, \tag{4.1}$$

where $\mathbf{T_n}$ denotes the traction force and $\mathbf{T}$ is the stress tensor. Additional forces that can act on the medium are gravitational forces and/or a seismic force. These forces can all be related through Newton's second law of motion:

$$\int \rho\, \ddot{\mathbf{u}}\, dV = \int \mathbf{T} \cdot \hat{\mathbf{n}}\, dS + \int \mathbf{f}\, dV, \tag{4.2}$$

with ρ denoting density, $\ddot{\mathbf{u}}$ acceleration and $\mathbf{f}$ body force density (Auld, 1973).

Gauss' theorem is applied on the surface integral in equation (4.2) to find the forces acting on an infinitesimal volume dV. Gauss' theorem states that:

$$\int \mathbf{T} \cdot \hat{\mathbf{n}}\, dS = \int \nabla \cdot \mathbf{T}\, dV. \tag{4.3}$$

When we apply this in Newton's second law of motion we get

$$\int \rho\, \ddot{\mathbf{u}}\, dV = \int \nabla \cdot \mathbf{T}\, dV + \int \mathbf{f}\, dV. \tag{4.4}$$

This equation holds for an arbitrary volume. Therefore the integrals can be eliminated. Finally, this gives the equation of motion

$$\rho \ddot{\mathbf{u}} = \nabla \cdot \mathbf{T} + \mathbf{f}. \tag{4.5}$$

and in component notation

$$\rho \ddot{u}_i = \partial_j T_{ij} + f_i. \tag{4.6}$$

Relating strain deformation and stress in a general medium is complicated. However, if we only consider small elastic deformations then the relation between strain and stress can be linearized and is given by Hooke's law:

$$T_{ij} = c_{ijkl} S_{kl}, \quad i, j, k, l = 1, 2, 3, 4. \tag{4.7}$$

Here c_{ijkl} denotes the components of the elastic stiffness tensor, S_{kl} the components of the strain tensor, T_{ij} are the components of the stress tensor and the summation convention has been used. The strain tensor $\mathbf{S}$ is related to the particle displacement field $\mathbf{u}$ by

$$S_{ij} = \frac{1}{2}\left(\frac{\partial u_i}{\partial x_j} + \frac{\partial u_j}{\partial x_i}\right), \tag{4.8}$$

where $\mathbf{x} = (x_1, x_2, x_3)$ denotes the spatial coordinates. There is symmetry in the strain tensor: $S_{ij} = S_{ji}$. Therefore, it follows from Hooke's law that the stress tensor and the elasticity stiffness tensor are also symmetric. These symmetries reduce the number of independent components in equation (4.7), simplifying the tensors (Auld, 1973). The strain relationship in equation (4.8) can be combined with Hooke's law:

$$T_{ij} = c_{ijkl} \frac{\partial u_k}{\partial x_l}, \tag{4.9}$$

This can be inserted into the equation of motion (4.5)

$$\rho \, \ddot{u}_i = \frac{\partial}{\partial x_j} \left(c_{ijkl} \frac{\partial u_k}{\partial x_l} \right) + f_i, \tag{4.10}$$

which is the elastic wave equation in the time domain. It is often convenient to study the wave equation in the frequency domain. In this case we have

$$\rho \omega^2 \hat{u}_i + \frac{\partial}{\partial x_j} \left(c_{ijkl} \frac{\partial \hat{u}_k}{\partial x_l} \right) = -\hat{f}_i. \tag{4.11}$$

where $\hat{u}_i$, and $\hat{f}_i$ are the Fourier transform of u_i and f_i, respectively. Equations 4.10 and 4.11 are linear second order partial differential equations. They are solved for the displacement vector $\mathbf{u}$, given the density ρ, the elastic stiffness tensor $\mathbf{c}$ and the body force density $\mathbf{f}$ (Auld, 1973).

4.2.2 Asymptotic Wave Propagation

In general, it is difficult to find an explicit solution to the elastic wave equation in heterogeneous media (i.e., media where ρ and $\mathbf{c}$ are a function of position $\mathbf{x}$). A first simplification is to assume that the medium is isotropic.

In elastic isotropic media the components of the stiffness tensor $\mathbf{c}$ is given by

$$c_{ijkl} = \lambda \delta_{ij} \delta_{kl} + \mu (\delta_{ik} \delta_{jl} + \delta_{il} \delta_{jk}) \tag{4.12}$$

where λ and μ are the Lamé's parameters, and δ_{ij} denotes the Kronecker delta.

By inserting equation (4.12) into equation (4.10) the elastodynamic wave equation in vector notation becomes

$$\rho \frac{\partial^2}{\partial t^2} \mathbf{u}(\mathbf{x}, t) = (\lambda + \mu) \nabla (\nabla \cdot \mathbf{u}(\mathbf{x}, t)) + \mu \nabla^2 \mathbf{u}(\mathbf{x}, t) + \mathbf{f}(\mathbf{x}, t). \tag{4.13}$$

This equation can be solved for a point source if the medium is homogeneous (Pujol, 2003). The body force density for a point source is given by

$$\mathbf{f}(\mathbf{x}, t) = \mathbf{f}\delta(t)\delta(\mathbf{x} - \mathbf{x}_s), \tag{4.14}$$

and the Green's tensor for a homogeneous medium can be computed (with the constants λ, μ, and ρ). The Green's tensor contains far-field, intermediate-field and near-field terms. At large offsets, the far-field terms are the only terms that are relevant, whereas the near and intermediate fields are only considered when the receivers are sufficiently close to the source. The far field is defined to be all $\mathbf{x}$ such that

$$\frac{\omega|\mathbf{x} - \mathbf{x}_s|}{v_p} >> 1, \tag{4.15}$$

Here $v_p = \sqrt{\frac{\lambda+2\mu}{\rho}}$ is the P-wave velocity (Madariaga, 2007).

For the work in this thesis, only the far-field terms are of interest. It can be shown that in a heterogeneous isotropic elastic medium two wave types exist: P- and S-wave. Furthermore, when considering high frequency waves only, one can solve equations for the travel time T and amplitude A for each of these waves. The travel times satisfy the P- and S-wave eikonal equation:

$$|\nabla T_p|^2 = \frac{1}{v_p^2}, \text{ and } |\nabla T_s|^2 = \frac{1}{v_s^2}, \tag{4.16}$$

where

$$v_p = \sqrt{\frac{\lambda + 2\mu}{\rho}} \tag{4.17}$$

is the P-velocity and

$$v_s = \sqrt{\frac{\mu}{\rho}} \tag{4.18}$$

is the S-velocity.

In this thesis the focus is on the travel times of the P-waves and S-waves. The amplitudes are not considered. However, for the sake of completeness it is useful to give the frequency domain Green's tensor, which can be computed once the travel times and the amplitudes (i.e., the geometrical spreading) are known. The P-wave Green's tensor is

$$\mathbf{G}_{rs} = \mathbf{p}_r\mathbf{p}_s(\rho_r\rho_s v_r v_s^3)^{-\frac{1}{2}} R_{rs}^{-1} e^{i\omega T_{rs}}. \tag{4.19}$$

Here $\mathbf{p}_r, \mathbf{p}_s$ denote the polarization vectors at the receiver and source respectively, v_r and v_s, are the P-velocities at the receiver and source, respectively, ρ_r and ρ_s, are the densities

at the receiver and the source, R_{rs} is the solution of the transport equation (the equation for the amplitude) and T_{rs} is the travel time of the ray from the receiver to the source (Dahlen et al., 2000). The Green's tensor for the S-waves is quite similar.

The eikonal equations (4.16) for the P-waves and S-waves are first-order non-linear partial differential equations. These equations are solved to find the wavefront as it radiates away from the seismic source. The eikonal equation can be solved numerically (Sethian, 1999), but the solution has some limitations. For instance, multipathing is not taken into account. Instead of solving the eikonal equation directly, it is easier to solve for the lines/curves perpendicular to the wavefronts. These curves are called rays, or ray paths, and are given by the ray equations (Pujol, 2003). This is the topic of the next sub-section.

4.2.3 Ray tracing

The ray equations are a set of ordinary differential equations used to solve the non-linear eikonal equation, which was discussed in the previous section. These equations give the position $\mathbf{x}(t)$ of a ray at time t, given a velocity model v and a source position $\mathbf{x}_s$ (Cerveny, 2001). The ray equations are

$$\frac{d\mathbf{x}(t)}{dt} = v(\mathbf{x})^2\mathbf{p}, \tag{4.20}$$

$$\frac{d\mathbf{p}(t)}{dt} = -\frac{1}{v(\mathbf{x})}\nabla v(\mathbf{x}), \tag{4.21}$$

where $\mathbf{p}(t)$ denotes slowness as a function of time, $\mathbf{x}$ is position along the ray and v velocity. Note that slowness is defined as $\mathbf{p} = \nabla T$ and has a length of $\frac{1}{v}$ (see equation (4.16)). Moreover, the slowness vector $\mathbf{p}(t)$ provides the direction of the ray, as it is tangent to the ray path $\mathbf{x}(t)$. As is the case for all differential equations, initial conditions are required to solve the ray equations uniquely. The initial condition for the ray path is $\mathbf{x}(0) = \mathbf{x}_s$. The initial condition for the slowness vector can be specified by the take-off angles and the velocity at the source position

$$v_0 = v(\mathbf{x}_s). \tag{4.22}$$

In 3D these initial conditions can be given explicitly by choosing a local coordinate system at the source location. In this case

$$\mathbf{p}_0 = \frac{1}{v(\mathbf{x}_s)}(\sin(\theta)\cos(\phi), \sin(\theta)\sin(\phi), \cos(\theta)), \tag{4.23}$$

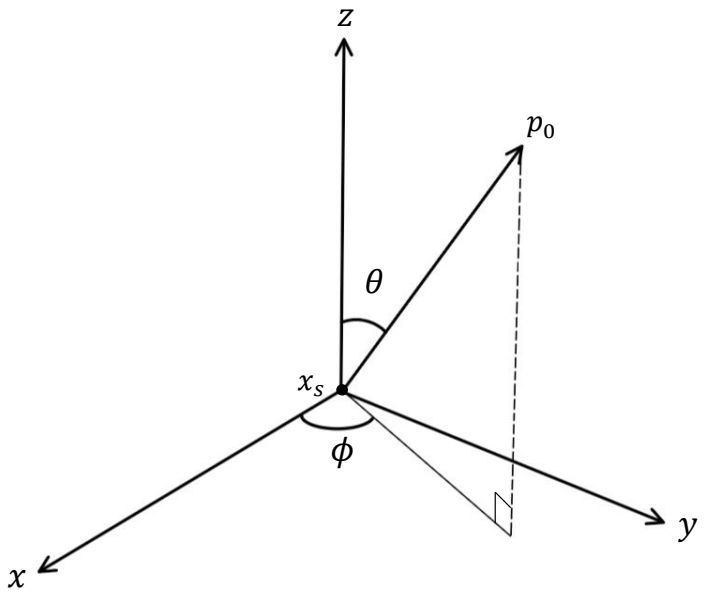

Figure 4.1: Figure that illustrates the inital conditions for 3D ray tracing. In particular, the take-off angles θ and ϕ at the source point $\mathbf{x}_s$.

where $\theta = [0, \pi]$ is the angle between the vertical and the ray path and $\phi = [0, 2\pi]$ is the azimuth (see Figure 4.1).

4.3 Ray Tracing - Numerical Implementation

4.3.1 Ordinary Differential Equations

As noted in Subsection 4.2.3 ray tracing involves solving a set of ordinary differential equations (ODE). Differential equations are equations used to model and predict systems that change with time (Sauer, 2014). For the ray tracing application, this means that the ray equations describe how the ray path find its way through a heterogeneous velocity model.

ODE's can be written in two different ways, in vector form

$$\frac{d\mathbf{x}}{dt} = \mathbf{g}(t, \mathbf{x}) \tag{4.24}$$

and as a set of scalar equations

$$\begin{cases} \frac{dx_1}{dt} = g_1(x_1, x_2, \cdots, x_n, t) \\ \frac{dx_2}{dt} = g_2(x_1, x_2, \cdots, x_n, t) \\ \vdots \\ \frac{dx_n}{dt} = g_n(x_1, x_2, \cdots, x_n, t), \end{cases} \tag{4.25}$$

where time t is the independent variable of the system. The initial conditions can also be written as vector equations or a set of scalar equations. In terms of the scalar equations the equations are $x_i(t_0) = x_0$, for $i = 1, ..., n$ and g_i is a known function.

In general, equations (4.24) and (4.25) can not be solved analytically and need to be solved numerically. If the velocity model is smooth then there are different methods to solve these types of equations, e.g. the Euler method, the modified Euler method, the midpoint method and various order Runge-Kutta methods (Sauer, 2014). These methods solve the system for different levels of accuracy, depending on the method and the step sizes used. The most accurate methods are often more complex and more computationally demanding than the simplest. It is therefore important to choose the method that fits a particular problem best (Sauer, 2014). Solving the equations numerically is done in Subsection 4.3.5. Before doing this it is necessary to discuss the velocity models and the interpolation methods as they are both used in the ray tracing.

4.3.2 Velocity models

In this thesis I do ray tracing through three different types of velocity models, and I study the effect these have on the solution of the earthquake location problem. For the earthquake location problem in the vicinity of Heimaey a smooth 1D velocity model for the south-western Iceland presented by Tryggvason et al. (2002) is used. The location problem around Jan Mayen, is solved using two different velocity models, a layered discontinuous 1D model presented by Sørne and Navrestad (1975) and a 3D velocity model based on a 2D model given by Kandilarov et al. (2012).

1-Dimensional Velocity Models for Heimaey and Jan Mayen

To locate the earthquakes in the VVS the P-wave velocity model shown in Figure 4.2a is used, whereas the discontinuous 1D P-wave velocity model used for Jan Mayen is shown in Figure 4.2b.

Note that a 1D velocity model in this thesis refers to variation with depth only, i.e. $v(x, y, z) = v(0, 0, z)$ for all x and y, and for simplicity this is denoted by $v(z)$.

3-Dimensional Jan Mayen Velocity Model

Kandilarov et al. (2012) obtained a 2D velocity model using a combination of Ocean Bottom Seismic (OBS), Multichannel Seismic (MCS) and gravity data. This data was collected in 2006 during a survey along two lines along the northernmost part of the Jan Mayen ridge. The first line, 165 km long, is east of Jan Mayen and has a SW-NE trend. The second line is 220 km long, and goes along Jan Mayen from south to north. The two lines intersect approximately 60 km from the beginning of line two and 20 km from the beginning of line one. The reflection and refraction surveys were executed to estimate the velocities, which were further constrained using gravity data (Kandilarov et al., 2012).

For the work in this thesis the line east of the island was used. It was extended from 2D to 3D (see Figure 4.3a for the 2D profile and Figure 4.3b for the 3D volume). This was done by first setting the 2D line as a S-N line, it was then extended to 3D. This volume was then rotated clockwise to mimic the SW-NE trend of line two.

4.3.3 Ray tracing through models with smooth and discontinuous velocities

In seismic wave propagation there are two basic ways to define velocity models. The first assumes that the velocity is smooth. In this case the model is often given on a number of grid points. The second assumes that the model consists of a number of layers with constant velocities that are separated by discontinuities. In practice it is usually best to use a combination of the two velocity models: i.e., a velocity model that has a smoothly varying part but also a number of interfaces. However, ray tracing through these types of

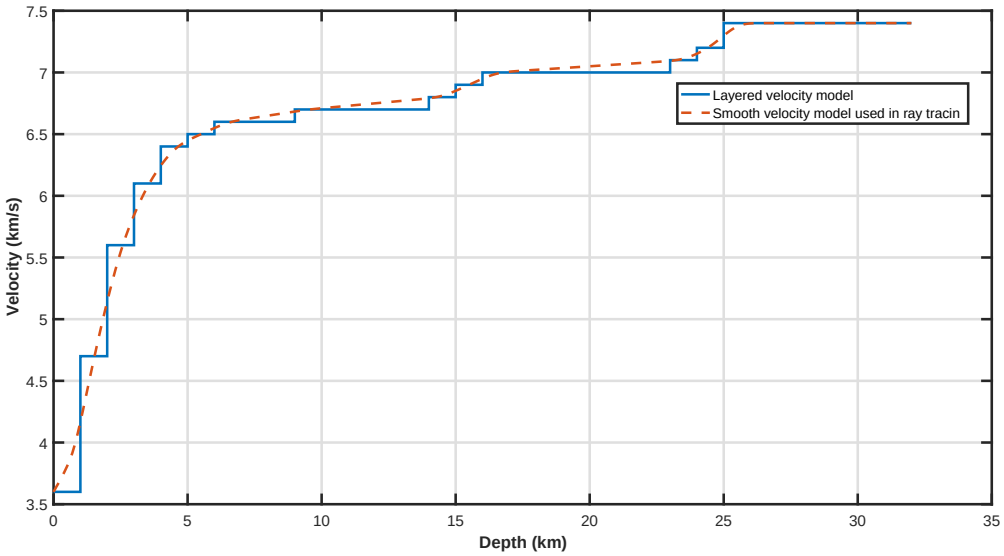

(a) The 1D velocity model used in Heimaey. The solid line indicates the layered velocity model, whereas the dashed line indicates the smooth model used to solve the ray equations (Tryggvason et al., 2002).

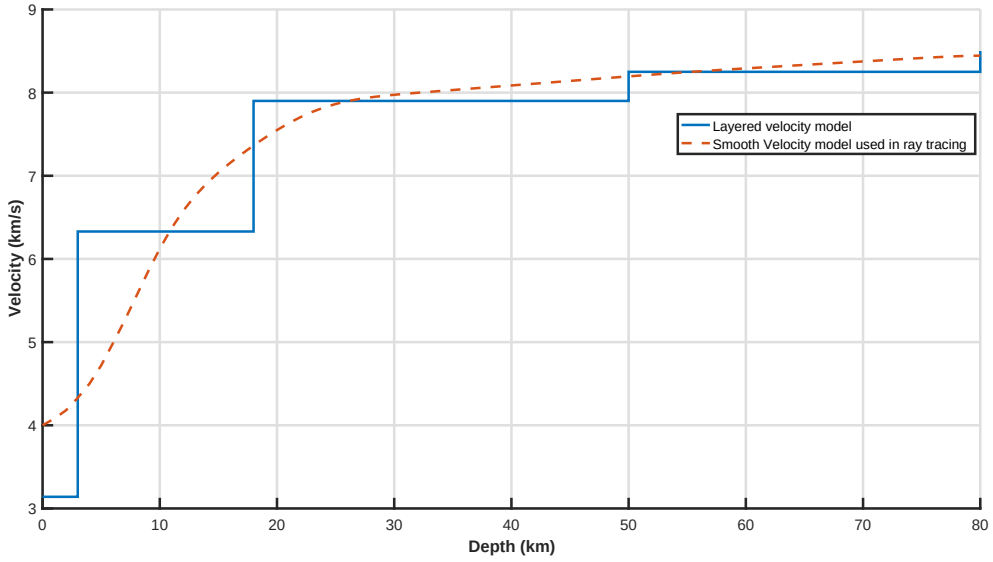

(b) The 1D velocity model used in the Jan Mayen region. The solid line indicates the layered velocity model, whereas the dashed line indicates the smooth model used to solve the ray equations (Sørne and Navrestad, 1975).

Figure 4.2: The 1D velocity models applied to solve the location problem. (a) Shows the model for VVS, and (b) the model for the Jan Mayen region.

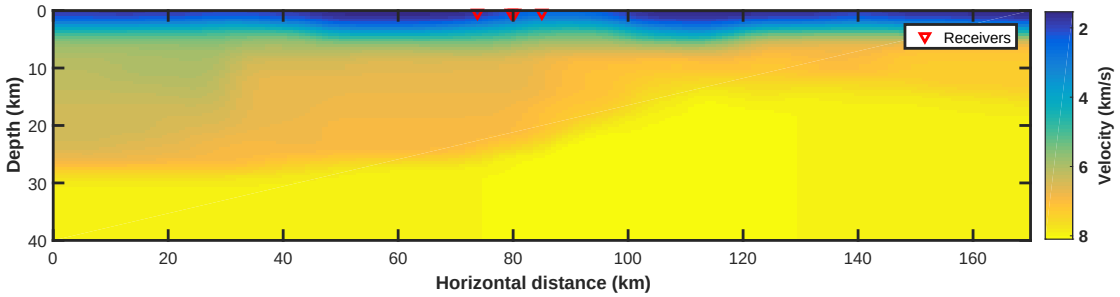

(a) 2D velocity profile for Jan Mayen determined using Kandilarov et al. (2012).

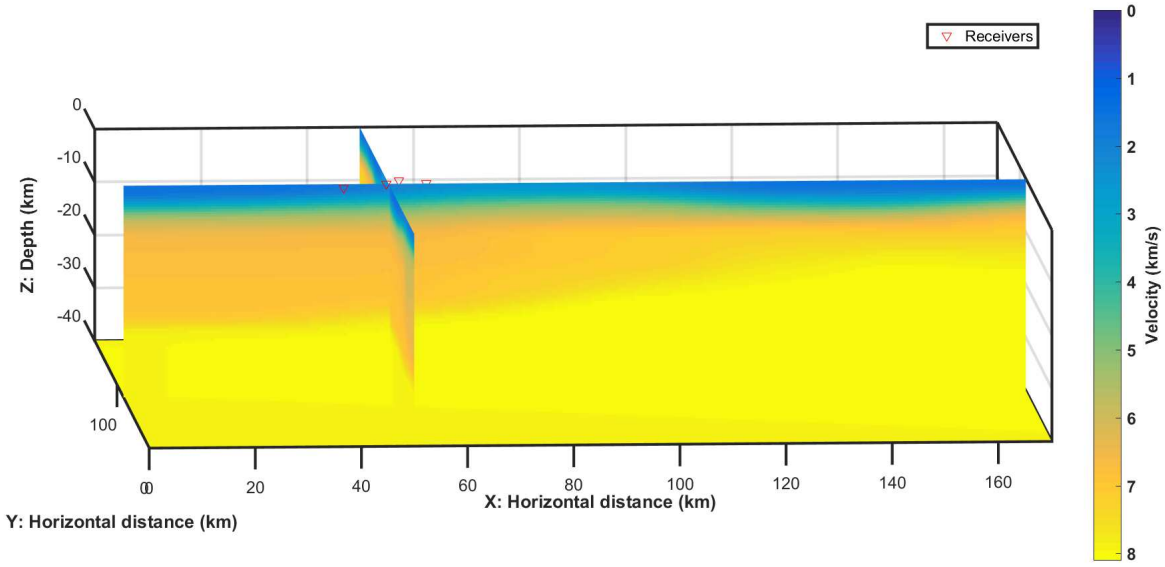

(b) The 3D velocity model for Jan Mayen. This is determined by extending the 2D profile in figure (a).

Figure 4.3: 2D profile (a) and 3D volume (b) for the Jan Mayen region. The velocity model has been modified from the original velocity model given by Kandilarov et al. (2012). The modification includes smoothing of the original values and expansion of the edges of the velocity model.

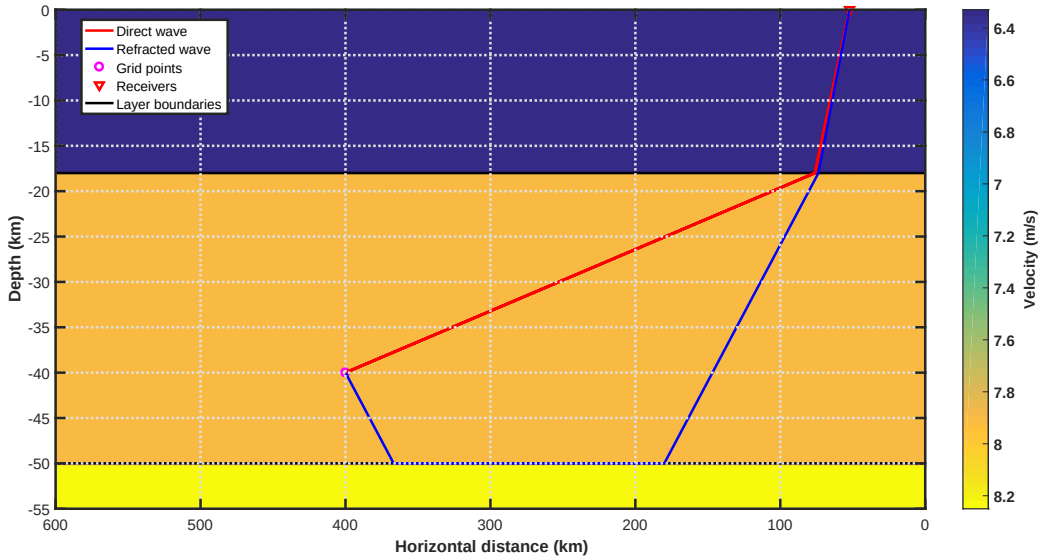

Figure 4.4: Illustrative figure showing direct and refracted ray paths from a source at 40 km depth in layer two to a receiver at the surface in the case of simple three-layered model.

models is more difficult to implement. I therefore focus on the two basic velocity models, i.e., a smooth velocity model and a model consisting of constant velocity layers.

In 1D the two basic velocity models are as in Figure 4.2. The solid lines represent a discontinuous 1D velocity model and the smooth dashed lines a smooth 1D model. Ray tracing for these velocity model are solved in two different manners. The smooth velocity models are, as noted in previous sections, solved using the ray equations. The numerics for these are discussed in Subsection 4.3.5. The discontinuous velocity model, gives rise to ray paths that are reflected, transmitted, or refracted at each layer interface. The ray paths are therefore estimated by a combination of the Pythagoras' theorem and Snell's law (see Figure 4.4). Both models have been used in this thesis. The discontinuous model has been applied for large grid search volumes (because of its computational efficiency) and the smooth models for finer local volumes (due to its computationally demanding nature). It should be emphasized that it is not always clear which type of model works best for a given situation. A combination of the two would most likely provide the best results. Doing this, however, is beyond the scope of this thesis.

4.3.4 Interpolation

In the first basic type of velocity model, i.e., the smoothly varying velocity model on a grid, interpolation is essential. This is because when one solves the ray equations one should be able to determine the velocity and its gradient at any point in the model. Moreover, when tracing many rays it is necessary to do so in an efficient manner.

There are numerous interpolation methods that can be applied. For 1D cases, linear interpolation can be used. The simplest and fastest interpolation methods in 3D are nearest-neighbor methods and more advanced interpolation methods are the spline methods. Nearest neighbor methods are fast, but not very attractive because they are discontinuous along cell boundaries. Spline methods, in contrast, are relatively slow but accurate. In this thesis I have chosen to use linear interpolation for ray tracing through the 1D velocity model and tri-linear interpolation for ray tracing through the 3D velocity model. Tri-linear is attractive because it is continuous along cell boundaries and still relatively fast (i.e. faster than spline methods).

The interpolation problem is discussed in detail in different books, e.g. Press et al. (1992) and Sauer (2014). The 1D and 3D linear interpolation methods discussed in the two following subsections are derived based on information gathered from these.

1D Linear Interpolation

Linear interpolation uses a linear interpolation function to estimate the function value of a data point. It needs at least two discrete data points to construct the line and to estimate the unknown function value. This is illustrated in Figure 4.5, where two data points, (x_1, f_1) and (x_2, f_2), are assumed known and we have to compute the unknown function value f at a known value x. Note that the third data point, x, has to be between the two known points, i.e., $x_1 < x < x_2$, and that f is a function of x, $f(x_i) = f_i$. The unknown function value is found by the ratio of the distance at each axis between the data points

$$\frac{f - f_1}{x - x_1} = \frac{f_2 - f_1}{x_2 - x_1}, \tag{4.26}$$

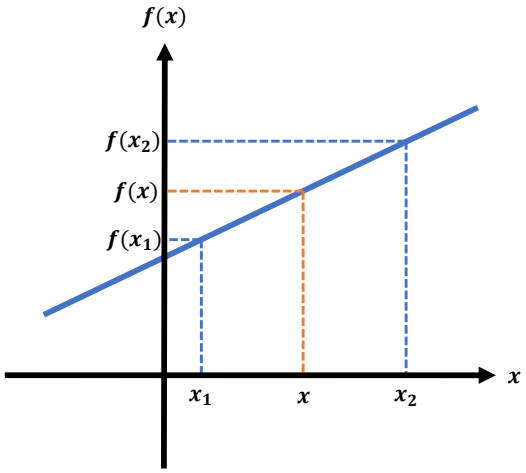

Figure 4.5: Figure that defines the parameters that are used in the 1D interpolation problem.

which is solved for the unknown function value, f,

$$f = f_1 + \frac{f_2 - f_1}{x_2 - x_1}(x - x_1). \tag{4.27}$$

3D Linear Interpolation

The 3D, tri-linear interpolation, is used to estimate the function value, $f(x, y, z)$, at a point (x, y, z) within a local rectangular prism. The prism is constructed by eight grid points in a regular grid. The vertices of the prism are denoted by (x_i, y_i, z_i) for $i = 0, 1$ with associated function values $f(x_i, y_i, z_i)$ (see Figure 4.6a).

First, the ratio between the distances of the different axis to the point, x_r, y_r, z_r, are found

$$\begin{aligned} x_r &= \frac{x - x_0}{x_1 - x_0} \\ y_r &= \frac{y - y_0}{y_1 - y_0} \\ z_r &= \frac{z - z_0}{z_1 - z_0} \end{aligned} \tag{4.28}$$

where x_0 denotes the point lower than x, and x_1 the higher point (similar for y and z).

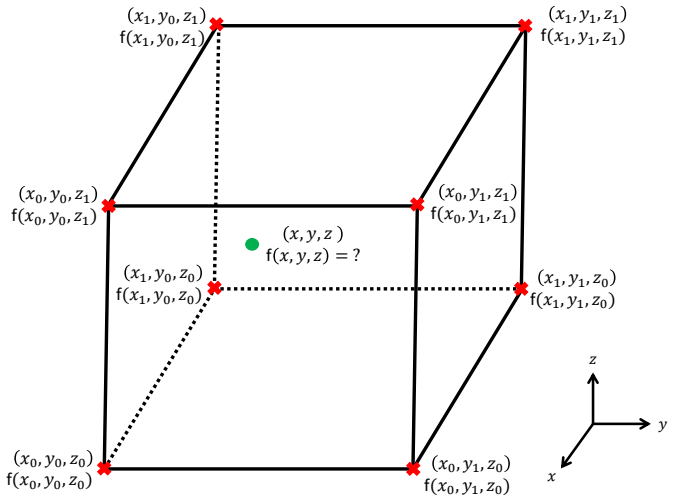

(a) The red stars indicate the known vertices of the prism, and the green dot the interpolation point.

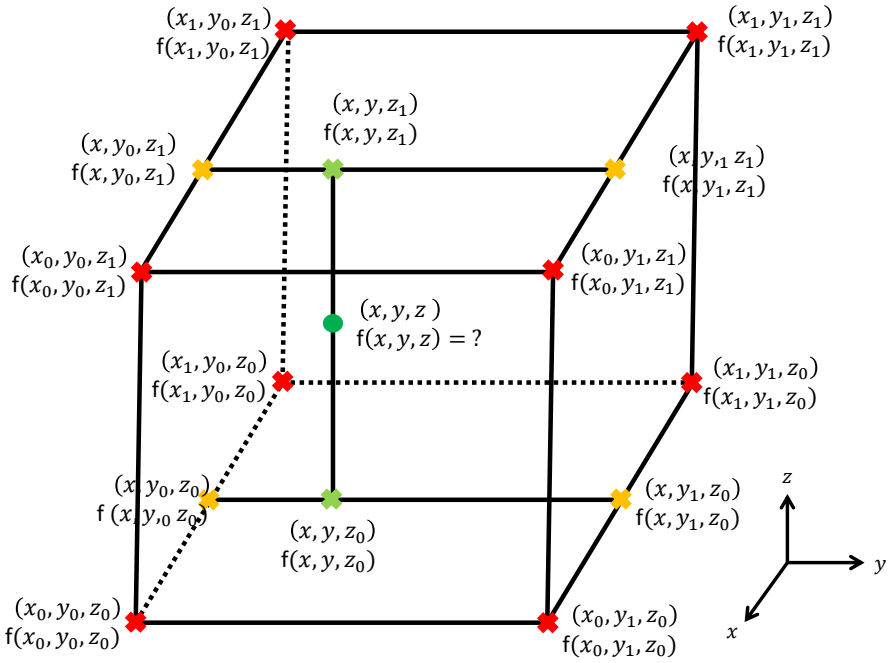

(b) The lines from (x, y_0, z_1) to (x, y_1, z_1), from (x, y, z_0) to (x, y, z_1), and from (x, y_0, z_0) to (x, y_1, z_0) are used in the tri-linear interpolation algorithm.

Figure 4.6: Figure that defines the parameters used in tri-linear interpolation.

The interpolation is first executed along the x-axis,

$$\begin{aligned} f(x_0, y, z_0) &= f(x_0, y_0, z_0)(1 - x_r) + f(x_1, y_0, z_0)x_r \\ f(x_0, y, z_1) &= f(x_0, y_0, z_1)(1 - x_r) + f(x_1, y_0, z_1)x_r \\ f(x_1, y, z_0) &= f(x_0, y_1, z_0)(1 - x_r) + f(x_1, y_1, z_0)x_r \\ f(x_1, y, z_1) &= f(x_0, y_1, z_1)(1 - x_r) + f(x_1, y_1, z_1)x_r. \end{aligned} \tag{4.29}$$

Then, interpolation along the y-axis is done,

$$\begin{aligned} f(x, y, z_0) &= f(x, y_0, z_0)(1 - y_r) + f(x, y_1, z_0)y_r \\ f(x, y, z_1) &= f(x, y_0, z_1)(1 - y_r) + f(x, y_1, z_1)y_r, \end{aligned} \tag{4.30}$$

finally along the z-axis, to find the function value at the wanted interpolation point

$$f(x, y, z) = f(x, y, z_0)(1 - z_r) + f(x, y, z_1)z_r. \tag{4.31}$$

The interpolation process is illustrated in Figure 4.6b. It is important to point out that tri-linear interpolation is not a linear interpolation method but a special type of a cubic interpolation method (i.e. the interpolation function is a polynomial in terms of xyz, xy, xz, yz, x, y and z).

4.3.5 Numerical Solution of the Ray Equations

As noted in Section 4.2.3 ray tracing involves solving the ordinary differential equation (4.20) and (4.21), with a set of initial conditions for velocity, take-off angles and slowness (see equations 4.22 and 4.23).

The numerical solution of the ray equations are calculated by applying the definition of first order derivatives

$$\frac{\mathbf{x}_{i+1} - \mathbf{x}_i}{\Delta t} = c^2(\mathbf{x}_i)\mathbf{p}_i, \tag{4.32}$$

$$\frac{\mathbf{p}_{i+1} - \mathbf{p}_i}{\Delta t} = -\frac{1}{c(\mathbf{x}_i)}\frac{\partial c(\mathbf{x}_i)}{\partial \mathbf{x}}. \tag{4.33}$$

These equations are rearranged to solve for their unknowns $\mathbf{x}_{i+1}$ and $\mathbf{p}_{i+1}$

$$\mathbf{x}_{i+1} = \mathbf{x}_i + \Delta t\, c^2(\mathbf{x}_i)\mathbf{p}_i, \tag{4.34}$$

$$\mathbf{p}_{i+1} = \mathbf{p}_i - \Delta t \left(\frac{1}{c(\mathbf{x}_i)}\frac{\partial c(\mathbf{x}_i)}{\partial \mathbf{x}} \right). \tag{4.35}$$

Equations (4.34) and (4.35) are solved with the standard Euler method, which represents the simplest way of solving the ray equations numerically. However, the ray equations in this thesis are solved by the modified Euler method (also known as symplectic Euler method). This means that the newly calculated position along the ray, $\mathbf{x}_{i+1}$, is used instead of the previous, $\mathbf{x}_i$, in the equation for the slowness vector (4.35). That is

$$\mathbf{x}_{i+1} = \mathbf{x}_i + \Delta t\, c^2(\mathbf{x}_i)\mathbf{p}_i, \tag{4.36}$$

$$\mathbf{p}_{i+1} = \mathbf{p}_i - \Delta t \left(\frac{1}{c(\mathbf{x}_{i+1})} \frac{\partial c(\mathbf{x}_{i+1})}{\partial \mathbf{x}} \right), \tag{4.37}$$

which has been shown to be more accurate than the standard Euler method (Sauer, 2014). More sophisticated methods used to solve the ray equations exist, e.g., the midpoint method and the Runge-Kutta methods. Comparison of these methods with the modified Euler method is interesting and has been done by Newrkla et al. (2019, manuscript submitted) for ray tracing on a global scale.

4.3.6 One-Point and Two-Point Ray Tracing

The modified Euler method of solving the ray equations, discussed in the previous section are used to conduct one-point and two-point ray tracing.

One-point ray tracing estimates the ray path from the source, in the direction specified by take-off angle pairs, to the surface. Figure 4.7 shows an example of one-point ray tracing, using the 1D velocity model of south-western Iceland.

In contrast to one-point ray tracing, two-point ray tracing estimates the ray path from the source to a known receiver position at the surface. This is more complicated than one-point ray-tracing as the take-off angles at the source are unknown and need to be determined.

To estimate the take-off angles an iterative interpolation method is used. First, a number of one-point ray paths for different take-off angles are calculated. Each take-off angle corresponds to a specific ray, with a specific intersection point at the surface (indicated by the magenta stars in Figure 4.7). The magenta stars are then used in a triangulation procedure, called Delaunay triangulation (De Berg et al., 1997), where triangles surrounding the receiver positions are determined (see Figures 4.8 and 4.9). The magenta stars at the

vertices of the triangles have known take-off angles. Linear interpolation is then applied to estimate the unknown take-off angles associated with a ray intersecting the surface at the receiver position.

Figures 4.8 and 4.9 illustrates how the triangulation procedure is executed in practice. Receivers are indicated by blue triangles, located within some Delaunay triangles. The take-off angle pair that estimates the ray path to the receiver within the triangle is computed by applying interpolation to the end points of the triangle. These are indicated by magenta stars in the figure. If the ray intersects the surface sufficiently close to the receiver, the ray path is accepted and the travel time from the source to the receiver is estimated. However, if the surface intersection is not close enough, the failed intersection point will be used as a new end point in a new triangle and a new take-off angle pair is calculated. This procedure is repeated until a wanted accuracy is reached, and a result similar to Figure 4.10 is obtained, creating an iterative method.

The accuracy in the two-point ray tracing depends on the number of iterations and the number of take-off angles used. The more take-off angles are included in the initial calculations, the more accurate the method is, but at the cost that the procedure is more computationally demanding. In practice, two iterations of the two-point ray tracing algorithm are enough.

One- and two-point ray tracing for the 3D of Jan Mayen has also been performed. These are shown in Figures 4.11 and 4.12. The one-point ray tracing shows that the ray paths is curved near the surface. This is because of the low velocities in the upper kilometers of the model. It should be noted that the 3D velocity model has been derived from a 2D velocity profile. Therefore, the velocity model might not be accurate for the entire region.

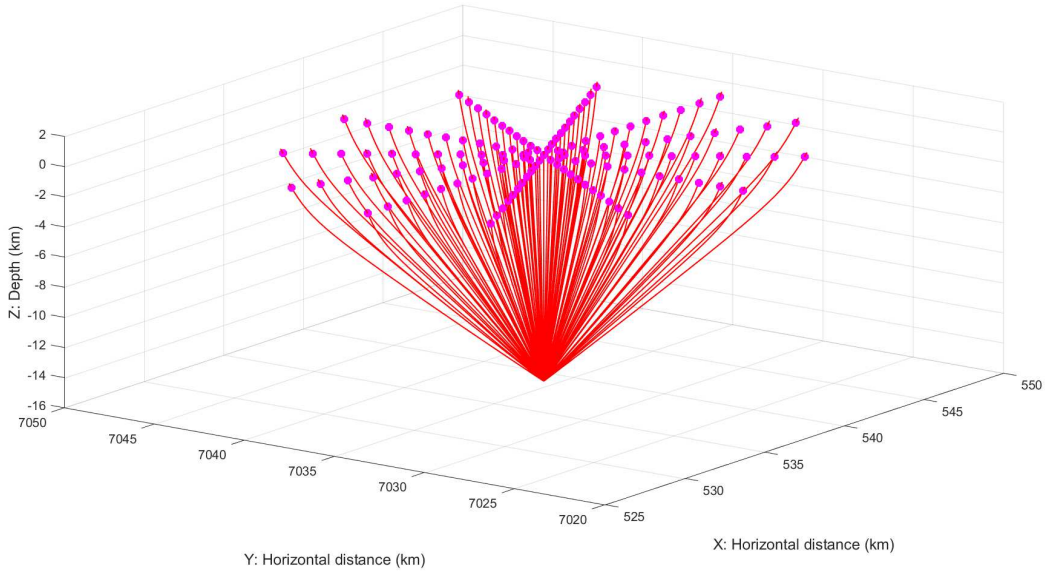

Figure 4.7: One-point ray tracing result using the 1D velocity model for south-west Iceland (see figure 4.2a)

.

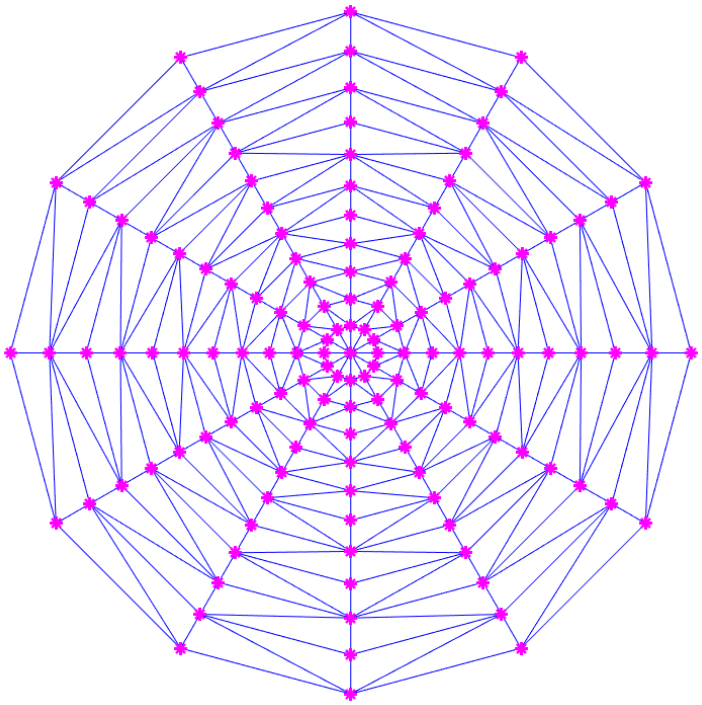

Figure 4.8: Illustrative figure showing Delaunay triangles created by triangulating the points where the rays intersects with the surface.

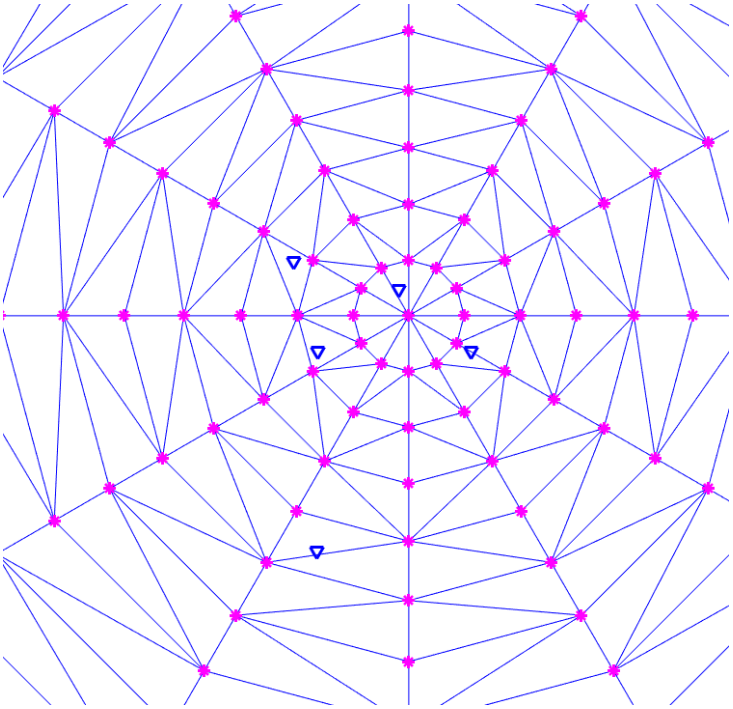

Figure 4.9: Illustrative figure showing Delaunay triangulation. The vertices of the triangles (magenta stars) are used to estimate the take-off angles that give the ray paths to the receiver positions (blue triangles).

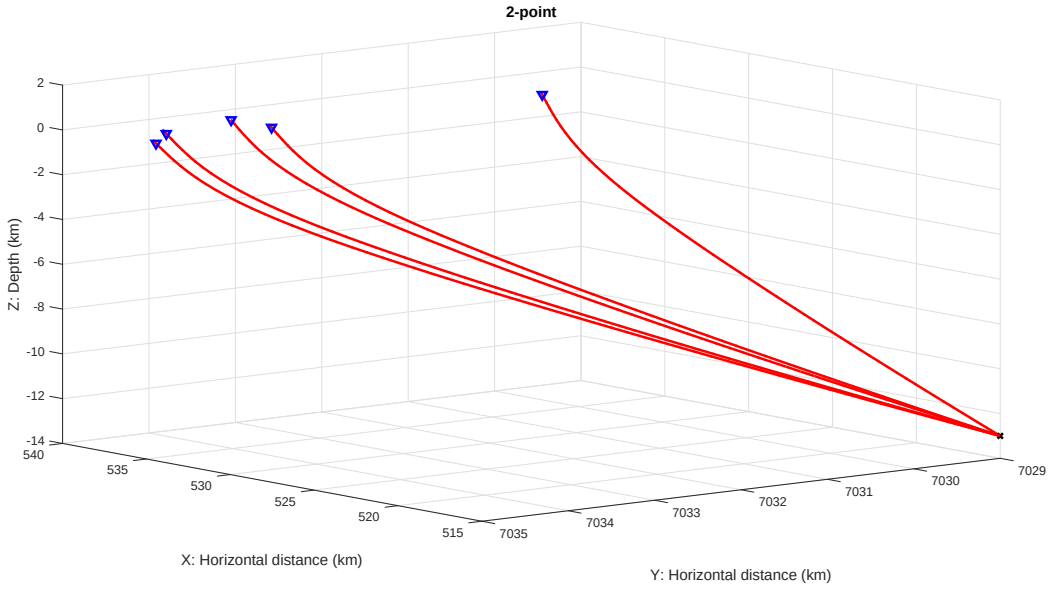

Figure 4.10: Two-point ray tracing example, using the station geometry at Heimaey. The rays travel from a source to five stations (blue triangles).

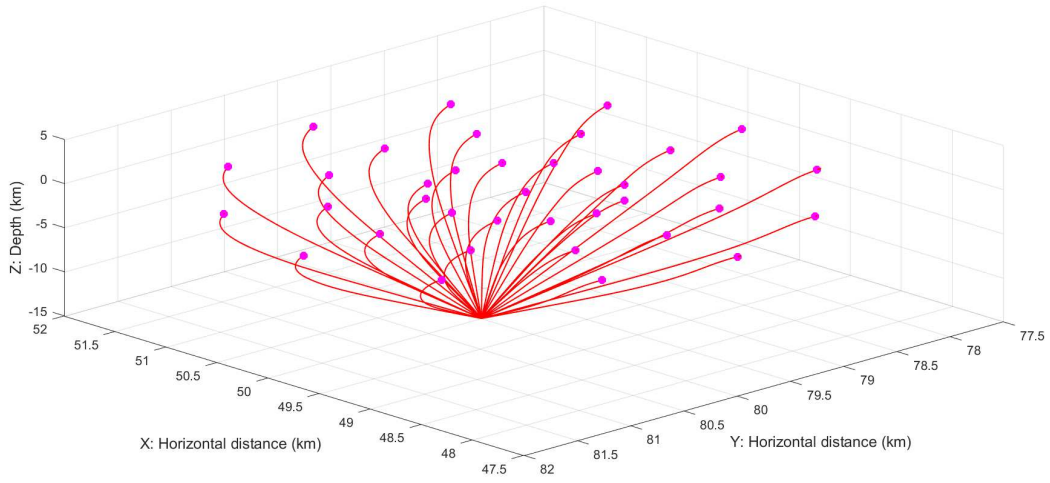

Figure 4.11: One-point ray tracing results using the 3D velocity model of Jan Mayen (see figure 4.3).

.

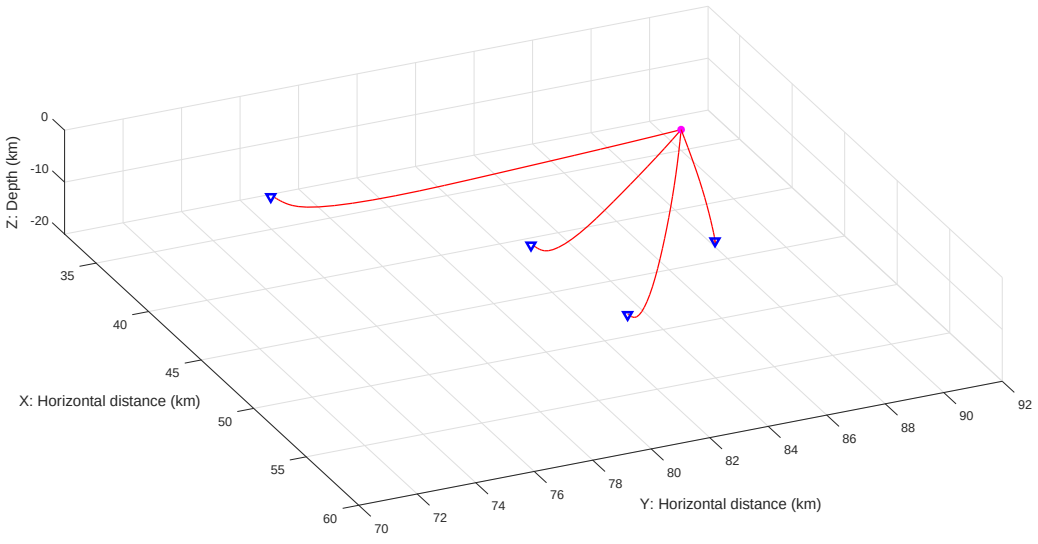

Figure 4.12: Two-point ray tracing results using the 3D velocity model of Jan Mayen. The rays travel from a source to four stations (blue triangles) (see figure 4.3).

.

Chapter 5

Earthquake Location Procedures

This chapter provides the theoretical background used to solve the earthquake location problem. Section 5.1 introduces the earthquake location problem. Then, the different relocation methods are described in Section 5.2. The chapter finishes with Section 5.3, where various synthetic tests for the different methods are discussed.

5.1 The earthquake location problem

The earthquake location problem is an estimation of the spatial coordinates and origin time, $\mathbf{x} = (x, y, z, \tau)$, of a source that generates seismic energy recorded at seismic stations.

Theoretical approximations of the observed arrival times are required, to be able to find the hypocenter and origin time of the seismic source. These theoretical arrival times are compared to the observed arrival times and can be computed by different ray tracing procedures (as discussed in Chapter 4).

A homogeneous medium with P-velocities v_p and S-velocities v_s is the simplest model in which one can use ray tracing to determine the origin time and source location. In this approach, the arrival times recorded at a seismic receiver i, $\mathbf{x}_i = (x_i, y_i, z_i)$, for a seismic source k, $\mathbf{x}_k = (x_k, y_k, z_k)$, with origin time τ_k, are given by

$$t^p_{k,i} = \tau_k + \frac{d(\mathbf{x}_k, \mathbf{x}_i)}{v_p} = \tau_k + T^p_{const}(\mathbf{x}_k, \mathbf{x}_i), \tag{5.1}$$

$$t^s_{k,i} = \tau_k + \frac{d(\mathbf{x}_k, \mathbf{x}_i)}{v_s} = \tau_k + T^s_{const}(\mathbf{x}_k, \mathbf{x}_i), \tag{5.2}$$

where $d(\mathbf{x}_k, \mathbf{x}_i)$ denotes the straight line distance between source and receiver. Note that even in the simplest case, the travel time is nonlinearly related to distance.

Another procedure for arrival time approximation appears when a medium with a general velocity field $v(\mathbf{x})$ is considered. Travel time computations become more complicated and can be expressed as a path integral along the ray path S (see Chapter 4). The travel time for the velocity field is represented as

$$T(\mathbf{x}_k, \mathbf{x}_i) = \int_S u(\mathbf{x}) d\mathbf{x}, \tag{5.3}$$

where $d\mathbf{x}$ is an element of the path length and $u(\mathbf{x}) = 1/v(\mathbf{x})$ is the slowness field for either P-waves or S-waves. The arrival time is then given by

$$t_{k,i} = \tau_k + T(\mathbf{x}_k, \mathbf{x}_i). \tag{5.4}$$

Changing the source location in equation 5.3 results in a change in the ray path that the integral is evaluated for (Li, 2017). This represents a non-linear change in travel time computation. Hence, equation 5.3 and 5.4 are non-linear equations for t as a function of source position $\mathbf{x}$. On the basis of these two arrival time estimation procedures, it is therefore shown that the earthquake location problem is a non-linear problem. Note that when a heterogeneous model is used conversion of waves may occur. This is, however, will not be included in this thesis [(Stein and Wysession, 2003); (Li, 2017)].

The non-linear earthquake location problem can be formulated as an inverse problem using the observed phases and unknown model parameters. When n arrival time observations are available, a data vector $\mathbf{d}^{obs}$ can be constructed

$$\mathbf{d}^{obs} = [t_1, t_2, \cdots, t_n]^T, \tag{5.5}$$

where $\mathbf{d}^{obs}$ contains the different observed arrival times, t, and the upper-case letter T denotes the transpose of a vector/matrix. The unknown spatial coordinates and origin time are represented as the model vector $\mathbf{m}$,

$$\mathbf{m} = [x, y, z, \tau]^T. \tag{5.6}$$

Another representation of equations (5.1) and (5.4) is

$$\mathbf{d}^{obs} = F(\mathbf{m}), \tag{5.7}$$

where the non-linear function $F(\mathbf{m})$ predicts the observed data for a given or assumed model parameters. The inverse problem is $\mathbf{m} = F^{-1}(\mathbf{d})$, which is a highly non-linear problem. Due to the difficulty of solving non-linear problems, approximations are often applied to solve the earthquake location problem. In a linear iterative method, first-order Taylor expansions are used to find linear approximations to the non-linear function. A second-order Taylor expansion can be used to formulate a quadratic inversion scheme. An alternative to these linearized, but approximate, solutions of the inverse problem is to do a grid search. Both the linearized inversion and the grid search are discussed in the next section.

5.2 The Earthquake Location Methods

The earthquake locations in this thesis are computed using phase picks from seismograms recorded at different seismic receivers. Absolute arrival times for P- and S-phases are read from the seismograms, and together with local velocity models for P- and S-wave, used to solve the earthquake location problem.

In this section, I present the methods used to solve the earthquake location problem. The hypocenter locations are estimated by three different methods. The first uses the linearized inversion method available in SEISAN. The second uses P- and S-waves to relocate the earthquake and is similar to the traditional grid search method (Havskov and Ottemöller, 2010). The third uses interstation single-differences for P-waves, combined with interstation single S-P differences (referred to as the single-difference method). These three methods are described in the next subsections.

5.2.1 HYPOCENTER - a SEISAN hypocenter location method

One of the methods available in SEISAN estimates earthquake locations using a modified version of the HYPOCENTER location package (Ottemöller et al., 2017). All catalog events referred to in this thesis are located by this method. HYPOCENTER locates an event by a modified linearized iterative inversion method. The modifications include adaptive damping (see Lienert et al. (1986) for more information). The linearized iterative

inversion introduced by Geiger (1912) was implemented in this thesis to understand the theory behind the HYPOCENTER program better. This linearized inversion is described in the next subsection.

Linear iterative inversion

The linear inversion method starts with an initial guess, or a starting model, of the model parameter, $\mathbf{m}_0 = (x_0, y_0, z_0, \tau_0)$. This starting model initiates an iterative method used to estimate the unknown hypocenter position and origin time, $\mathbf{m} = (x, y, z, \tau)$, of an earthquake. As discussed in Section 5.1 the observed arrival time can be related to a hypocenter and an origin time by

$$t_{k,i}^{obs} = T(\mathbf{x}_k, \mathbf{x}_i) + \tau, \tag{5.8}$$

or, in vector notation, by

$$\mathbf{t}^{obs} = \mathbf{f}(\mathbf{m}). \tag{5.9}$$

The starting model is a guess of a hypocenter that is sufficiently close to the true solution, which predicts the observed arrival time. The starting model in the linearized inversion method available in SEISAN applies a starting location algorithm that tests the rms for different starting locations. The location with the smallest rms is chosen as the starting position. The arrival times predicted by the starting model are rarely the true observed times, so a change in the starting model that makes the predicted data closer to the observed needs to be computed

$$\mathbf{m}_1 = \mathbf{m}_0 + \delta\mathbf{m}. \tag{5.10}$$

The new model parameter is then inserted into equation 5.9

$$\mathbf{t}^{obs} = \mathbf{f}(\mathbf{m}_1) = \mathbf{f}(\mathbf{m}_0 + \delta\mathbf{m}). \tag{5.11}$$

Function $\mathbf{f}(\mathbf{m}_0 + \delta\mathbf{m})$ can then be linearized by a first order Taylor expansion around the starting model

$$\mathbf{t}^{obs} \approx \mathbf{f}(\mathbf{m}_0) + \left.\frac{\partial \mathbf{f}(\mathbf{m}_0)}{\partial \mathbf{m}}\right|_{m_0} \delta\mathbf{m}_0. \tag{5.12}$$

This can be rewritten as

$$\delta\mathbf{t}_0 = \mathbf{t}^{obs} - \mathbf{t}_0^{cal} \approx \left.\frac{\partial \mathbf{f}(\mathbf{m}_0)}{\partial \mathbf{m}}\right|_{m_0} \delta\mathbf{m}_0, \tag{5.13}$$

where $\delta \mathbf{t}_0$ is the residual for the travel time. For simplicity, the partial derivative matrix is denoted by

$$G = \frac{\partial \mathbf{f}(\mathbf{m}_0)}{\partial \mathbf{m}}. \tag{5.14}$$

Note that the partial derivatives are functions of the spatial variables (x, y, z), whereas the last partial derivative with respect to origin time is

$$\frac{\partial \mathbf{f}(\mathbf{m}_0)}{\partial m_4} = \frac{\partial \mathbf{f}(x_0, y_0, z_0, \tau_0)}{\partial \tau} = \mathbf{1}. \tag{5.15}$$

Generalized for n receivers, the matrix equation relating travel time residuals and model parameters is

$$\begin{bmatrix} \delta t_1 \\ \delta t_2 \\ \delta t_3 \\ \vdots \\ \delta t_n \end{bmatrix} = \begin{bmatrix} \frac{\partial t_1}{\partial x} & \frac{\partial t_1}{\partial y} & \frac{\partial t_1}{\partial z} & 1 \\ \frac{\partial t_2}{\partial x} & \frac{\partial t_2}{\partial y} & \frac{\partial t_2}{\partial z} & 1 \\ \frac{\partial t_3}{\partial x} & \frac{\partial t_3}{\partial y} & \frac{\partial t_3}{\partial z} & 1 \\ \vdots & \vdots & \vdots & \vdots \\ \frac{\partial t_n}{\partial x} & \frac{\partial t_n}{\partial y} & \frac{\partial t_n}{\partial z} & 1 \end{bmatrix} \begin{bmatrix} \Delta x \\ \Delta y \\ \Delta z \\ \Delta \tau \end{bmatrix} \tag{5.16}$$

Equation (5.16) is a system of linear equations. Because there are more observations than unknowns, the problem is overdetermined and can not be solved by inverting the partial derivative matrix. The change in model parameters is found by multiplying both sides of the equation by the transposed partial derivative matrix

$$G^T \delta \mathbf{t}_0 = (G^T G) \delta \mathbf{m}_0. \tag{5.17}$$

This creates the square matrix $(G^T G)$, which can be inverted. This is equivalent to performing a least square inversion of equation (5.16). The change in the model parameters can then be estimated by

$$\delta \mathbf{m}_0 = (G^T G)^{-1} G^T \delta \mathbf{t}_0. \tag{5.18}$$

The operator $(G^T G)^{-1} G^T$ is called the generalized inverse and denoted by G^{-g}

$$\delta \mathbf{m}_0 = G^{-g} \delta \mathbf{t}_0. \tag{5.19}$$

The new model parameter is

$$\mathbf{m}_1 = \delta \mathbf{m}_0 + \mathbf{m}_0, \tag{5.20}$$

and the arrival times are found

$$\mathbf{t}_1 = \mathbf{f}(\mathbf{m}_1) \tag{5.21}$$

that is closer to the observed values. If this new hypocenter value has the desired misfit, $\mathbf{m}^1$ is set to be the event hypocenter. If not the procedure is repeated until the desired misfit is reached [e.g. (Geiger, 1912); (Stein and Wysession, 2003)].

5.2.2 Grid Search using P- and S-wave arrivals

A systematic grid search computes all possible locations in a survey area to estimate the earthquake location. It should be noted that this method is computationally demanding. Increasing computer power and technology, however, has made it more efficient and practical (Lomax et al., 2009).

The grid search procedure starts by dividing the area assumed to contain the earthquake into discrete grid points. It estimates potential source locations at these grid points, and the true hypocenter location is found at the point where the misfit has a minimum. The misfit is denoted by $M(x, y, z)$, and calculated by the squared residual at each grid point (x, y, z)

$$M(x, y, z) = \left(\frac{\sum_{i=1}^{n} r_i^2(x, y, z)}{n} \right)^{1/2}. \tag{5.22}$$

The station residual is given by

$$r_i(x, y, z) = t_i^{obs} - t_i^{cal}(x, y, z) = t_i^{obs} - (T_i^{cal}(x, y, z) + \tau_0), \tag{5.23}$$

where $t_i^{cal}(x, y, z)$ is the calculated arrival time at station i for a hypothetical event at each grid point, $T_i^{cal}(x, y, z)$ is the travel time, and τ_0 is the unknown origin time, which is determined in an average manner using all observations (discussed later) (Havskov and Ottemöller, 2010).

In this section, two grid search methods are described, the traditional grid search method and the single-difference grid search method. The traditional method compares observed arrival times at different receivers with computed arrival times for each grid point to the same receivers (as in equations (5.22) and (5.23)). This is done for both P- and S-arrival times. The second grid search method combines two alternative grid searches. The first compares observed and calculated interstation arrival time pairs of the same phase, i.e., comparing P-observed and P-calculated arrival time differences for all station pairs. This method is referred to as the interstation single P-P difference method, or simply single

P-P difference. The second method compares the observed and calculated interstation S-P differences for all station combinations, and is referred to as the single S-P difference. By combining the single P-P difference and single S-P difference, the second grid search method used in this thesis is generated. This is called the single-difference method.

The reason for applying the single-difference grid search method is to investigate an alternative way of estimating earthquake locations using sparse station networks. The single P-P difference produces direction sensitive earthquake locations, whereas the single S-P difference produces distance sensitive earthquake locations. By combining these two methods a method constrained both in direction and distance is developed. All this will be shown in the synthetic test presented in Section 5.3.

Now that the methods have been discussed, the equations for the different misfit functions are derived. Both methods assume that an earthquake is recorded at n seismic receivers, and that the absolute arrival times at the receivers are denoted as $t_i^{P_{obs}}$ $(i = 1, \ldots, n)$ and $t_i^{S_{obs}}$ $(i = 1, \ldots, n)$, for the P- and S-waves respectively. To estimate the location of the earthquake using the single-difference grid searches method, P- and S-observed arrival times are combined to produce interstation arrival time differences for the seismic stations. The observed ΔPP^{obs} and ΔSP^{obs} arrival time differences are respectively defined by

$$\delta t_{ij}^{\Delta PP_{obs}} = t_i^{P_{obs}} - t_j^{P_{obs}}, \quad j \neq i \tag{5.24}$$

$$\delta t_{ij}^{\Delta SP_{obs}} = t_i^{S_{obs}} - t_j^{P_{obs}}, \tag{5.25}$$

where i and j denote the indexes for the seismic stations, $i \in [1, ..., n]$ and $j \in [1, ..., n]$. From the equations above, it should be noted that the maximum number of combinations varies. For the single difference ΔPP there are a total of $n^2 - n$ combinations possible (as similar phase arrivals at the same station equal zero and therefore not included), whereas ΔSP has n^2 possible combinations.

The area of interest consists of $n_x n_y n_z$ equally spaced theoretical grid points, where n_x is the number of grid points in the x-direction, n_y the number of grid points in the y-direction and n_z the number of grid points in the z-direction. For each grid point, the P- and S-wave travel- and arrival-times to the n receivers are estimated and the differences

in arrival times computed. The computed arrival times are estimated by

$$\begin{aligned} t_i^{P_{cal}}(x,y,z) &= \tau^{cal}(x,y,z) + T_i^{P_{cal}}(x,y,z), \\ t_i^{S_{cal}}(x,y,z) &= \tau^{cal}(x,y,z) + T_i^{S_{cal}}(x,y,z), \end{aligned} \tag{5.26}$$

where $\tau^{cal}(x,y,z)$ are the grid point's origin time (discussed later), $T_i^{P_{cal}}(x,y,z)$ and $T_i^{S_{cal}}(x,y,z)$ are the computed travel times from grid point (x,y,z) to receiver i for P- and S-waves, respectively. These are used in the traditional grid search method. For the single-difference method travel time interstation differences are calculated, e.g., for station i and j

$$\begin{aligned} \delta t_{ij}^{\Delta PP_{cal}}(x,y,z) &= t_i^{P_{cal}}(x,y,z) - t_j^{P_{cal}}(x,y,z) \\ &= \tau^{cal}(x,y,z) + T_i^{P_{cal}}(x,y,z) - (\tau^{cal}(x,y,z) + T_j^{P_{cal}}(x,y,z)) \\ &= T_i^{P_{cal}}(x,y,z) - T_j^{P_{cal}}(x,y,z). \end{aligned} \tag{5.27}$$

Note that the $\delta t_{ij}^{\Delta PP_{cal}}$ and $\delta t_{ij}^{\Delta SP_{cal}}$ are independent of the origin time τ^{cal}. The same is done for the S-P differences

$$\delta t_{ij}^{\Delta SP_{cal}}(x,y,z) = T_i^{S_{cal}}(x,y,z) - T_j^{P_{cal}}(x,y,z). \tag{5.28}$$

Furthermore, the different misfit functions are calculated. For the traditional grid search method the misfit functions are computed using equations (5.22) and (5.23) for the n_p and n_s available P- and S-phases, respectively, yielding the combined misfit function

$$M(x,y,z) = \left(\frac{\sum_{i=1}^{n_p} (t_i^{P_{obs}} - t_i^{P_{cal}}(x,y,z))^2}{n_p} + \frac{\sum_{i=1}^{n_s} (t_i^{S_{obs}} - t_i^{S_{cal}}(x,y,z))^2}{n_s} \right)^{1/2}. \tag{5.29}$$

Then, the single P-P difference misfit functions are computed by summing the differences between the observed and calculated interstation phases for all the available combinations

$$M^{\Delta P}(x,y,z) = \left(\frac{\sum_{i=1}^{n_p} \sum_{j=1}^{n_p} (\delta t_{ij}^{\Delta P_{obs}} - \delta t_{ij}^{\Delta P_{cal}}(x,y,z))^2}{n^2 - n} \right)^{1/2}, \quad i \neq j. \tag{5.30}$$

Finally, the misfit for the S-P differences are computed for all combinations available

$$M^{\Delta SP}(x,y,z) = \left(\frac{\sum_{i=1}^{n_s} \sum_{j=1}^{n_p} (\delta t_{ij}^{\Delta SP_{obs}} - \delta t_{ij}^{\Delta SP_{cal}}(x,y,z))^2}{n^2} \right)^{1/2}. \tag{5.31}$$

Repeating the calculations for every grid point and then determining the minimum of the misfit function gives the estimated source location $\mathbf{x}_s = (x_s, y_s, z_s)$ at the global minimum misfit value.

Origin Time Estimation for the Traditional method

The calculation of the origin time of an event is computed through two iterative steps in the traditional grid search method. The first step computes the origin time for each grid point. This is done by taking the average residual for each grid point using an initial origin time guess for all grid points (here zero is used for all grid points)

$$\begin{aligned} \delta t(x,y,z) &= \delta t^P(x,y,z) + \delta t^S(x,y,z) \\ &= \frac{1}{n_p}\sum_{i=1}^{n_p}(t_i^{P_{obs}} - (\tau_0 + T_i^{P_{cal}}(x,y,z))) + \frac{1}{n_s}\sum_{i=1}^{n_s}(t_i^{S_{obs}} - (\tau_0 + T_i^{S_{cal}}(x,y,z))) \\ &= \frac{1}{n_p}\sum_{i=1}^{n_p}(t_i^{P_{obs}} - T_i^{P_{cal}}(x,y,z)) + \frac{1}{n_s}\sum_{i=1}^{n_s}(t_i^{S_{obs}} - T_i^{S_{cal}}(x,y,z)). \end{aligned} \tag{5.32}$$

The average residual for each grid point, $\delta t(x,y,z)$, corresponds to a time shift that when added to the initial origin time

$$\tau^{cal}(x,y,z) = \tau_0 + \delta t(x,y,z), \tag{5.33}$$

estimates the origin time for each grid point. In the second step, the origin time of the grid point is added to its theoretic travel time to find the computed arrival time. Then, the misfit function is computed by equation (5.29). The global minimum misfit value is the estimated hypocenter location, and the origin time of the grid point is the events estimated origin time (Havskov and Ottemöller, 2010).

Grid Search Origin Time Estimation for the Single-Difference methods

The origin time calculation for the single-difference method is different from the traditional method, as the misfit functions are origin time-independent. First, the hypocenter location is estimated by the misfit function. Then, the travel times from the estimated source to the different receivers are found. By calculating the average residual of these travel times the origin time is found to be

$$\tau^{cal}(\mathbf{x}_s) = \frac{1}{n_r}\sum_{i=1}^{n_r}(t_i^{obs} - t_i(\mathbf{x}_s, \mathbf{x}_r)) \tag{5.34}$$

where $t_i(\mathbf{x}_s, \mathbf{x}_r)$ denotes the travel time from the source to receiver i.

5.2.3 Combination of Single P-P Difference and Single S-P Difference

The single P-P difference and single S-P difference misfit functions result in two different contour plots, as will be shown in the section on synthetic tests. The single P-P difference results in a location that is relatively independent of distance, whereas single S-P difference results in a location that is relatively independent of direction. The aim by combining the single P-P and single S-P difference is to develop a location method which is both distance and direction sensitive. The single-difference method is then compared to the traditional method to check if it provides better location constraints.

To combine the single P-P difference and the single S-P difference in the best possible way, both methods are scaled by their mean value. There are two reasons for doing this. First, the single difference method provides lower misfit values than the S-P, because the P-P difference is smaller than the S-P difference. The second reason is that S-wave picks often are more uncertain than P-wave picks. The misfit function for the combination of single P-P difference and single S-P difference is therefore

$$M^{comb}(x,y,z) = \frac{M^{\Delta PP}(x,y,z)}{\mu^{\Delta PP}} + \frac{M^{\Delta SP}(x,y,z)}{\mu^{\Delta SP}}, \tag{5.35}$$

where μ denotes the average misfit value over the region where the grid search is applied.

The grid searches used in this thesis is executed in two steps. First, a coarse grid search is carried out for the entire region. Then, based on the locations found in the coarse grid search, a finer grid search is executed. This grid search extracts a volume around the location found in the coarse grid search. Finally, the estimated source location is found at the global minimum of the volume.

5.3 Synthetic Tests

This section presents the synthetic tests for the different grid search methods using two station geometries. These synthetic tests are executed to validate that the methods work properly and to investigate how different acquisition geometries affect the results. The first geometry test uses the same station geometry as Jan Mayen, where an event occurs outside

the network (see Figure 5.1a). The second test uses an alternative station geometry with three additional hypothetical stations placed around the synthetic event (see Figure 5.1b).

For synthetic data, the observed arrival times are calculated for a predefined source and an input model. The ray tracing discussed in Chapter 4 is then used to estimate the travel times from the source to the receivers and the associated arrival times. To better understand how the grid search methods behave, a constant velocity medium is used for the tests shown in this section. This way, wavefront distortions caused by a more complex velocity model are avoided. The goal for the synthetic inversion is to find back to the predefined source used to generate the observed data.

The synthetic tests in this section assume a source at $(x_s, y_s, z_s) = (15, 110, -16)$ km and a grid volume consisting of $nx * ny * nz = 85 * 103 * 101 = 884{,}225$ grid points with a grid increment of 0.5 km in all directions.

In the following sections, the resulting contour plots of the misfit functions from the synthetic test are presented. First, the contours for the traditional grid search are shown. Then, contours for the single P-P difference grid search, followed by S-P. Finally in Subsection 5.3.4, the results from the synthetic test for the combination of single P-P difference and single S-P difference are presented.

5.3.1 Traditional Grid Search: Synthetic Test

Figures 5.2, 5.3, 5.4, and 5.5 show the misfit contours for two station geometries using the traditional grid search. These figures are presented to get an impression on how accurate the method is for the different geometries and later compared to the other methods.

Figures 5.2 and 5.4 illustrate the effect the different station geometries have on the horizontal resolution. For the test where the event occurs outside the network, the contours show an elongated ellipse (Figure 5.2), whereas the test for the distributed station network shows a circular shape (Figure 5.4). This means that the area where the event can be located is larger when the event occurs outside the network, compared to inside. These results were anticipated, as a distributed station network generally gives a better constrained earthquake location than a localized network (Havskov and Ottemöller, 2010).

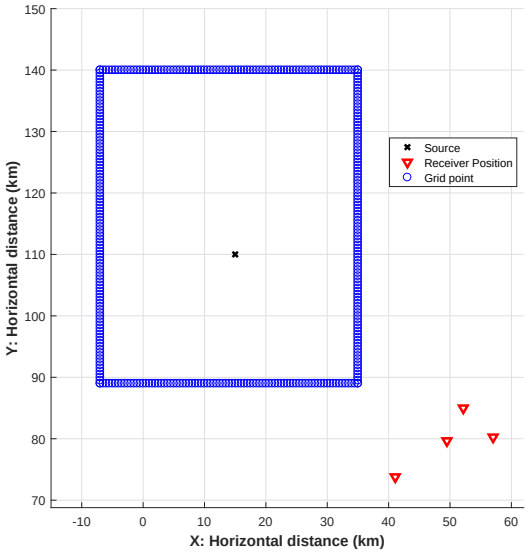

(a) Source located outside the network.

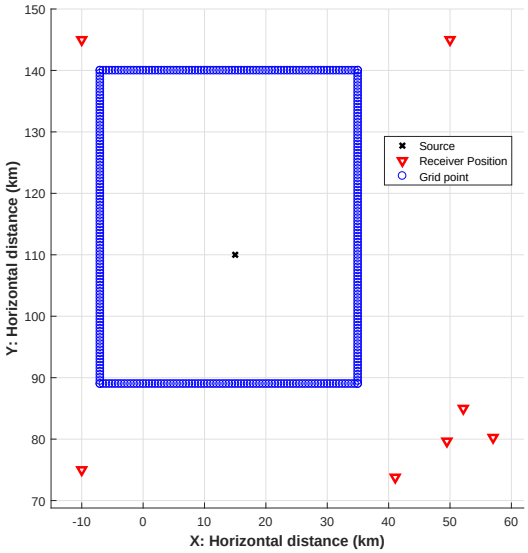

(b) Source located inside the network.

Figure 5.1: The different station geometries for the synthetic tests. The red triangles represents the stations, the black cross the synthetic event and the blue circles the outer edge of the grid search area.

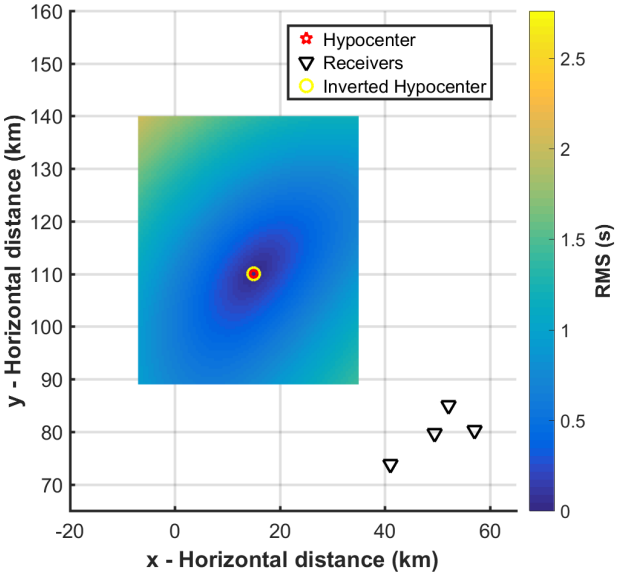

Figure 5.2: Synthetic test for the traditional method using the Jan Mayen network. The earthquake occurring outside the network of stations. Plot of the horizontal plane. P- and S-waves are used.

Figures 5.3 and 5.5 show the depth resolution for the geometries. The hypocenter depth plot for the Jan Mayen network is curved (Figure 5.3). Note that the hypocenter is not as well constrained for the Jan Mayen network as for the distributed network. However, the depth plot is not curved. It is rather observed as a narrow dip (Figure 5.5). Hypocenter depth is known as the most difficult parameter to determine because a change in hypocenter depth does not cause a big change in the travel time (Havskov and Ottemöller, 2010). The misfit contours computed in the tests were, therefore, as expected.

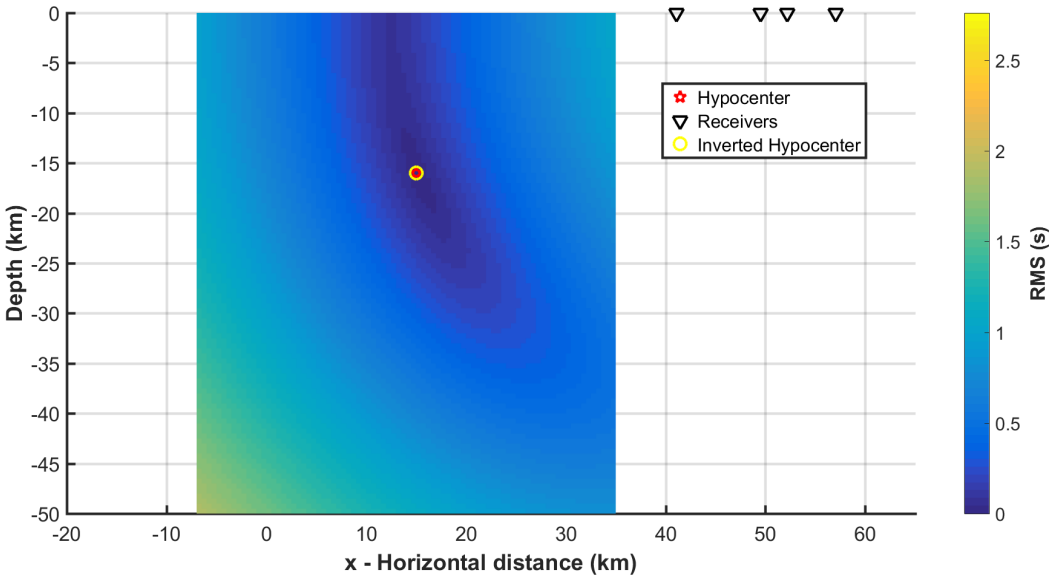

Figure 5.3: Synthetic test for the traditional method using the Jan Mayen network. The earthquake occurs outside the network of stations. Plot of the X-Z plane. P- and S-waves are used.

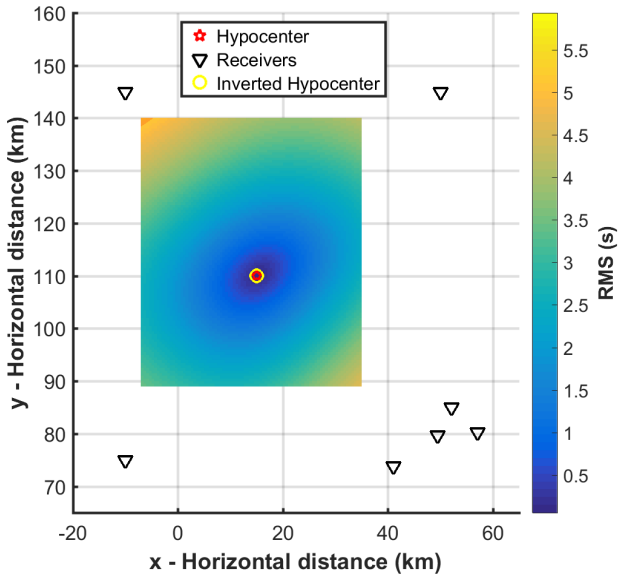

Figure 5.4: Synthetic test for the traditional method using the distributed station network. The earthquake occurs inside the network of stations. Plot of the horizontal plane. P- and S-waves are used.

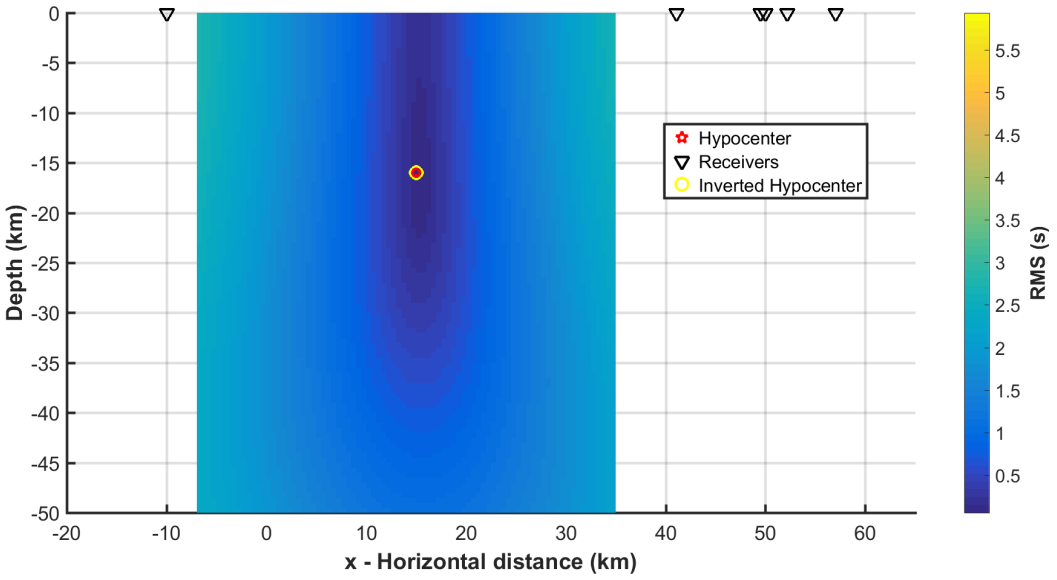

Figure 5.5: Synthetic test for traditional method using the distributed station network. The earthquake occurs inside the network of stations. Plot of the X-Z plane. P- and S-waves are used.

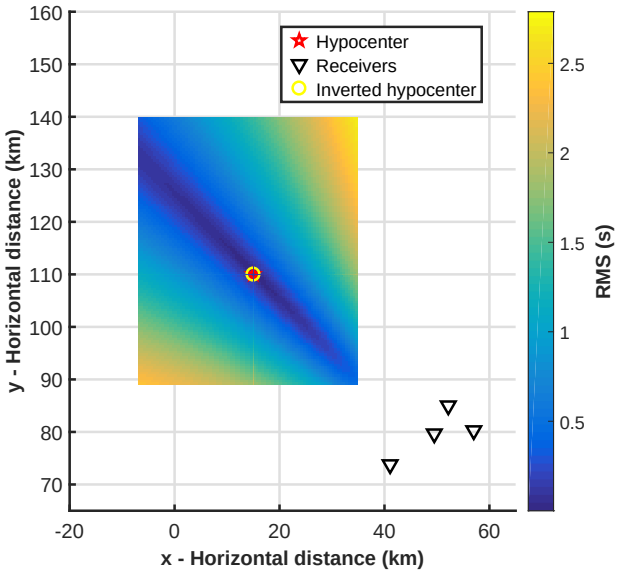

Figure 5.6: Synthetic test for the single P-P difference method using the Jan Mayen network. The earthquake occurs outside the network of stations. Plot of the horizontal plane. Only P-waves are used for this test.

5.3.2 Single P-P Difference: Synthetic Test

The single-difference tests are executed in the same manner as the traditional method. Figures 5.6 and 5.7 show the contour plots for earthquakes happening outside the station network. The horizontal plane shows a beam-like structure radiating from the network of stations (Figure 5.6). It is clear that this method alone provides a good direction constraint, but a poorly constrained location in terms of distance. The depth plot is curved, but in contrast to the traditional method, it curves away from the network (Figure 5.7).

For the synthetic test of earthquakes occurring inside the station network, there are constraints both in distance and direction (Figure 5.8). The horizontal plane in the contour map is similar to the traditional contour map, but the depth resolution is not as good (Figure 5.9).

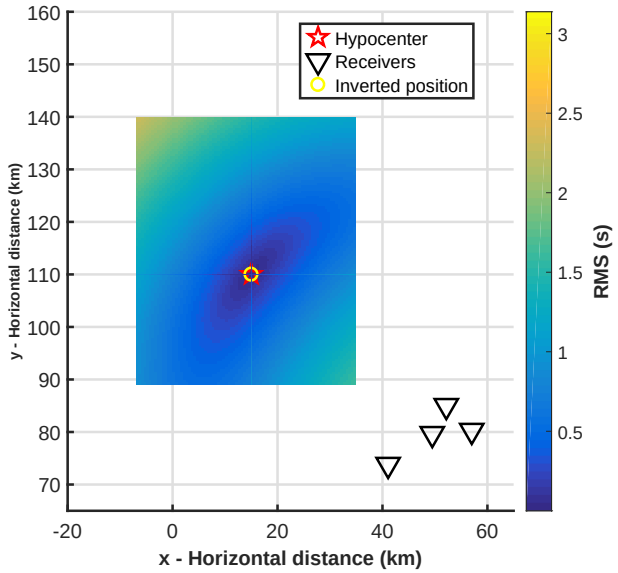

Figure 5.7: Synthetic test for the single P-P difference method using the Jan Mayen network. The earthquake occurs outside the network of stations. Plot of the X-Z plane. Only P-waves are used for this test.

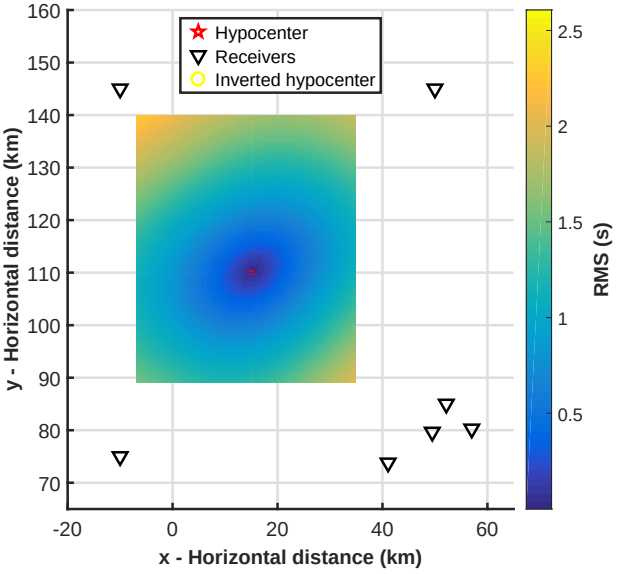

Figure 5.8: Synthetic test for single P-P difference method using the distributed station network. The earthquake occurs inside the network of stations. Plot of the horizontal plane. Only P-waves are used for this test.

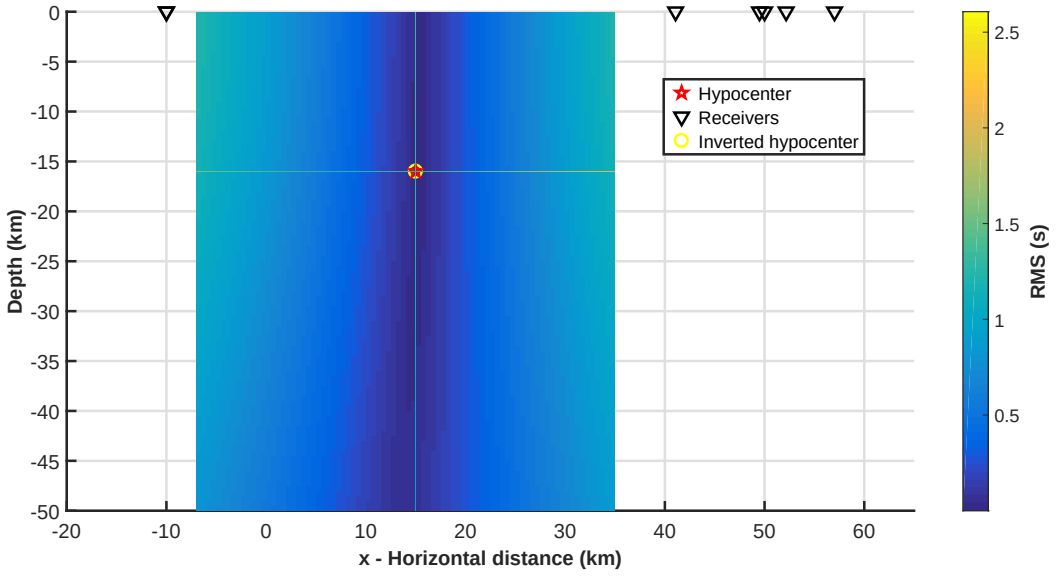

Figure 5.9: Synthetic test for single P-P difference method using the distributed station network. The earthquake occurs inside the network of stations. Plot of the X-Z plane. Only P-waves are used for this test.

5.3.3 Single S-P Difference: Synthetic Test

In this subsection, I present the grid search test results for the S-P difference. Figures 5.10 and 5.11 show S-P contour plots for an event outside the network. The contour plot of the horizontal plane shows an elongated ellipse (Figure 5.10). This elongated contour suggests more sensitivity in distance than direction. The depth plot shows the same shape as the traditional method, curved towards the network of stations (Figure 5.11).

For the test where an event occurs inside the station network, a circular contour shape is found, and a more constrained earthquake location is obtained (Figure 5.12). The depth resolution is better resolved here than in the traditional grid search method (Figure 5.13).

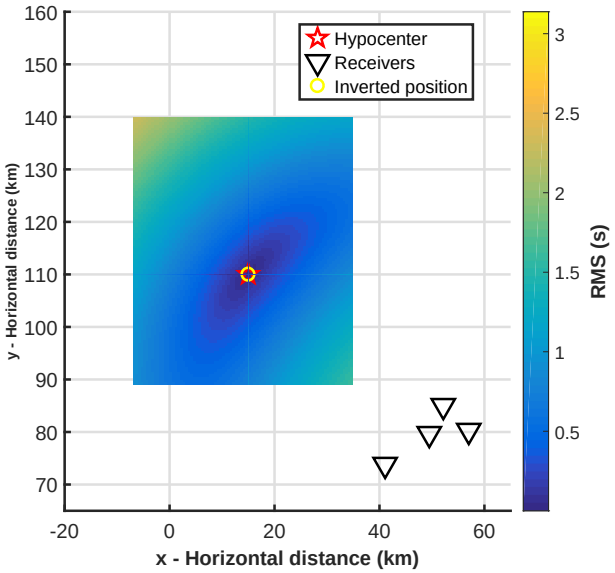

Figure 5.10: Synthetic test for the single S-P difference method using the Jan Mayen network. The earthquake occurs outside the network of station. Plot of the horizontal plane. Both P-waves and S-waves are used.

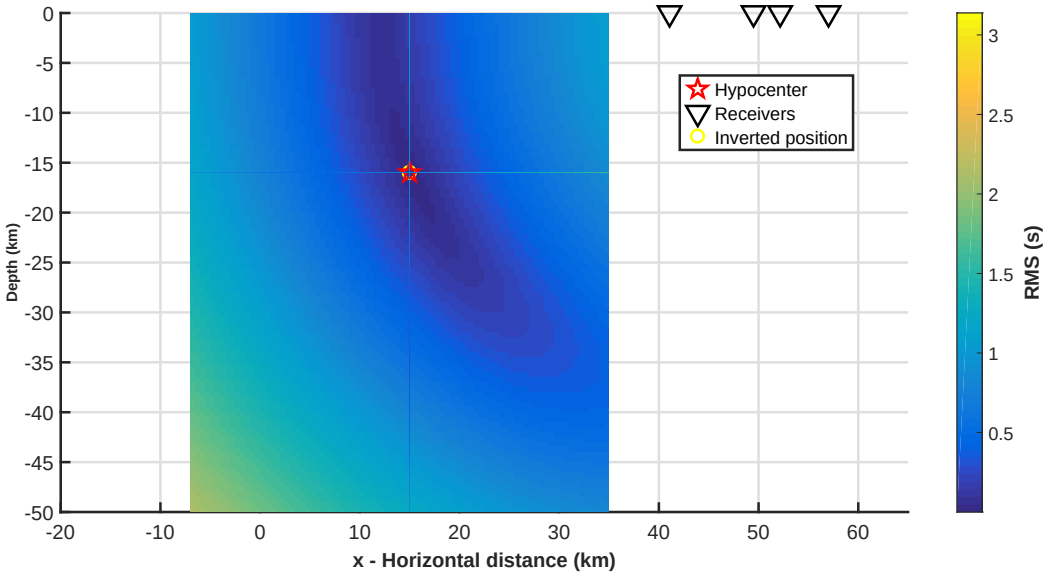

Figure 5.11: Synthetic test for the single S-P difference method using the Jan Mayen network. The earthquake occurs outside the network of stations. Plot of the X-Z plane. Both P-waves and S-waves are used.

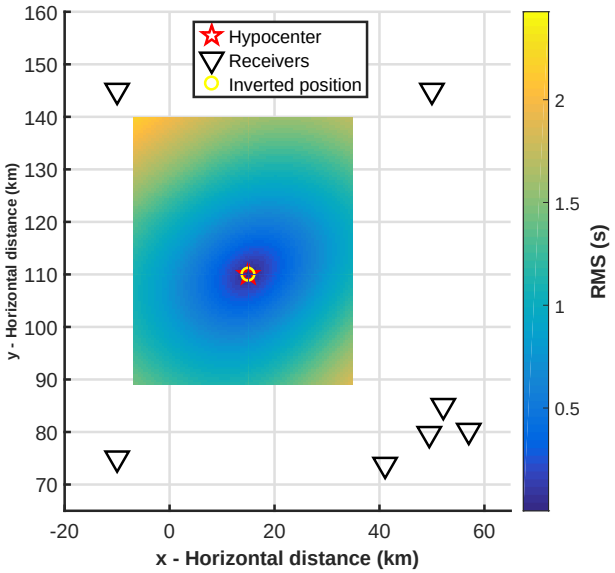

Figure 5.12: Synthetic test for the single S-P difference grid search method using the distributed station network. The earthquake occurs inside the network of stations. Plot of the horizontal plane. Both P-waves and S-waves are used.

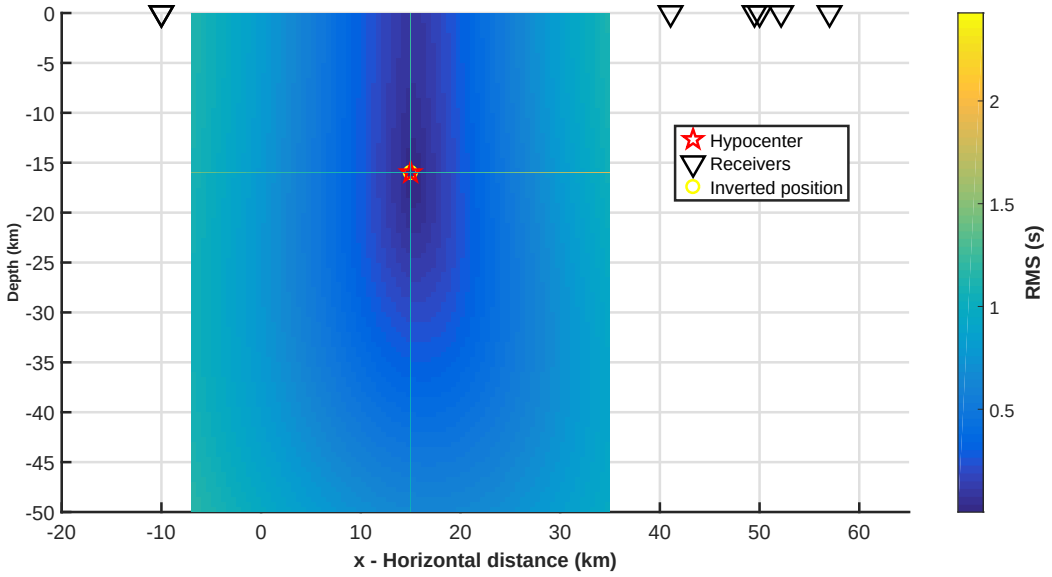

Figure 5.13: Synthetic test for the single S-P difference grid search method using the distributed station network. The earthquake occurs inside the network of stations. Plot of the X-Z plane. Both P-waves and S-waves are used.

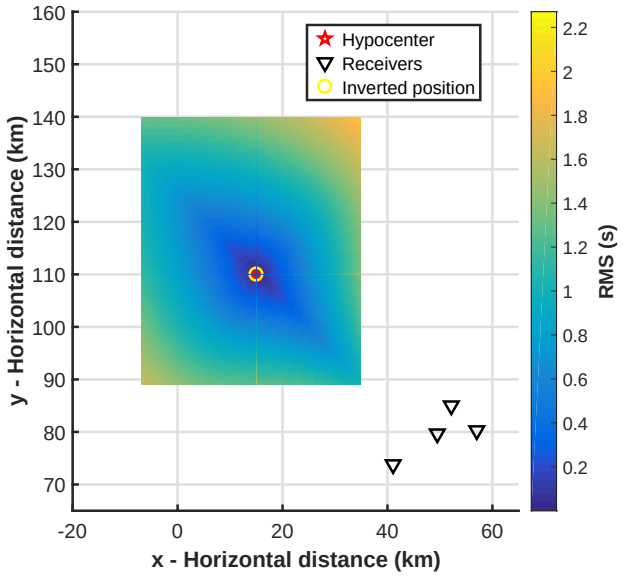

Figure 5.14: Synthetic test for the single-difference method using the Jan Mayen network. The earthquake occurs outside the network of stations. Plot of the Horizontal plane.

5.3.4 Combination of Single P-P Difference and Single S-P Difference: Synthetic Test

The idea behind combining the single P-P difference and the single S-P difference grid search comes from combining the beam-like structure with good direction sensitivity for P-P, seen in Figure 5.6, with the elongated contour with good distance sensitivity for S-P, seen in Figure 5.11. By combining these methods, a more constrained contour is obtained, and in principle, more accurate earthquake locations are found.

Figures 5.14 and 5.15 show the resulting contour plots of the single-difference method for an event outside the seismic network. The shape of the low-value area in the horizontal plane is an elongated ellipse (Figure 5.14). The depth resolution shows a narrow dip structure (Figure 5.15). This suggests a good constraint in the horizontal directions.

For an event occurring inside the station network, the contour plot is similar to the ones seen above. A circular low value zone is observed (Figure 5.16), as well as a depth resolution similar to the one for the traditional method (Figure 5.17). This suggests that the horizontal coordinates for this geometry are also well constrained.

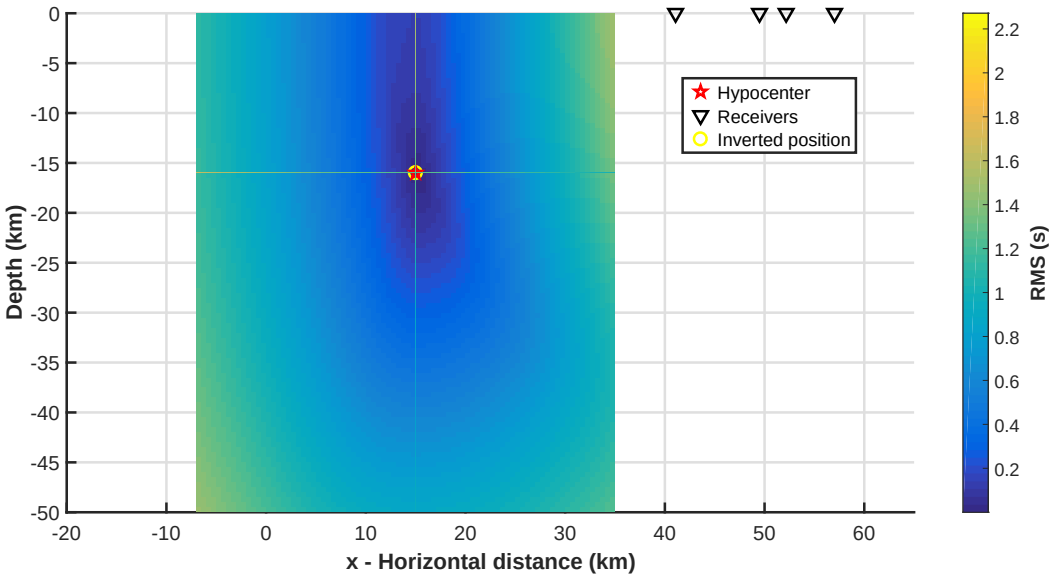

Figure 5.15: Synthetic test for the single-difference method using the Jan Mayen network. The earthquake occurs outside the network of stations. Plot of the X-Z plane.

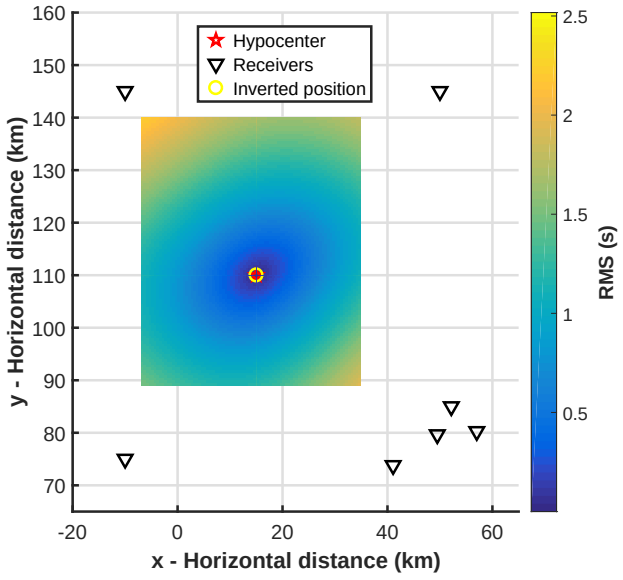

Figure 5.16: Synthetic test for the single-difference grid search method using the distributed station network. The earthquake occurs inside the network of stations. Plot of the horizontal plane.

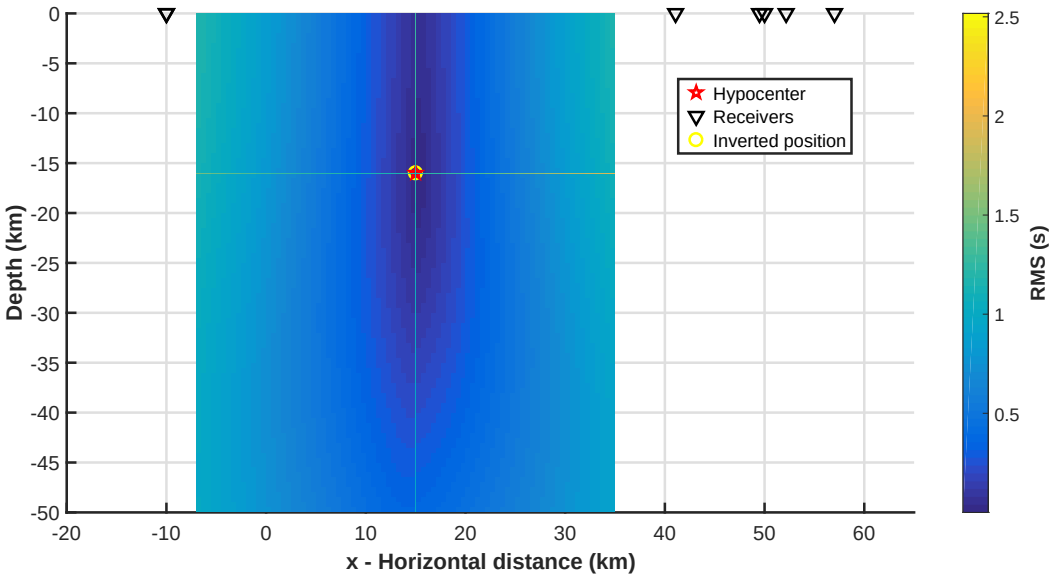

Figure 5.17: Synthetic test for the single-difference grid search method using the distributed station network. The earthquake occurs inside the network of stations. Plot of the X-Z plane.

Chapter 6

Relocation of Seismic Events near Heimaey and Jan Mayen

6.1 Overview

In this chapter, the relocation results for the data-sets from Heimaey and Jan Mayen are presented. Section 6.2 discusses the relocation for the Heimaey data-set. The section first discusses the waveforms and the selected arrival times. Then, relocations using the linearized inversion in SEISAN, the traditional, and the single-difference grid search methods are presented. The final Section, 6.3, presents the waveforms and arrival times for the Jan Mayen data-set. Then the relocation results, using the various relocation methods, are discusses as well as an uncertainty analysis.

6.2 Heimaey Relocations

6.2.1 Waveforms and Phase Picks

Selecting accurate arrival times for P- and S-waves is an essential step in processing seismic waveform data, as they are required to determine the earthquake locations. Figures 6.1 and 6.2 show how P- and S-wave arrivals have been picked for the 24 April 2018 event. The P- and S-arrivals are selected where the waveforms show a sudden increase in amplitude.

These are denoted by the black vertical lines labeled IP and ES.

6.2.2 Relocation

Unfortunately, after almost two years of data collection on Heimaey, only two events in the vicinity of the island were relevant for further analysis. These events are relocated using the linearized inversion in SEISAN, the traditional grid search method, and the single-difference grid search method (see Section 5.2).

The grid search methods were done using two steps. First a coarse grid search, with a $(1, 1, 1)$ km grid increment, is executed to find the approximate locations of the events. Then, a grid search zoomed in around the approximate location is computed, with a grid increment of $(0.1, 0.1, 0.1)$ km. The final hypocenter location is found at the point where the misfit has its global minimum. It is worth noting that the January event had only three available stations, whereas the April event had four.

The relocations are plotted together with IMO's location of the events. It should be noted that IMO located these events with their entire station network. This includes stations on Heimaey (see figure 3.1a) as well as on the mainland.

Results using the Traditional Grid Search method

Figures 6.3 and 6.4 show the relocation results after applying the traditional grid search method to the data. The figures also show the location uncertainty for the coarse grid searches and the IMO locations. The April event's final location is 63.425°N, 20.714°W, and at a depth of 11.5 km (Figure 6.3). The contours show a significant uncertainty for the event, which is most likely due to the aperture of these stations as they all are located on the same island. The final location for the January event is 63.556°N, 20.684°W, at a depth of 12.5 km (green circle in Figure 6.4), similarly with significant uncertainty as shown in the contour plots. The stations for the January event lie on a line, and the event is relocated along this line.

The earthquakes are relocated by the grid search methods 8 km North-West and 30 km North relative to the IMO locations. Moreover, the location found by HYPOCENTER in SEISAN for the January event converges to a location between the grid search and IMO

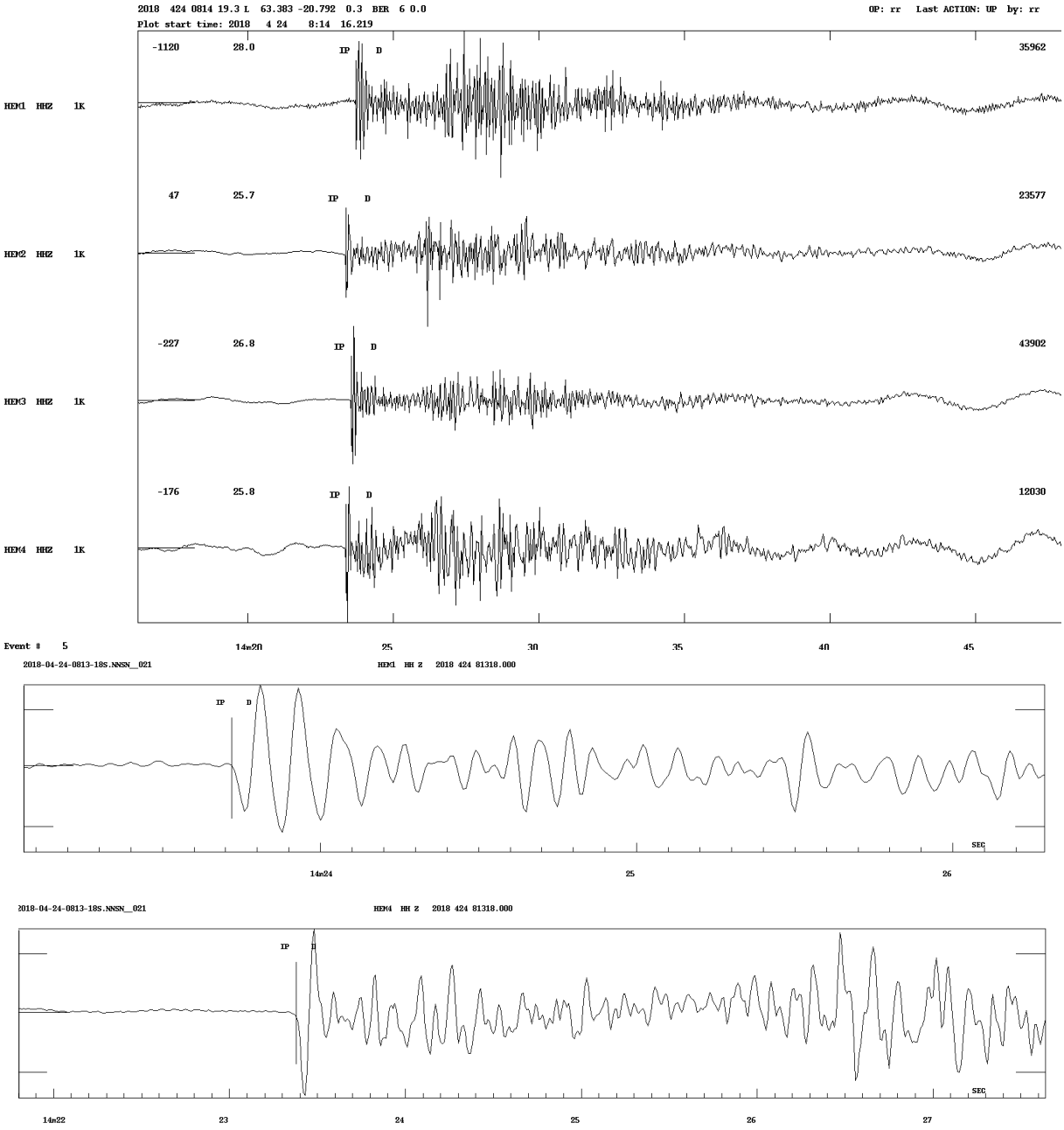

Figure 6.1: P-picks on waveforms for the earthquake that occurred on the 24th of April 2018. The black vertical lines labeled IP denote the P-wave selection. The picks were chosen on the vertical component. The top figure provides an overview of the traces. The bottom two traces are zoomed in on the P-phases picked on HEM1 and HEM4.

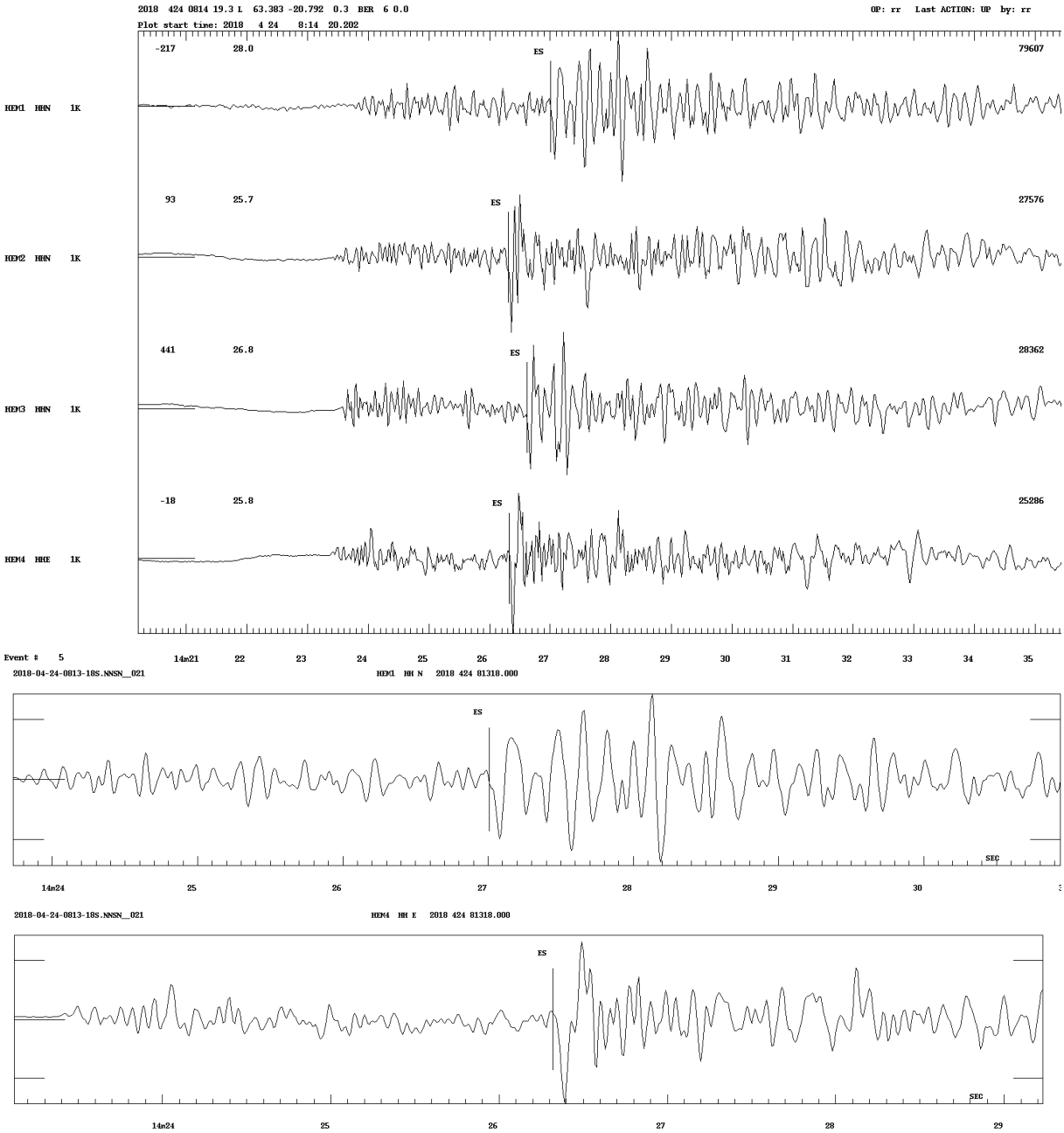

Figure 6.2: S-picks on waveforms for the earthquake that occurred on the 24th of April 2018. The black vertical lines labeled *ES* denotes the S-wave selection. The picks were chosen on the North component for HEM1, HEM2, and HEM3, and the east component for HEM4. The top figure provides an overview of the traces. The bottom two traces are zoomed in on the S-phases picked on HEM1 and HEM4, respectively.

solutions. However, the HYPOCENTER location is close to the high probability region shown by the grid search. The spread in the locations and the contour plot suggest an uncertain location for the event.

Results using the Single-Difference Grid Search method

Figures 6.5 and 6.6 show the relocation results using the single-difference grid search method. The final location for the April event is 63.394° N, 20.720°W, at a depth of 11.5 km (Figure 6.5). The coordinates of the January event are 63.483°N, 20.653°W, at a depth of 21.5 km (Figure 6.6). The contour map of the April event suggests that this event is well constrained. The January event, however, is less constrained. As in the case of the traditional method, the locations are relocated 8 km North-West and 20 km North, respectively, relative to the IMO locations.

The January event is located in a similar position as for the traditional grid search method. HYPOCENTER in SEISAN locates the event between the location found by IMO and the grid search. In contrast to the traditional grid search, the contour plots do not show a high probability near the HYPOCENTER location. This is most likely because of the stations aperture, where the three stations that recorded the event are more or less located along a line.

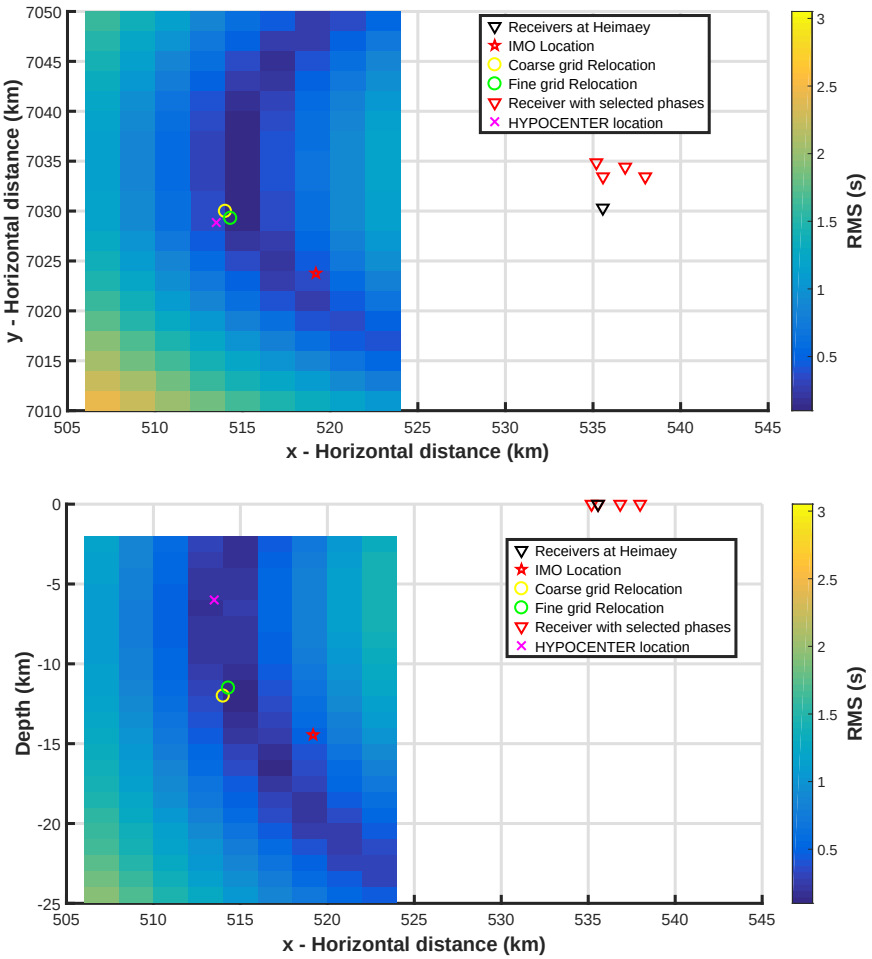

Figure 6.3: Relocation of the earthquake that occurred on April 24 of 2018 at 08:24:19. The misfit plots for the coarse grid search using the traditional grid search are shown. The final location after using the fine grid search is 63.425°N, 20.714°W, at 11.5 km depth. Figure (a) shows the horizontal plane of the coarse grid search. Figure (b) shows the X-Z plane of the coarse grid search. The label shows the receivers as black triangles (receivers with selected phases are red), the IMO location as the red star, the coarse grid search relocation as the yellow circle, the fine grid search relocation as the green circle and the magenta cross represents the HYPOCENTER relocation found in SEISAN.

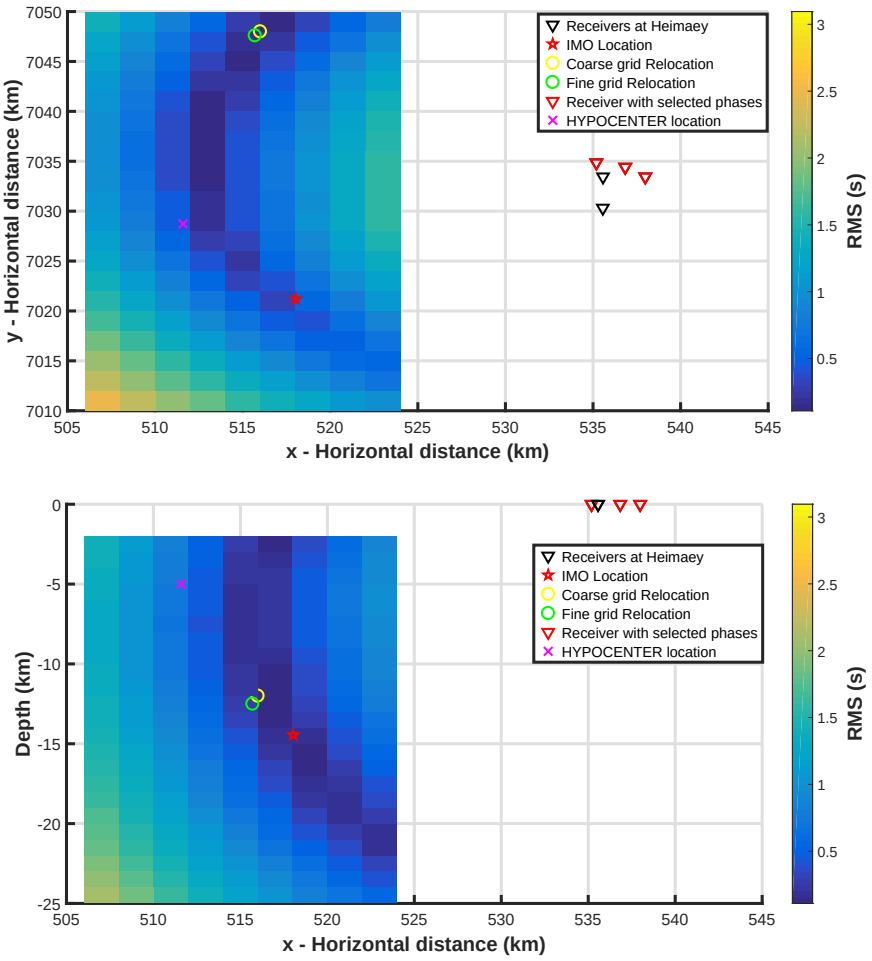

Figure 6.4: Relocation of the earthquake that occurred on January 31 of 2019 at 01:42:05. The misfit plots for the coarse grid search using the traditional grid search are shown. The final location applying the fine grid search is at 63.556°N, 20.684°W at a depth of 12.5 km (green circle). Figure (a) shows the horizontal plane of the coarse grid search. Figure (b) shows the X-Z plane of the coarse grid search. The label shows the receivers as black triangles (receivers with selected phases are red), the IMO location as the red star, the coarse grid search relocation as the yellow circle, the fine grid search relocation as the green circle and the magenta cross represents the HYPOCENTER relocation found in SEISAN.

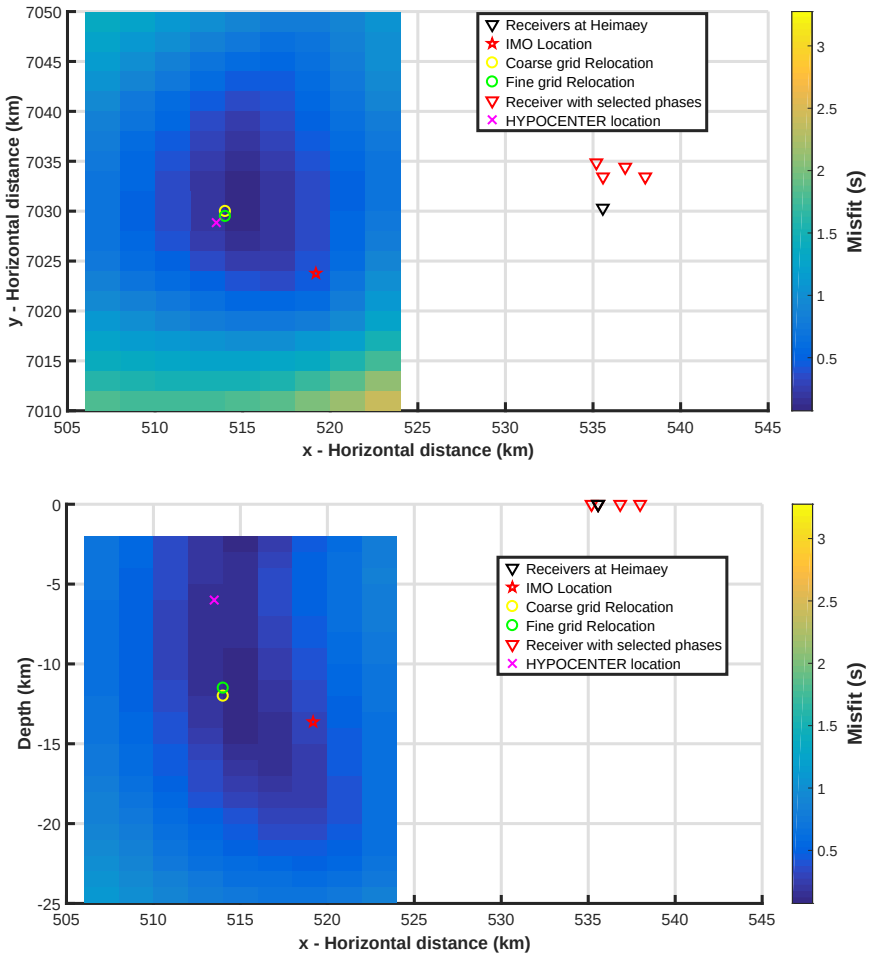

Figure 6.5: Relocation of the earthquake that occurred on April 24 of 2018 at 08:24:19. The misfit plots for the coarse grid search applying the single-difference method are shown. The final location after applying the fine grid search is 63.394°N, 20.720°W at a depth of 11.5 km (green circle). Figure (a) shows the horizontal plane of the coarse grid search. Figure (b) shows the X-Z plane of the coarse grid search. The label shows the receivers as black triangles (receivers with selected phases are red), the IMO location as the red star, the coarse grid search relocation as the yellow circle, the fine grid search relocation as the green circle and the magenta cross represents the HYPOCENTER relocation found in SEISAN.

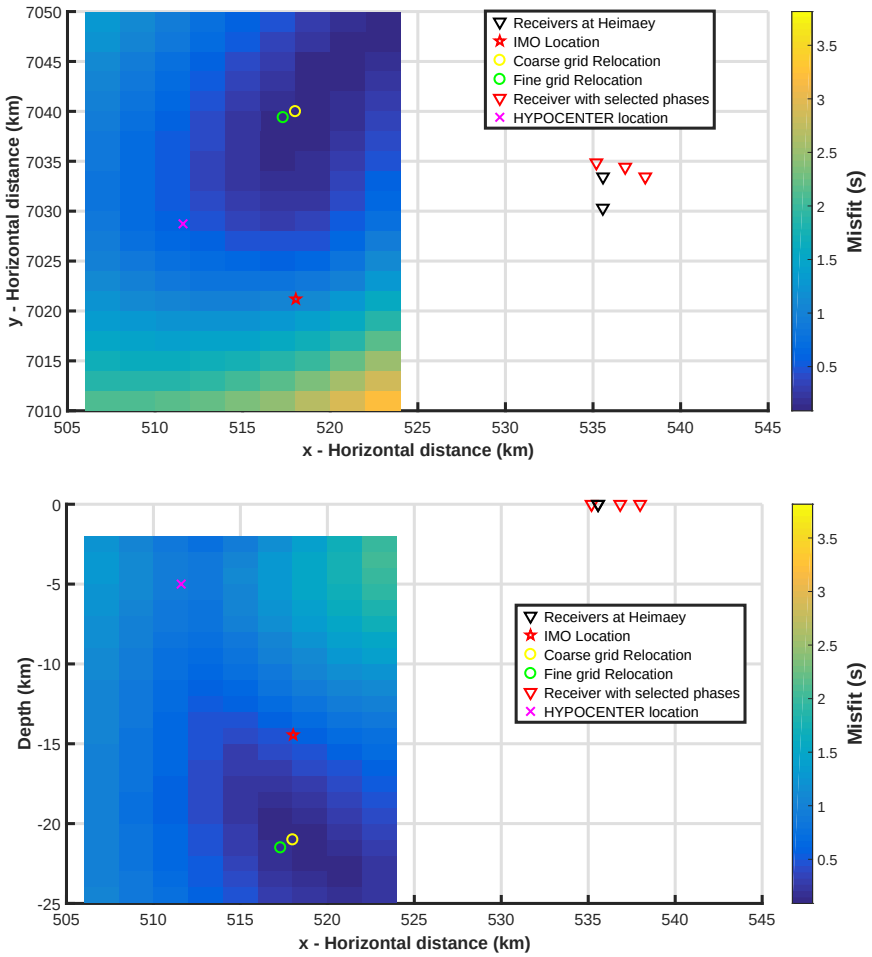

Figure 6.6: Relocation of the earthquake that occurred on January 31 of 2019 at 01:42:05. The misfit plots for the coarse grid search applying the single-difference method are shown. The final location after executing the fine grid search is 63.483°N, 20.653°W at a depth of 21.5 km (green circle). Figure (a) shows the horizontal plane of the coarse grid search. Figure (b) shows the X-Z plane of the coarse grid search. The label shows the receivers as black triangles (receivers with selected phases are red), the IMO location as the red star, the coarse grid search relocation as the yellow circle, the fine grid search relocation as the green circle and the magenta cross represents the HYPOCENTER relocation found in SEISAN.

6.3 Jan Mayen Relocations

This section presents the results from the relocation of the 262 event in the Jan Mayen data-set. It starts by looking at the waveforms in the data-set. Then, it discusses the relocations using the traditional grid search method and the single-difference grid search method. After this, a swarm to the North-West of the Jan Mayen island is relocated using the 3D velocity model introduced in Subsection 4.3.2.

6.3.1 Waveforms and Phase Picks

On November 9 there was a magnitude 6.7 event 130 km north-west of Jan Mayen. A large number of aftershocks followed this event. In total 262 aftershocks, recorded by the NNSN between November 2018 and May 2019, have been analyzed. Nearly 940 P-waves and S-waves have been selected at the four stations on the island. Analysts from UoB initially selected the P- and S-arrival times for the events. However, some picks have been revised to improve their quality. In total, around 20-30 picks were revised.

In contrast to the Heimaey data-set, where all stations show high-quality arrivals for the events, some of the waveforms in the Jan Mayen data-set are of low-quality. Figure 6.7 illustrates the difference between seismograms with clear and unclear picks.

6.3.2 Relocation

This sub-section presents the relocations of the Jan Mayen data-set. First, the relocations using the traditional grid search method and the 1D velocity model for Jan Mayen are shown. Then, the relocations are repeated for the single-difference method. After this, an analysis of when the events occurred is given. Finally, the relocation methods are applied using the 3D velocity model presented in Subsection 4.3.2 for a swarm North-West relative to the Jan Mayen island. This is compared to relocations of the same swarm using the 1D Jan Mayen velocity model.

The relocation of the entire Jan Mayen data-set is done using two grid search steps, with decreasing grid increments. First, the arrival times for the entire survey area are calculated with a coarse grid increment (5,5,2) km. As will be shown in the next subsections, the

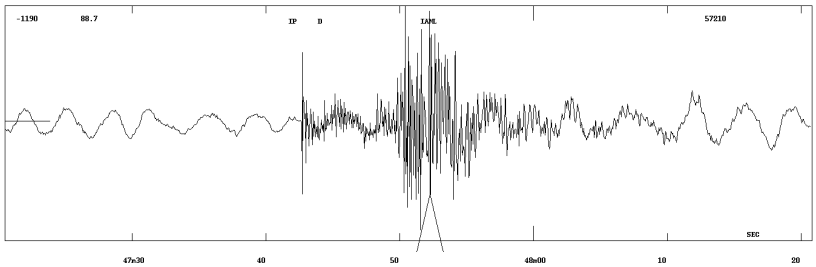

(a) Z-component at station JMI, raw waveform.

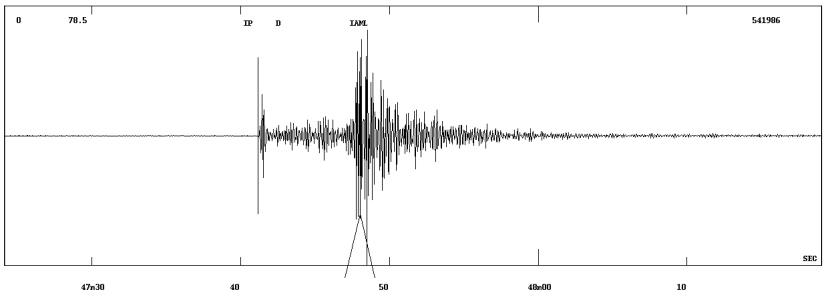

(b) Z-component at station JMI, filtered 5 to 10 Hz.

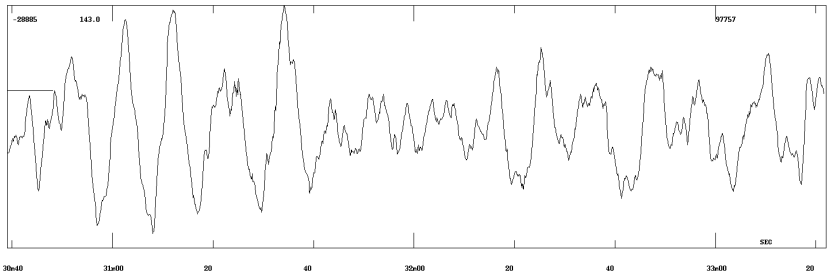

(c) Z-component at station JMI, raw waveform.

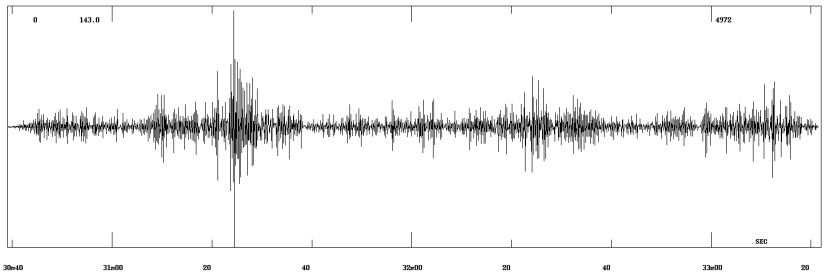

(d) Z-component at station JMI, filtered 5 to 10 Hz.

Figure 6.7: Figure (a) and (b) display an example of selected P-arrivals at a station with a high signal-to-noise ratio for the magnitude 3.3 event which occurred on November 8, 2018 at 13:47. Figure (c) and (d) show an example of data where it is difficult to select the P-arrival. This data comes from a magnitude 3.3 event which occurred on November 9, 2018 at 02:30.

depth resolution for the events is low. Because of this, the depths are fixed to 16 km. A new fine grid search with an increment of (0.1,0.1) km is then used.

Catalog locations

The initial locations found by analysts at UoB using the HYPOCENTER program in SEISAN show one clear swarm 10-40 km north-east of Jan Mayen (see Figure 2.7 and Table 9.1). Three other less clear swarms are also present in the area. The first and most spread out swarm is located approximately 50-130 km to the north-west, near the main event. This swarm is spread along an NNE-SSW line. The second swarm is spread along the fracture zone north of the island. The events in this swarm are found along an NW-SE line parallel to the fracture zone. The third swarm is centered 50-100 km east of the island. This swarm is also spread along a NNE-SSW line as the swarm to the north-west.

From to the bathymetry maps (see Figures 2.6 and 2.7), it is clear that these earthquakes correlate with the Jan Mayen transform fault. The earthquake location becomes more uncertain with distance. This is seen in the swarms to the north-west and the east. Here the locations are more spread out than the locations of the swarms closer to the seismic stations. In addition, several outliers are located to the south of Jan Mayen.

Relocation using the Traditional Grid Search method

The traditional grid search method and the local 1D velocity model have been used for the relocation of the catalog data presented in the section above. Results from the coarse grid search show that the depth resolution of the events is low (see Figures 6.8 and 6.9). No clear trend can be extracted from the depth plot as most events are relocated below the Moho at 40 km (Havskov and Atakan, 1991). On the basis of this the depth of the events was fixed to 16 km for the final grid search. The epicenter location shown in Figure 6.10 are obtained from this fine grid search (see Table 9.1 for the relocations in geographical coordinates).

Figure 6.10b shows how the traditional grid search method relocates the catalog events. The location method locates the events into six swarms. The clearest swarm is observed

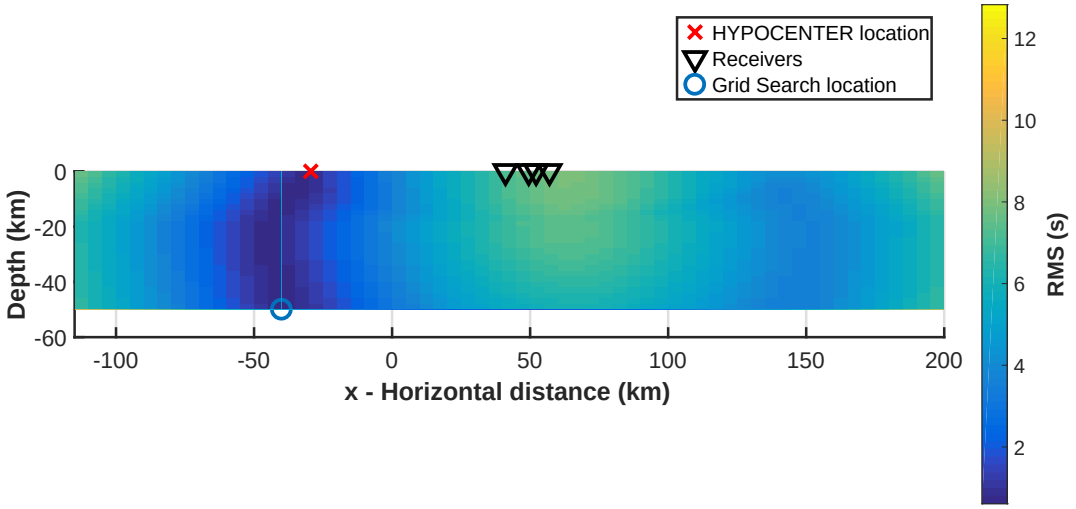

Figure 6.8: Contour plot of the misfit function for a magnitude 2.5 event which occurred on November 09, 2018 at 02:26:27. The contour plot illustrates the low depth resolution for an event west of Jan Mayen. The black triangles indicate the receivers, the blue circles denotes the location of the event after relocation and the red cross denotes the catalog location.

north-west of Jan Mayen (this is swarm number 2 (red)). This swarm is relocated some km towards the north compared to the catalog locations. The events also seem to be more concentrated than the catalog locations. Three smaller swarms are seen north and north-west of Jan Mayen (swarm 3 (green), swarm 4 (blue), and swarm 5 (gray)). These are not as clear in the catalog data, where the events are spread out between the swarms. Two other swarms are observed 50-130 km north-west of Jan Mayen (swarm 1 (black)), and 50-150 km east (swarm 6 (yellow)). The earthquakes in these swarms are quite spread out. Both swarms are on average relocated 15 and 20 km north of the catalog locations.

Some outliers from the catalog locations located south of Jan Mayen are relocated to swarm number 2 (see Figure 6.10b). Figures 6.11 and 9.8 show two of the events relocated from the south to the north. Note that less important figures are shown in Chapter 9, the Appendix. Figure 6.11 shows two local minima for the earthquake locations. The catalog location is found in the local minimum to the south of Jan Mayen. The relocation shows the event to be in the global minimum north-west of Jan Mayen, and on the fracture zone. The second figure suggests another reason for the difference in the location (see

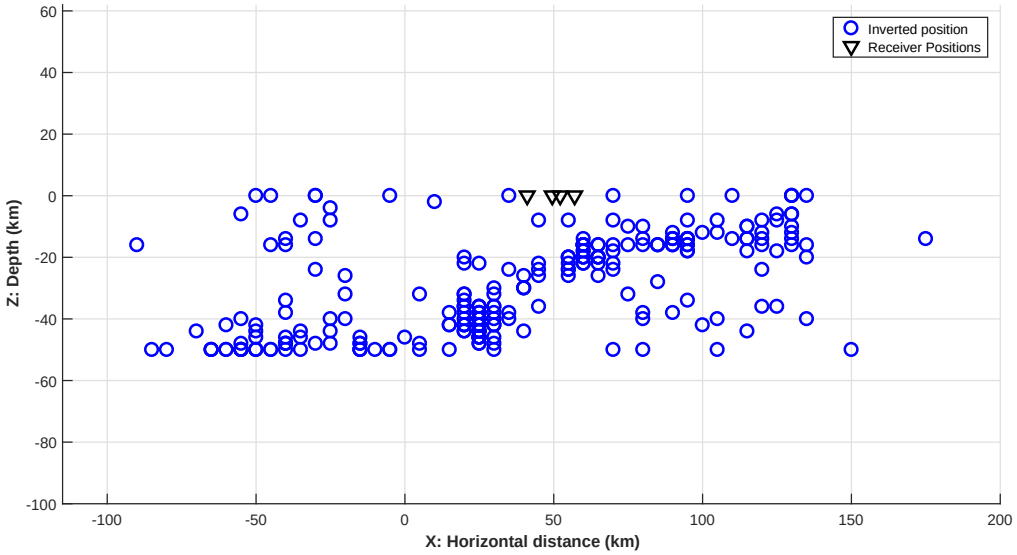

Figure 6.9: Depth plot of the relocated events using the traditional grid search method. The coarse gird search is applied to find the depth. An increment of of (5,5,2)km was used.

Figure 9.8). It shows a location with a very high uncertainty that stretches around Jan Mayen and includes the catalog location. Other events are relocated, but remains south of the island (e.g. see Figure 9.9) In total seven events are relocated north-west of the Jan Mayen. All relocations seem to occur because of uncertainties in the locations. From the results presented above, the traditional grid search method seems to improve the location of the events.

Outlier Analysis for the Traditional Grid Search Method

Figure 6.10 shows that outliers are seen throughout the survey area. Figure 6.10a shows a plot of the relocated events color-coded by the number of available phases. The magenta and blue circles in the figures denote events with less than three P-phases and three P-phases, respectively. These events represent the majority of the outliers. For the S-picks shown in Figure 6.12, there is no clear correlation between the number of phases selected and the outliers. From the figures, it is observed that the grid search relocations with four selected phases yield a location that is a lot better constrained and has fewer outliers than the events with three or less chosen phases.

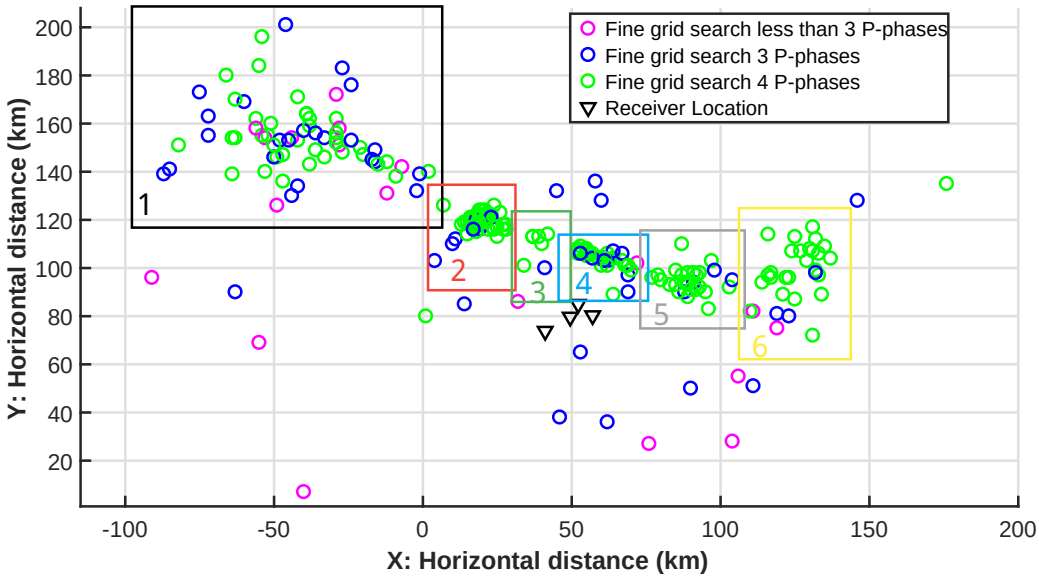

(a) Relocation of the Jan Mayen events using the traditional method.

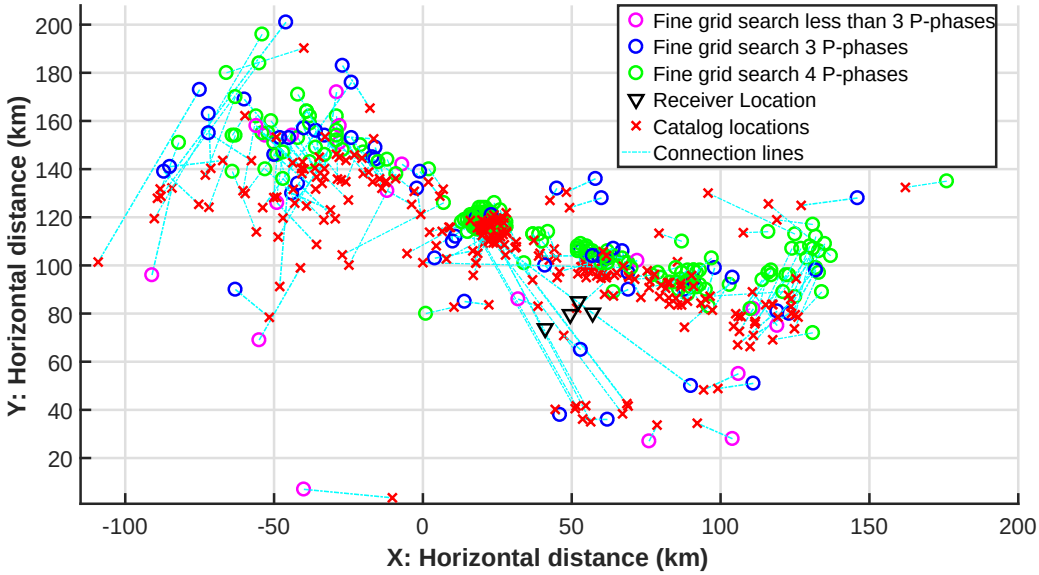

(b) Relocated and catalog events plotted together and connected by the cyan dashed lines.

Figure 6.10: Relocation results for the fine grid search using the traditional grid search method. Figure (a) shows the relocated events near Jan Mayen. Figure (b) shows the relocated and the catalog location plotted together and connected by the cyan dashed line. In both figures the locations have been divided into three groups depending on the number of selected phases. The green circles indicate four selected P-phases. The blue circles three and the magenta circles less than three phases. See table 9.1 for the relocation in geographical coordinates.

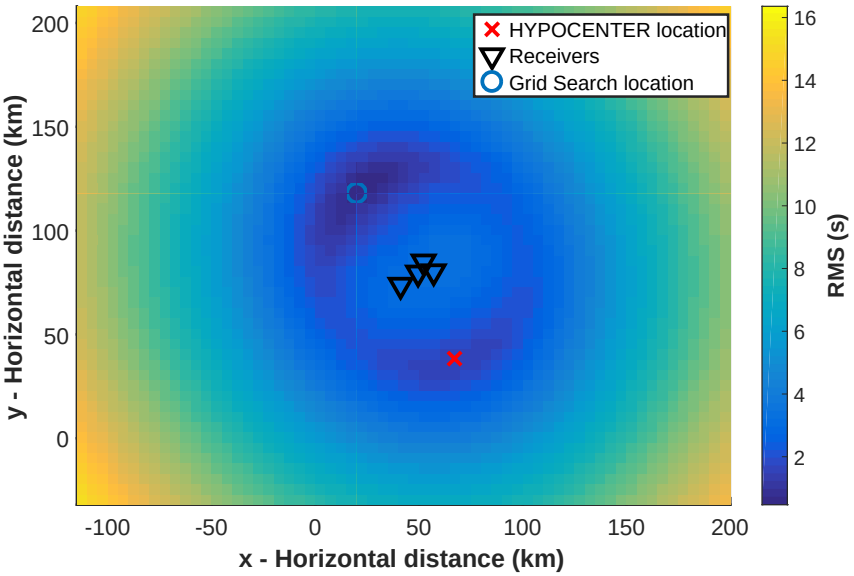

Figure 6.11: Contour plot of the misfit function of a magnitude 2.0 event which occurred on November 13, 2018 at 10:22:18. The figure show two local minima. The catalog location is located near the local minima to the south. The grid search relocates the event to the position in the north-west where the misfit function obtains its global minimum.

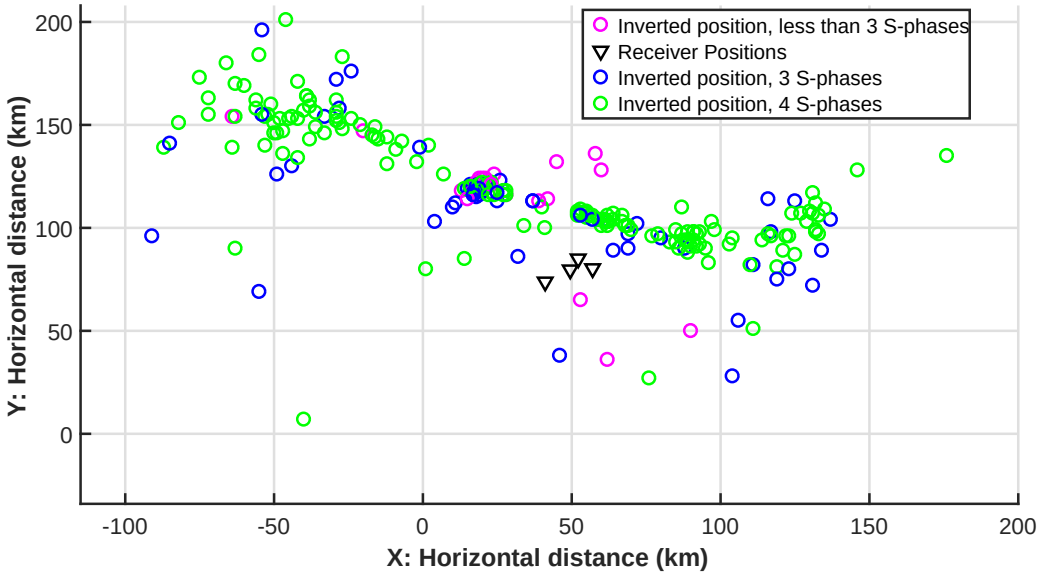

Figure 6.12: The locations in the figure have been divided into three groups depending on the number of selected S-phases. The green circles indicate that four phases have been selected. The blue circles three phases and the magenta circles less than three phases.

Figures 9.10a and 9.10b from the Appendix show the misfit contour for two of the outliers. These two events each have two available P-phases. The November 9 event has three S-picks, and the January 1 has four. The contour plot for the November event shows low direction sensitivity. For the January event, the misfit contours suggest that the event is correctly located south-west of the island. However, the location is also largely insensitive to direction.

Relocation using the Single-Difference method

The single-difference grid search method and the local 1D velocity model have been used to relocate the events (see Table 9.1 for the relocations in geographical coordinates). The relocations were executed using a coarse grid search than a fine grid search, as for the traditional grid search method (see Figure 6.13a). This resulted in the same trend in depth resolution (see Figure 9.11), which is why the depths were fixed to 16 km.

Figure 6.13a shows how the single-difference grid search method relocates the catalog events. The method relocates the events into six swarms, which are similar to the ones found using the traditional grid search method. The clearest swarm is observed north-east of Jan Mayen (swarm 2), similarly to the catalog location. This swarm is relocated some kilometers further north than the catalog location, and the events seem to be more concentrated than the catalog locations. Three smaller swarms are observed north (swarm 3 and 4) and north-west (swarm 5) of Jan Mayen. These are not as clear in the catalog data, because some events are located between the swarms. Two other swarms lie 50-130 km north-west of Jan Mayen (swarm 1), and 50-150 km west (swarm 6). The earthquakes in these swarms are quite spread out. Both are on average relocated 15 and 20 km north of the catalog locations.

As in the case of the traditional method the events located south of Jan Mayen are relocated to swarm 2 north-west of the island (see Figures 9.12a and 9.12b for illustrations). The figures show a clear global minimum in swarm 2, and a local minimum where the catalog location is found. The main difference from the traditional method is that the contour plot for these two events show a much clearer global minimum in swarm 2.

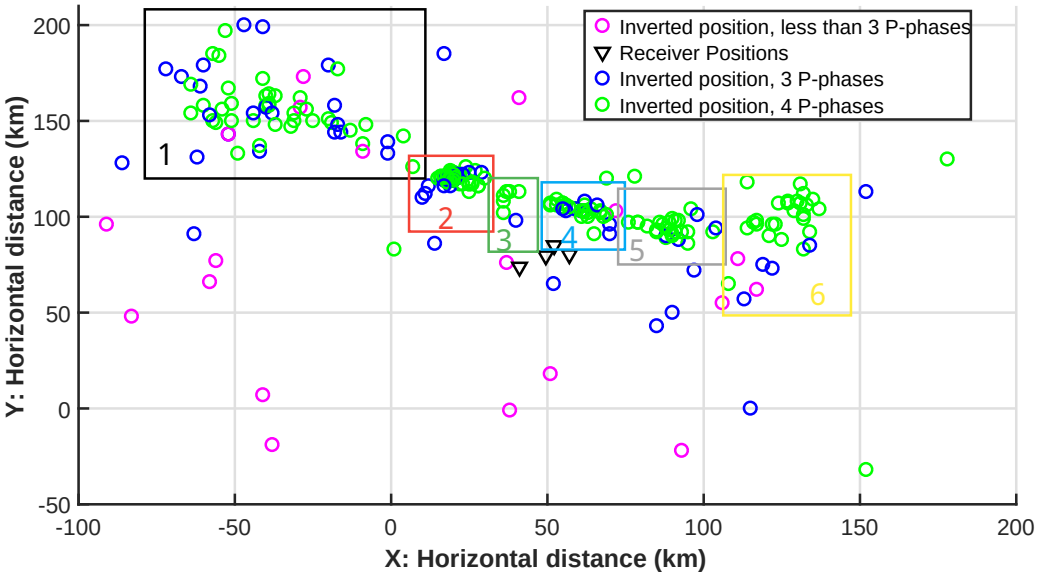

(a) Relocation of the Jan Mayen events using the single-differece method.

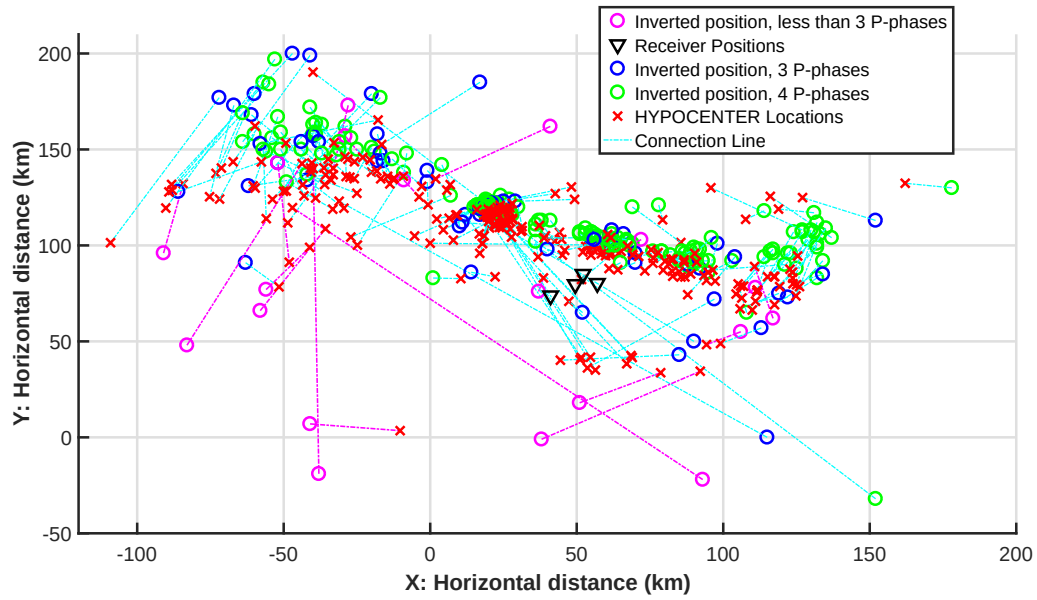

(b) Relocated and catalog events plotted together and connected by the cyan dashed lines.

Figure 6.13: Relocation results for the fine grid search using the single-difference grid search method. In both figures, the locations have been divided into three groups depending on the number of selected phases. The green circles indicate four selected P-phases. The blue circles three and the magenta circles less than three phases. The cyan lines in (b) connect the catalog location and its relocation, to better understand the change in the hypocenter.

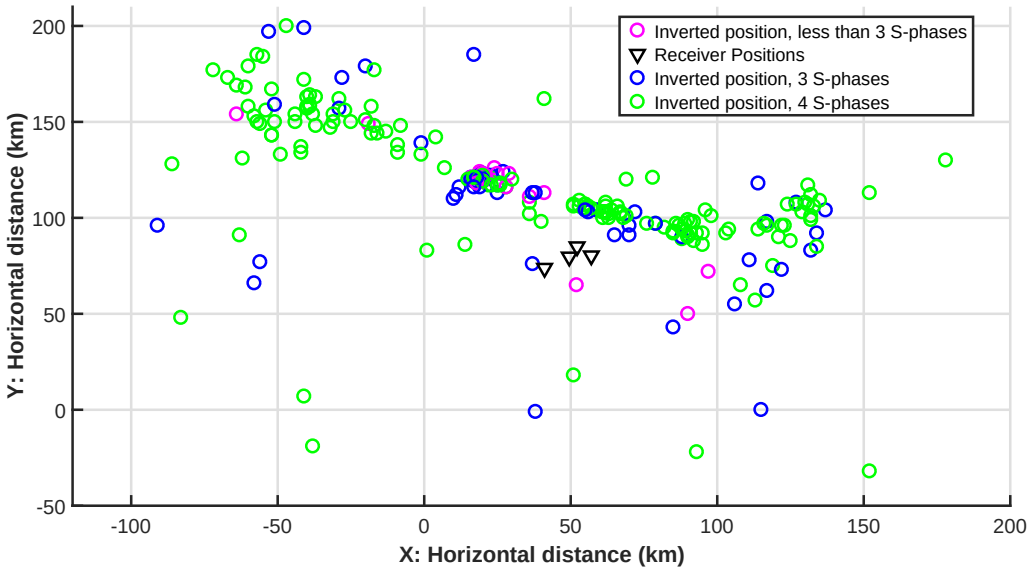

Figure 6.14: The earthquake locations in this figure have been divided into three groups depending on the number of selected S-phases. The green circles indicate that four phases have been selected. The blue circles three phases and the magenta circles less than three phases.

Outlier Analysis for the Single-Difference method

The single-difference grid search contains a similar number of outliers as the traditional method. Figures 6.13a and 6.14 show the events color-coded by the number of available P-phases and S-phases. The events with less than three phases represent the majority of the outliers (indicated by the magenta circles). Figure 6.14 suggests that the locations are more affected by the number of P-phases than the number of S-phases.

Figures 6.15 and 9.13 show two examples of events with fewer P-phase selections than S-phase selections. The first figure is an example of an event that originally was located in swarm 1, and relocated to the south-west by the single-difference method. The second figure is an example of the opposite. In this case, the original event was located outside the swarm 1. Both events have two selected P-picks and four S-picks. Figure 6.15a shows the single P-P difference locating the event 120 km south-west of Jan Mayen. The single S-P difference, on the other hand locates the event near the catalog event north-west of Jan Mayen. However, the uncertainty in the location for S-P stretches around Jan Mayen to the single P-P difference location (see Figure 6.15b). The combined location,

therefore, locates the event to the south-west (see Figure 6.15c). The second examples show another trend in the data (see Figure 9.13). The single P-P difference finds two possible directions the events can be located in, to the north-west and the south-east. The plot shows that the S-P method can not further constrain the event. Combining the two methods, however, finds two minima where the event can be located. One to the south-east and one to the north-west. This phenomenon might explain why some events with a low number of phase picks can be relocated over long distances. All the results above suggest that a low number of phases significantly reduces the accuracy of the location procedure, and when there are less than three P-phases, the location becomes unreliable.

6.3.3 Residual Analysis

To better understand the earthquake locations, it is useful to look at the residuals of the events. Figures 6.16 shows the events with residuals less than 0.5 sec and 0.2 sec. Figures 6.16a and 6.16c show the events with residuals less than 0.5 sec for the traditional grid search method and the single-difference method, respectively. Figure 6.16b shows the events with a residual less than 0.2 sec for the traditional grid search method. The figures show that the majority of the events with relatively high residual values are located near the fracture zone. The outliers are still present with relatively small residual values. This suggests that the 1D velocity model is not adequate for the relocation and that a 3D velocity model should be used. Another explanation for the relatively high residual levels is that the phase picks for the events are not of good quality. Most likely, there is a trade-off between the heterogeneity and the quality of the picks that creates these residual levels.

6.3.4 Occurrence of the events

Figures 6.17, 6.18, and 6.19 show the diurnal distribution of the relocated events from November 2018 to May 2019. The first figure shows the whole time period. The latter figures show events occurring in November and from December to May, respectively. Figure (a) shows the relocations using the traditional grid search method, whereas (b)

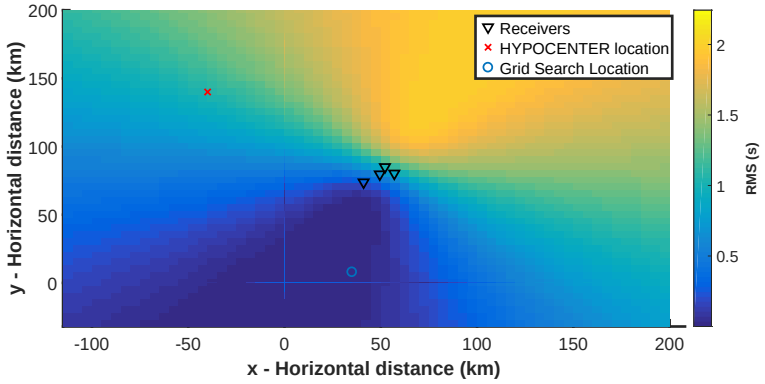

(a)

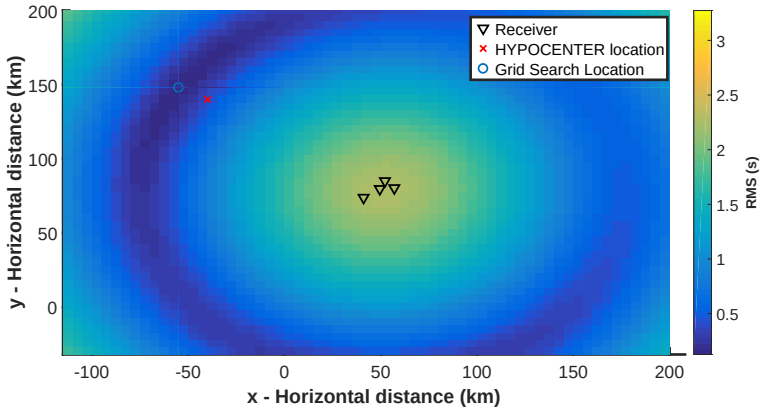

(b)

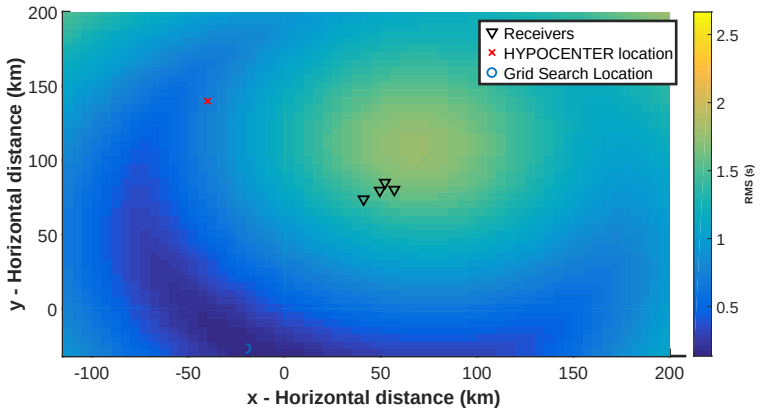

(c)

Figure 6.15: Example of an event relocated by the single-difference method. Figures (a), (b), and (c) show the contour plots for a magnitude 3.5 event which occurred on November 09, 2018 at 04:11:37. Figure (a) shows the contour map of the single P-P difference grid search. Figure (b) shows the contour map of the single S-P difference grid search. Figure (c) shows the combination of single P-P difference and single S-P differences above, resulting in the final contour maps.

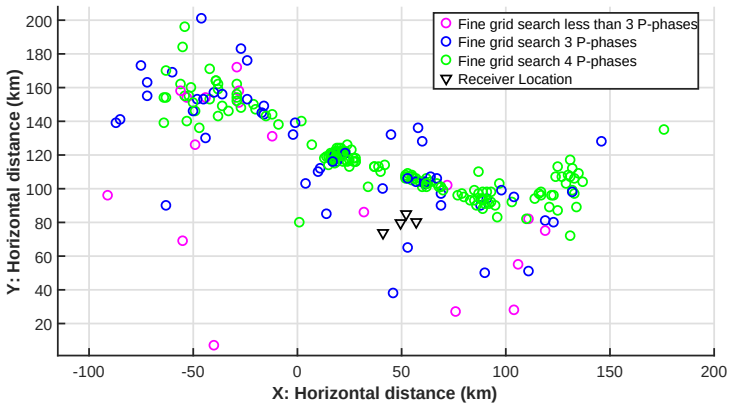

(a)

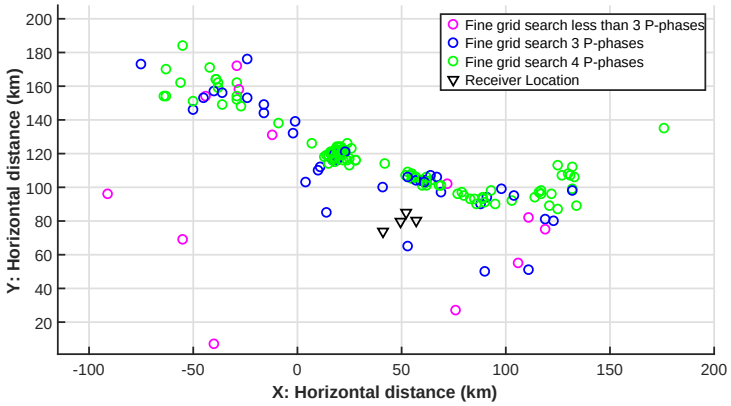

(b)

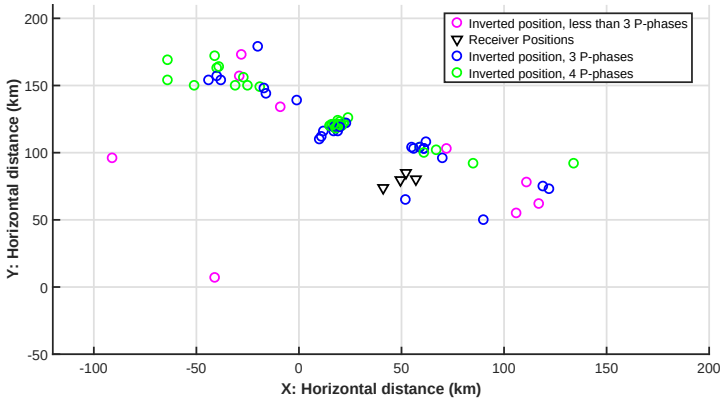

(c)

Figure 6.16: Events with an upper residual bound. Figure (a) shows all events with residual less than 0.5 sec located using the traditional method. Figure (b) shows all events with residual less than 0.2 sec using the traditional method. Figure (c) shows all events with residual less than 0.5 sec located using the single-difference method.

shows the relocations using the single-difference grid search method. Note that only the events with four selected P-phases have been selected for this analysis. These figures show a trend in the occurrence of the events. First, there is the main event. Events then propagate south-east and stop in swarm six west of Jan Mayen in May. Looking more closely at the individual months the primary propagation of the events seems to occur in November. This is especially clear in Figure 6.18, where the main event seems to trigger the swarm north-west of Jan Mayen as well as some events further east. Figure 6.19 shows that the activity starts to normalize in December. Moreover, regular activity from January to May is also observed, i.e., activity not directly caused by the big event in November.

6.4 Relocation using the 3D velocity model

The 3D velocity model introduced in Subsection 4.3.2 is used to relocate swarm 2 north-west of Jan Mayen. Both the traditional grid search method and the single-difference grid search method have been used for the relocations, and are compared to the catalog events. Figure 6.20 shows the relocations using the single-difference method, and Figure 9.14 show the relocations using the traditional grid search method. Most events in the swarm are relocated south-west relative to the catalog location. This is shown in Figures 6.20b and 9.14b for relocations using the single-difference and the traditional grid search method, respectively. Figure 6.20c and 9.14c show the locations found by the 3D velocity model relative to the locations found by the 1D velocity model using the single-difference method and the traditional method. The main trend seen from these figures is a 10 km shift in location to the south. These relocations are located away from the fracture zone. This is probably because of the low velocities near the surface for the 3D velocity model.

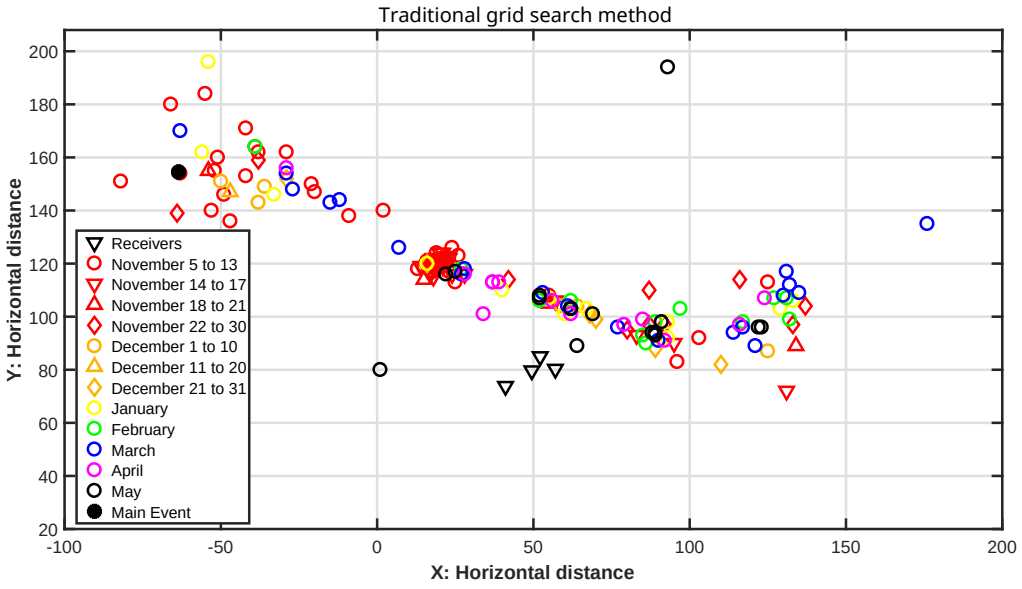

(a)

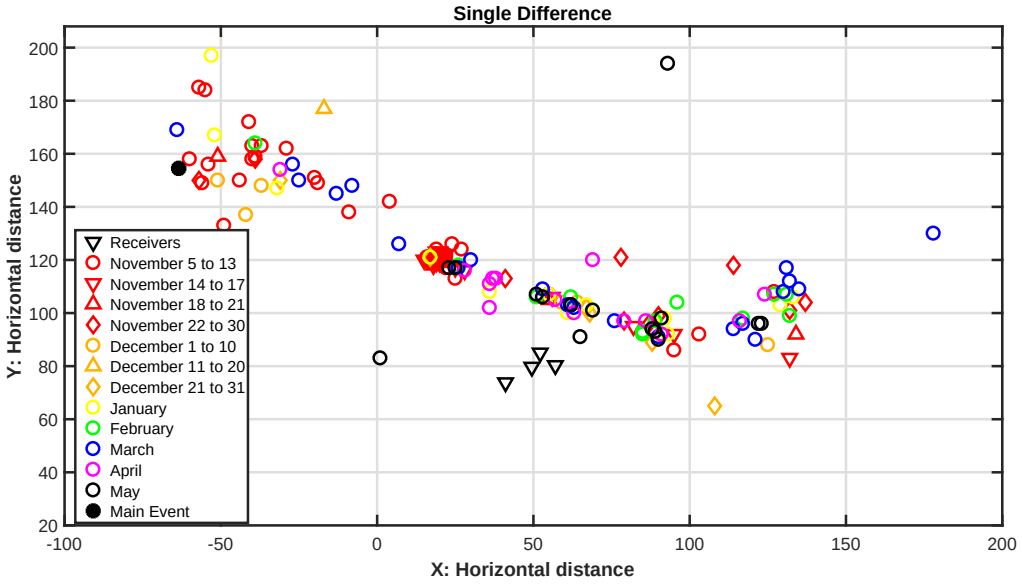

(b)

Figure 6.17: Events with four selected phases over the survey period are plotted and color-coded by the time of occurrence. Figure (a) is the relocation using the traditional grid search, and (b) the single-difference method. November events are red and divided into four time periods indicated by different symbols (circles, flipped triangles, regular triangles, and diamonds). December events are orange and divided into three groups (labeled by circles, regular triangles, and diamonds). January events are yellow, February green, March blue, April magenta, and May black. A black dot indicates the main event.

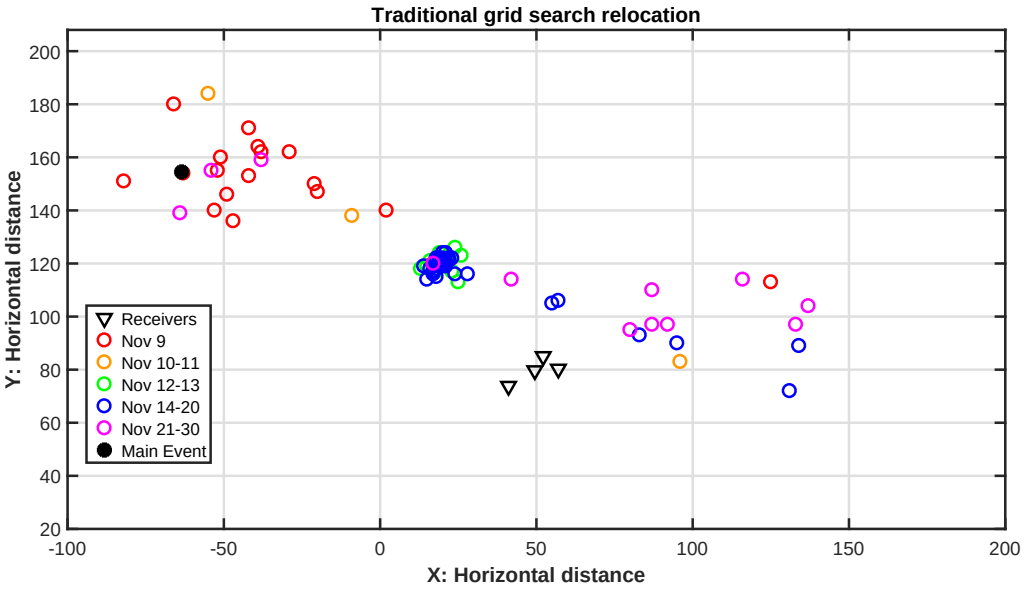

(a)

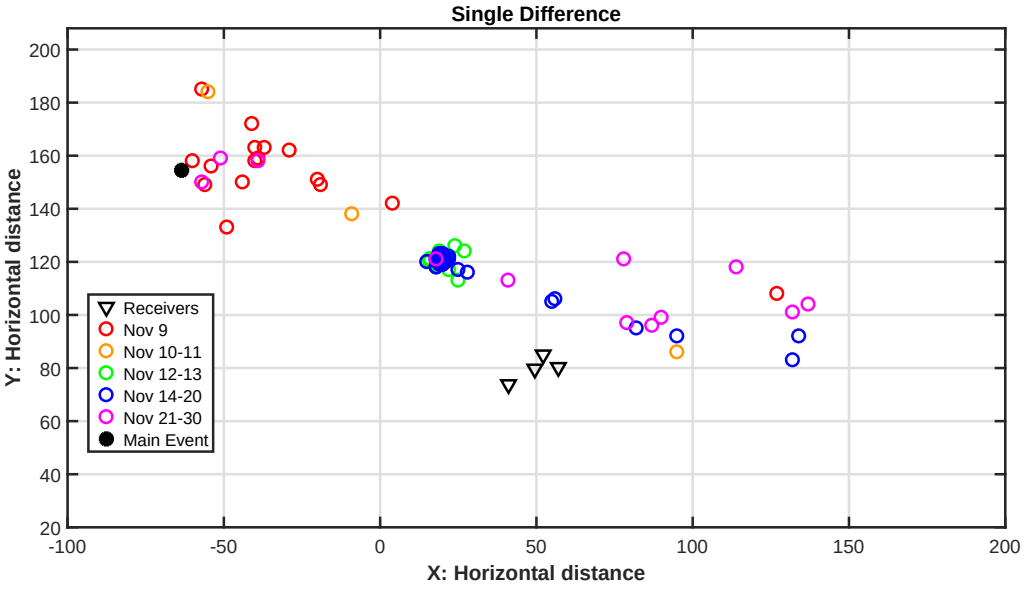

(b)

Figure 6.18: Events with four selected phases occurring in November after the main event November 9, 01:49:35 are plotted. Figure (a) shows the relocated events using the traditional grid search, and (b) the single-difference method. They are divided into five periods: November 9, November 10 and 11, November 12 and 13, November 14-20, and November 21-30 indicated by different colors (red, orange, green, blue, and magenta, respectively). A black dot indicates the main event.

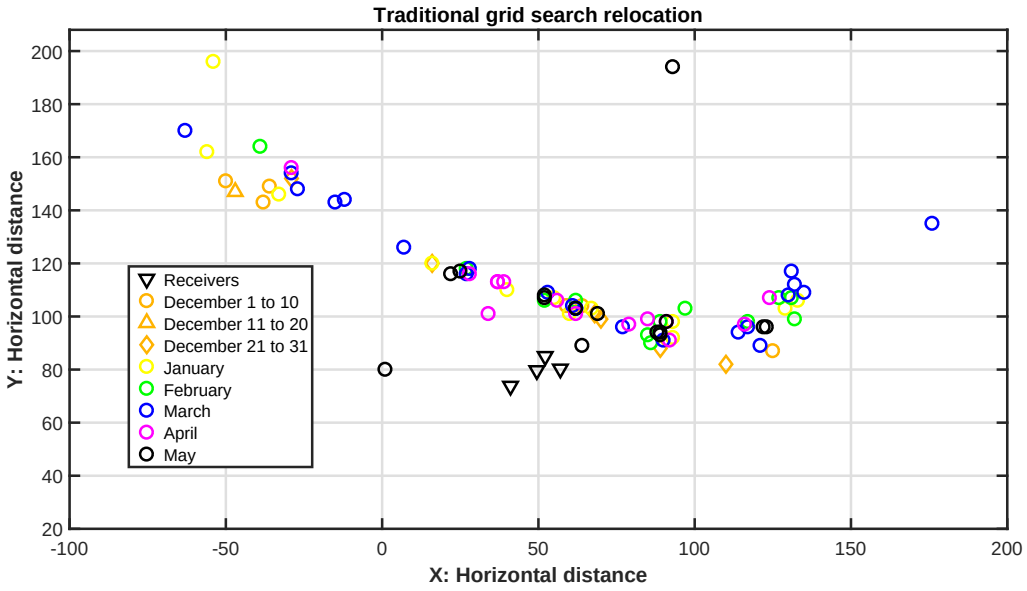

(a)

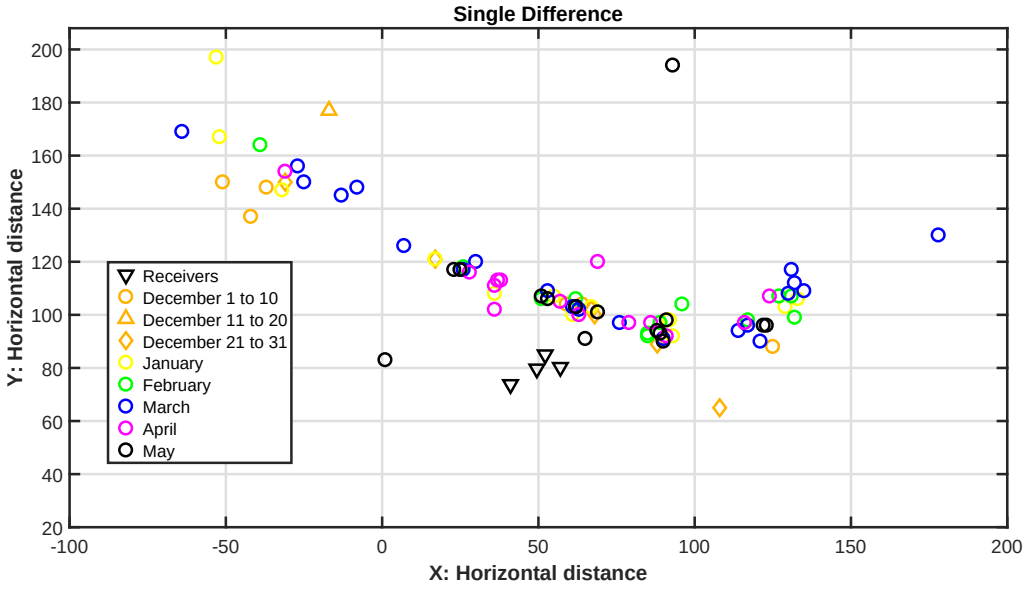

(b)

Figure 6.19: Events with four selected phases occurring from December to May. Figure (a) shows the relocations using the traditional grid search, and (b) the single-difference method. December events are orange and divided into three groups (labeled by circles, regular triangles, and diamonds). January events are yellow, February green, March blue, April magenta, and May black.

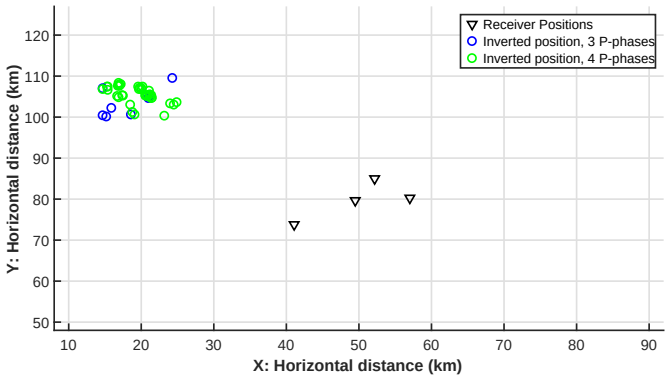

(a)

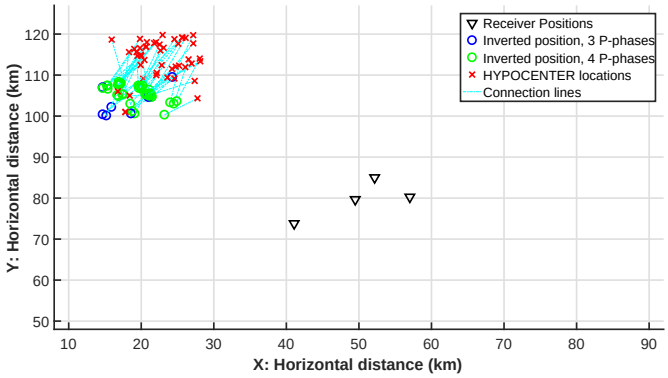

(b)

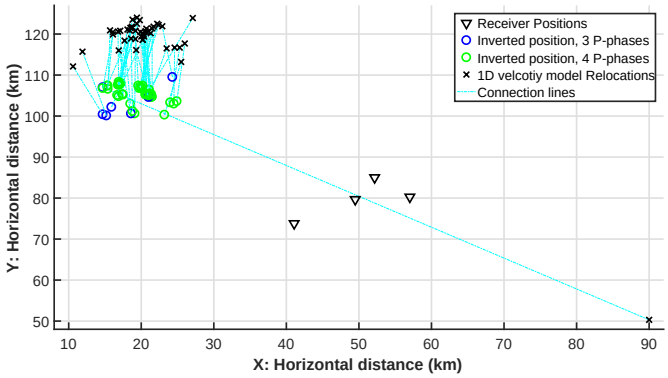

(c)

Figure 6.20: Relocation results using the 3D velocity model and the single-difference grid search method. Figure (a) shows the relocations using the 3D velocity model. Figure (b) shows the 3D velocity model relocations relative to the catalog locations. Figure (c) shows the 3D velocity model relocations relative to the 1D velocity model relocations. The labels denote events with four-selected P-arrivals with a green circle, three-selected P-arrivals with blue circles, the receivers as black triangles, red crosses as the catalog events, the black crosses as the 1D relocation positions, and the cyan dashed lines connect the relocated event with its corresponding catalog event.

Chapter 7

Discussion

7.1 Ray Tracing

In this thesis the theory and numerical implementation of a layered 1D, smooth 1D, and smooth 3D ray tracing algorithm have been described. These implementations resulted in various methods of estimating travel-times for earthquakes in the two survey areas of Heimaey and Jan Mayen. The different ray tracing procedures can be used as tools for travel times estimation and depend on the velocity model available. The ray tracing is done in two steps. First, travel times are computed using 1-point ray tracing. Secondly, travel times from a source to a receiver can be computed using 2-point ray tracing.

The three ray tracing implementations have some limitations. They contain different levels of complexities and have different computational costs. Therefore, the choice of time step in the ray tracing was important. When the time step is too large, an "aliasing" effect occurs. This aliasing effect happens when the ray skips part of the velocity model and therefore gives inaccurate results. A small enough time step should, therefore, be used to avoid this effect. In the Jan Mayen region, this had to be considered, as the rays were traced over distances of 10km to 140km. In particular a very small time step was not practical, as the computational cost would be too high.

Another limitation is related to the accuracy of the 2-point ray tracing when estimating ray paths for the 3D velocity model. A large number of initial rays are required to conduct 2-point ray tracing, to accurately find ray paths from the source to the receivers.

However, a large number of rays also increase computation time. Unfortunately, the ray-tracing procedure for the 3D model was too time-consuming to relocate all events in the entire region accurately.

Rawlinson and Sambridge (2005) describe the fast marching algorithm, which could have been used for the ray tracing application in this thesis. The fast marching algorithm is a program with rapid calculations of first arrival phases in a heterogeneous medium. The algorithm is a grid-based numerical scheme for tracking the evolution of monotonically advancing interfaces. This is done via the finite-difference solution of the eikonal equation (Sethian, 1999). The algorithm would make a well-suited program for the relocation of the whole Jan Mayen area using the 3D velocity model, and for further analysis of these relocations.

7.2 Earthquake Location

7.2.1 Synthetic Test for Grid search methods

In order to better understand the difference between the two grid search methods implemented in this thesis, synthetic tests using a constant velocity medium and two station geometries were carried out in Section 5.3. The results from these tests show a clear difference between the contour plots for the different methods and geometries.

For events occurring inside the network of stations, the contour plots for the grid search methods are similar. The resolution in this geometry is, as expected, more constrained.

In this thesis, all events occur outside the network. The results from these tests show different contour plots. The traditional method is less sensitive to direction than the single-difference method. 1D profiles of the contour plots have been computed in both the x- and y-direction. Figure 7.2a shows a profile taken along the x-direction, for $y = 110$km, and Figure 7.2b a profile along the y-direction, for $x = 15$km. These figures show that the single-difference method better constrains the earthquake location than the traditional method. More constrained events are, therefore, expected for the single-difference method.

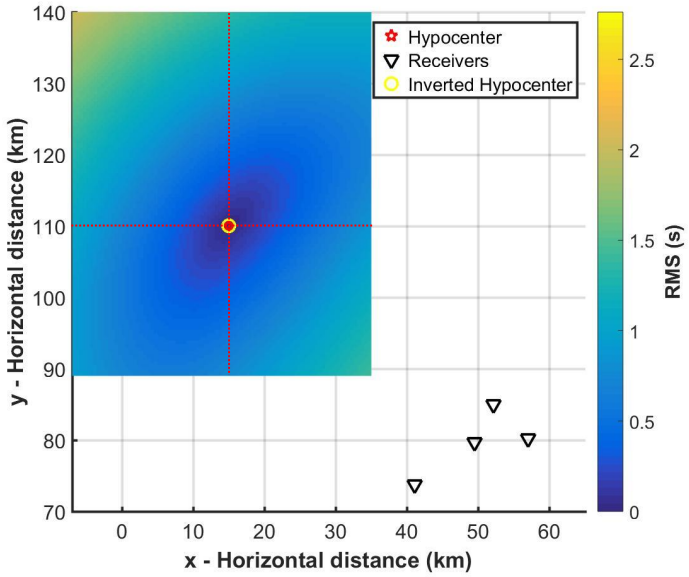

(a)

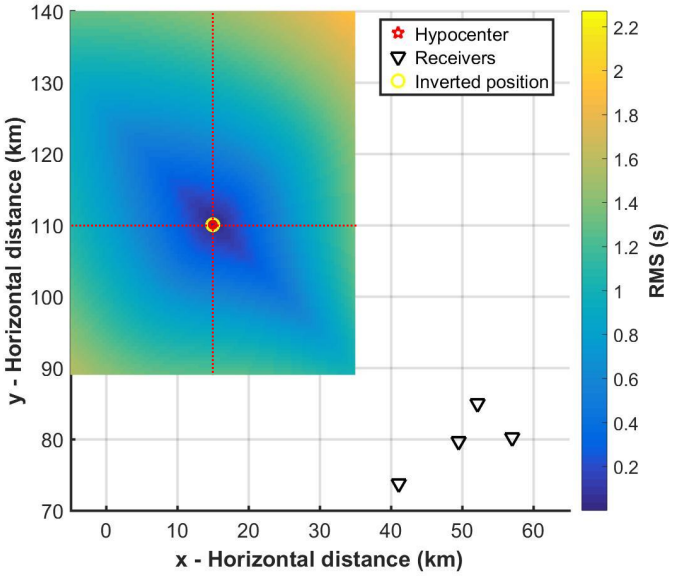

(b)

Figure 7.1: Synthetic test for the grid search methods. Figure (a) shows the traditional method. Figure (b) shows the contour plot for the traditional method. The red dashed lines indicate where the profiles in Figure 7.2 are taken.

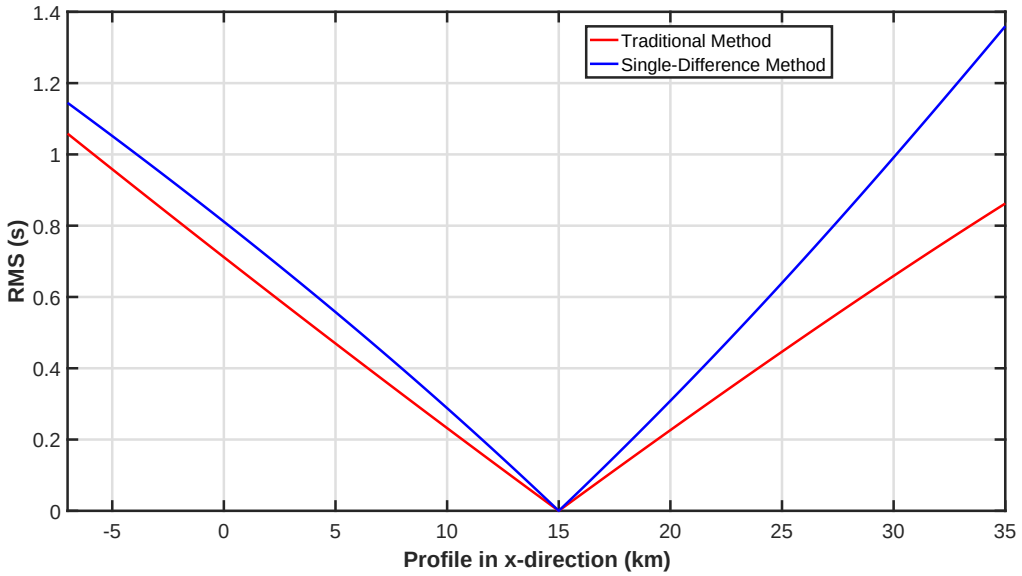

(a)

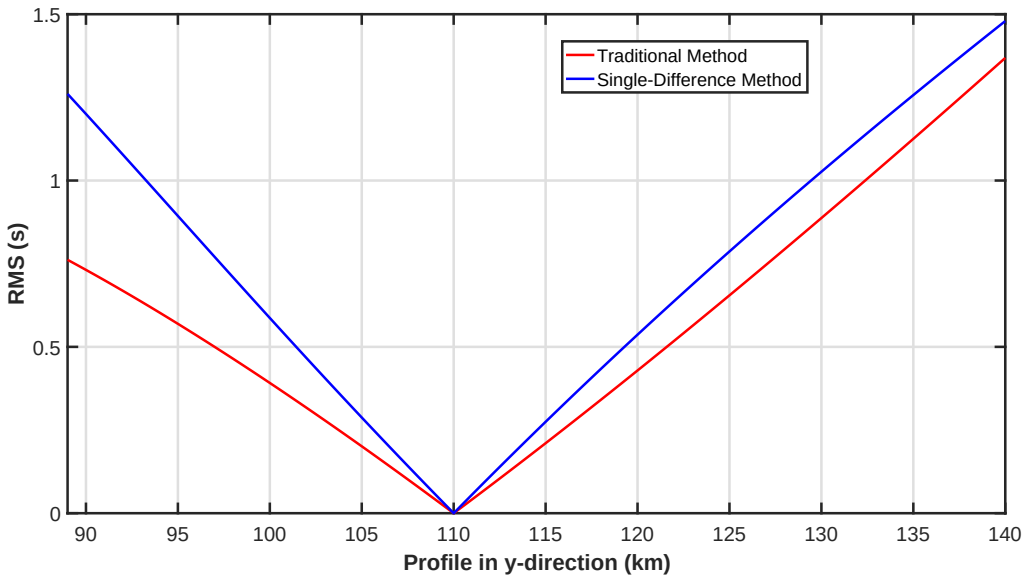

(b)

Figure 7.2: Profiles from the misfit function in Figure 7.1 illustrate the constraints of the different methods. Figure (a) shows profiles taken in the x-direction, for $y = 110$km, over the synthetic source. Figure (b) shows profiles taken in the y-direction, for $x = 15$km, over the synthetic source. The blue graph represents the traditional grid search methods. The red line the single-difference grid search method.

7.2.2 Relocation

An important issue is that for the real data example, there is no absolute reference available that the locations can be compared to. This makes it difficult to judge if the locations are of high or low quality. However, it is possible to see the overall trend in the locations and relate this to known tectonic features. If the events are, for example, located along a known existing fault then the relocations are likely to be an improvement.

In this thesis, three methods for locating and relocating 262 different earthquakes have been applied (see Table 9.1 for an overview of the relocations). This extensive relocation work was done using the linearized inversion in SEISAN, the traditional grid search method, and the single-difference method. The different methods provide different locations for the events. Only the results from Jan Mayen are discussed in this section, as Heimaey did not contain a sufficient amount of data.

The location methods all locate most of the events near the JMTF. The main difference between the methods lies in the spread of the locations as well as the existence of outliers.

The linearized inversion locations show a larger spread in earthquakes compared to the grid search methods. The traditional and the single-difference methods give similar locations (see Figures 6.10 and 6.13).

The grid search methods seem to result in better locations than the linearized inversion, in the sense that events are more localized in swarms along the JMTF, and there are less outliers. In total six swarms are found. The swarms furthest away show a higher level of spread in locations.

Seven outliers that were located south of Jan Mayen using the linearized inversion were relocated to the fracture zone by the grid search methods. The calculated contour plots of the misfit function for the events show two local minima, one in the south and one in the north (see, e.g., Figure 6.11 and 9.8). A closer look at the linearized inversion locations shows that the starting positions were estimated to the south-east of the island. Because of these starting positions, the events most likely converged to the local minimum in the south. The outliers found by the grid search methods, on the other hand, are partly results of a relatively low number of P-picks and partly because of uncertainties in the S-picks. This was the case for both methods, as seen in Figure 6.10 for the traditional

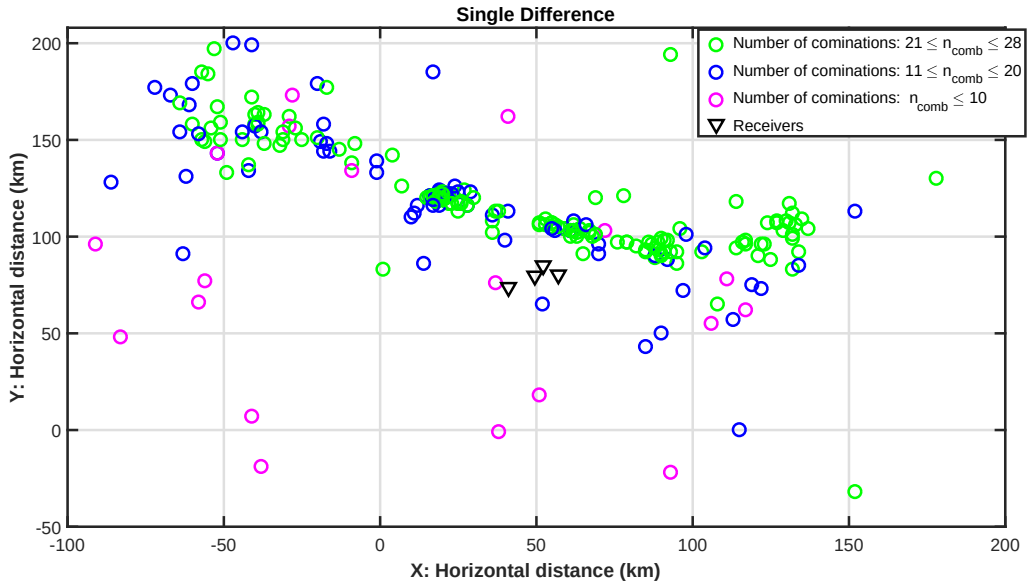

Figure 7.3: The earthquake locations in this figure have been divided into three groups depending on the number of difference combinations used in the single-difference method. The green circles indicate a number of combination between 21 and 28. The blue circles between 11 and 20 and the magenta circles corresponds to less than 10 combinations.

method and Figure 6.13 for the single-difference method. The outliers are especially clear for the single-difference method because this method requires a sufficient amount of clear arrivals to obtain an accurate location. Moreover, Figure 7.3 shows how the number of difference combinations in the single-difference grid search method affects the relocation of the events. The figure shows that the outliers mainly are produced by events with a relatively low number of combinations. When the number of combinations increases the locations improves, in the sense that events are more concentrated in the swarms.

The locations can be further improved by installing ocean bottom seismometers (OBS) in the vicinity of Jan Mayen. This would give better coverage of the network and more selected phases. Hence it should result in more accurate location estimates. However, the cost of such deployments is high.

Figures 6.17, 6.18, and 6.19 show the monthly distribution of when the different events in the Jan Mayen region occurred. A supplementary plot is given in Figure 7.4 to provide a better understanding of this distribution. This figure shows two sub-figures of the different swarms. The first shows the number of events in each swarm plotted on the day of the first event in the corresponding swarm. The second figure shows the distance from the

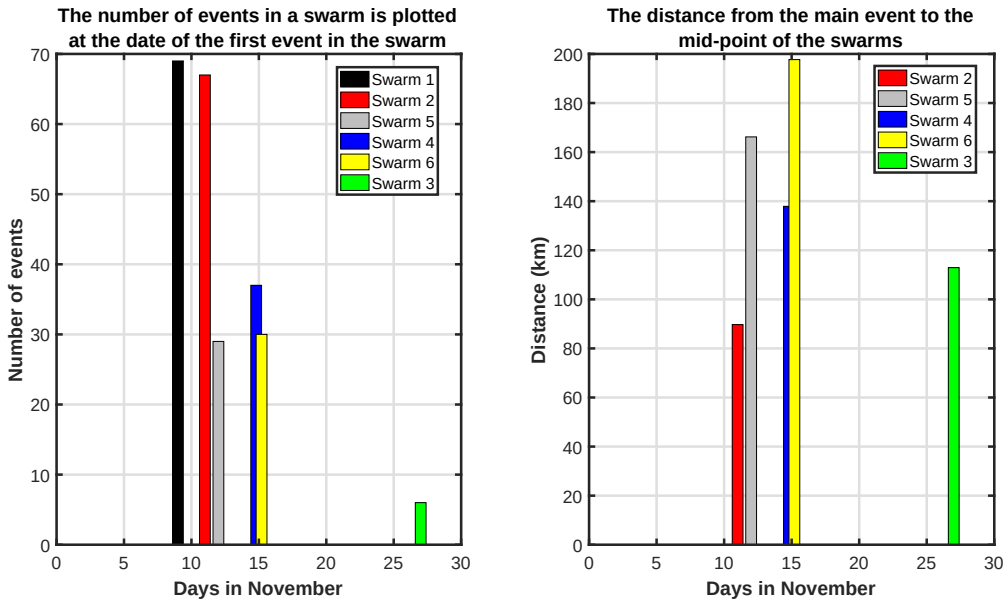

Figure 7.4: Two histograms containing background information on the six swarms. The first histogram shows the number of events plotted on the day the first event in the swarm occurred. The second histogram shows the distance from the main event to the swarms' center, also plotted on the day of the first event in the corresponding swarm.

main event, on November 9, to the center of the different swarms. These figures suggest that the swarms started more or less irregularly in time. It is, however, likely that the main event triggered swarm 2 to the north-west. Besides, the event propagation might be a result of energy being released in a part of the transform fault that was locked. A study of the source mechanisms should be executed to understand the origin of these events better. Several studies on earthquake swarms on transform faults have been done, for example by Roland and McGuire (2009) and Kuna et al. (2019).

The residual analysis made from Figure 6.16 shows that the events with the highest residuals occurred near the fracture zone. A reason for this can be that the 1D velocity model used in the analysis was not sufficient to resolve the heterogeneity of the fracture zone. Having said that, the number and the quality of the phases picked probably also plays a role. The relative high residual levels occur most likely because of a combination of these two factors.

Different velocity models have been introduced to study the effect they have on the earthquake location problem. In principle, a more detailed velocity model better represents the characteristics of the subsurface. It can, therefore, give better constraints to the

earthquake locations. Examples of this are given in Figure 7.5. This figure shows a test where computed synthetic arrival times were estimated with the 3D velocity model. The grid search was executed with the standard 1D velocity model. The results show that the location is shifted and that the 1D velocity model might not be sufficient to accurately estimate earthquake positions.

The relocation using the 3D velocity model shifted the events to the south and away from the fracture zone. This is most likely because of the low-velocity layer near the surface and suggests that the velocity model is inaccurate. To further improve the velocity model, a tomographic analysis is needed. For this, however, a relatively high number of data is required.

7.2.3 Uncertainty Analysis

The grid search methods also provide tools for uncertainty analysis. For example, they can be used to check whether the final location of the events was affected by a local minimum. The misfit contours can also be used to give accurate starting locations, e.g., for the linearized inversion as used in SEISAN. Note that the methods are time-consuming, so that the potential stating location would have limitations.

The error maps obtained using the different grid searches represent a simple way of estimating the errors of an event. A grid search can also provide an estimation of error volume. This is done by setting a specific upper or lower boundary to calculate the error volume. Figure 7.6 shows an example of this, where an error volume of the traditional method has been calculated.

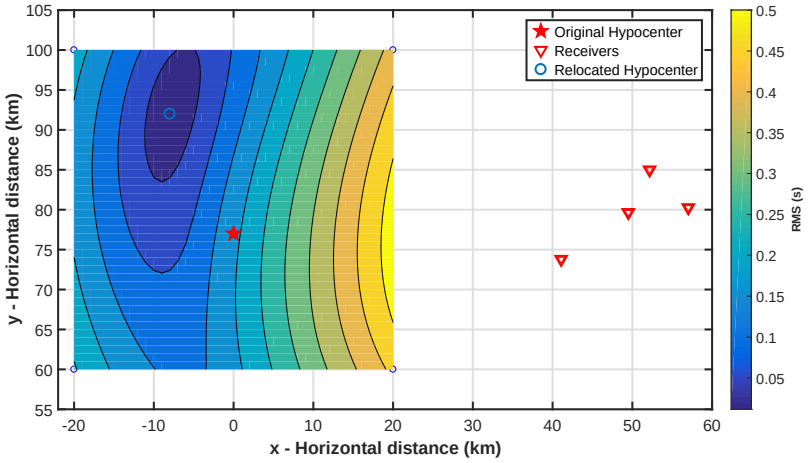

(a)

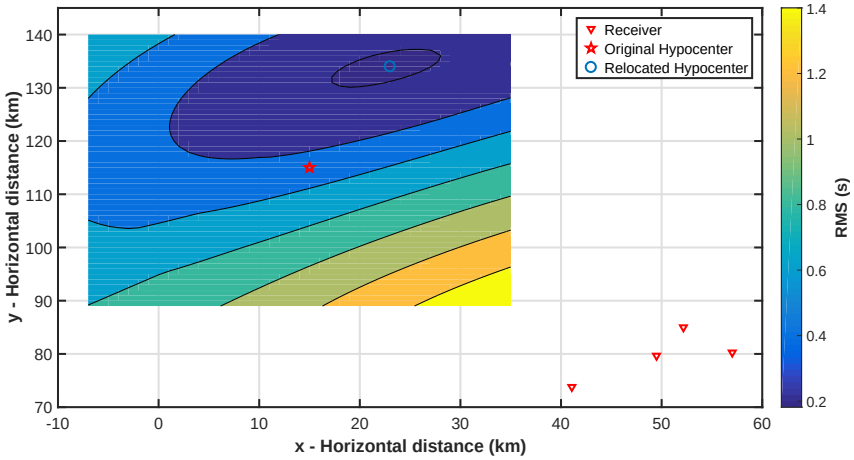

(b)

Figure 7.5: Contour plots of the misfit function of a synthetic event west of Jan Mayen, shown in figure (a), and another north-west of Jan Mayen, shown in (b). In this test, the computed synthetic arrival times were estimated with the 3D velocity model. Then the grid search was executed with the standard 1D velocity model. This test is executed to illustrate that the 3D velocity model of Jan Mayen might give a better location than a 1D model.

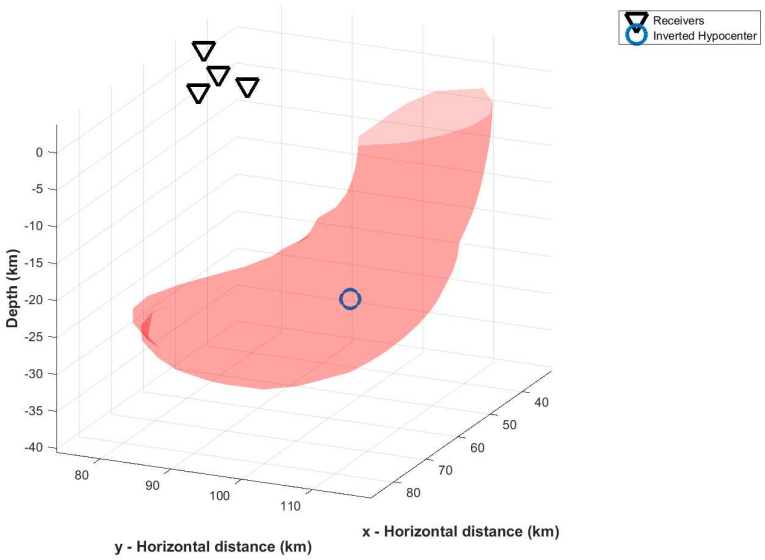

Figure 7.6: An example of error volume computation. A 95% isosurface of the misfit function has been calculated, and the uncertainty in the earthquake location is visible. The 95% is taken with respect to the absolute minimum of the misfit function.

7.3 Further Work

7.3.1 Computational Time

The ray tracing algorithms exhibit different computation times; the 3D ray-tracing is by far the slowest. The 1D methods vary, the layered velocity model is the fastest, and the smooth model the slowest of the two. The variation in computational costs is mostly caused by the interpolation methods used. The tri-linear interpolation method used in the 3D ray-tracing is more demanding than the linear interpolations used in the 1D ray-tracing. For the layered model, straight lines were computed, and no interpolation for velocity was needed. This made the method by far the most efficient. My implementation of the ray tracing was executed in MATLAB. Implementing the code using other programming languages, like C^{++} and Fortran, can reduce the computational time.

7.3.2 Earthquakes Locations

Additional analysis tools exists for solving the earthquake location problem, and it could be interesting to do further analysis with these. In particular, it would be interesting to implement the double difference algorithm to the data, as several studies have found it to improve the location of earthquakes (Waldhauser and Ellsworth, 2000).

7.3.3 Joint inversion for velocity and location

To improve the velocity model derived in this thesis, a joint inversion for velocity and location could be carried out. This, however, requires a significant number of arrival times that at the moment, does not seem to be available.

7.3.4 Study of Event Source Mechanism

To better understand the origin of the events in the six different swarms a study on their source mechanism should be executed. This would be done by picking the polarities of the phases of the biggest events.

Chapter 8

Conclusion

The main objective of this thesis was to study different aspects of solving the earthquake location problem and to investigate difficulties in locating earthquakes with sparse networks. This was done by using different velocity models, various ray tracing algorithms, and different location procedures at sparse oceanic island stations. In this thesis, it is investigated how all these effect the solution to the earthquake location problem in different ways.

Originally a station network was installed on Heimaey to study the seismicity in the region. Because too few events were recorded, a new data-set from Jan Mayen was included in the research. Three different location procedures did the relocation of the events in the two data-sets. A new velocity model was also used to relocate a swarm north-west of Jan Mayen.

Accurate travel time calculations were essential to find the most reliable solution to the earthquake location problem. The accuracy of travel times often comes at the cost of higher computation time. There is, however, a trade-off between the accuracy of the travel times and the computational time. This is why three different ray tracing algorithms were implemented in the thesis: one for a 1D layered discontinuous velocity medium, one for a 1D smooth velocity medium, and one for a 3D smooth velocity medium. From the application of the ray tracing algorithms to the location procedures, it was experienced a high computational cost of the 3D smooth ray tracing algorithm. The algorithm was applied to a swarm 50 km north-west of the seismic receivers on Jan Mayen.

The computational cost of the ray tracing algorithm can be reduced by implementing the algorithm in programming languages like C^{++} or Fortran.

The ray tracing was used to relocate earthquakes for the Heimaey and Jan Mayen data-set for two 1D velocity models and a 3D velocity model. The models used were a 1D velocity model for south-west Iceland, and a 1D and 3D velocity model for Jan Mayen. The Jan Mayen velocity models were derived from 1D and 2D velocity models found in the literature. The different methods show scattered locations for the events in the Heimaey network. This is likely because too few seismic phases could be identified. The relocation of the Jan Mayen data-set using the 1D velocity model and the grid search methods resulted in more concentrated swarms and events more localized to the fracture zone compared to the catalog locations. This suggests that the locations of the events improved after the application of the grid search methods. The monthly distribution implies that the main event might have triggered the swarm north-west of Jan Mayen and additional events east of Jan Mayen. Relocation of the swarm north-west of Jan Mayen using the 3D velocity model moved the events south-west and south relative to the six swarms. The events were, therefore, located away from the fracture zone. This was probably because of inaccuracies in the 3D velocity model. It, therefore, seems relevant to do 3D travel time tomography in this region, once enough data is available.

The grid search methods were also used as uncertainty analysis tools. Both methods indicated that the linearized inversion used in SEISAN estimated events to a local minimum south of Jan Mayen. This caused a few outliers. The uncertainty analysis tools also show that the grid search methods produced more accurate relocations when four selected P-phases were available than when two or three phases were available. The locations were especially uncertain when less than three P-phases were available.

One possibility to further improve the locations is to deploy OBSs in the vicinity of Jan Mayen.

Bibliography

Andrew, R. et al. (2008). *Volcanotectonic Evolution and Characteristic Colcanism of the Neovolcanic Zone of Iceland*. PhD thesis, Niedersächsische Staats-und Universitätsbibliothek Göttingen.

Auld, B. A. (1973). *Acoustic fields and waves in solids*. Wiley-Interscience.

Brander, J. and Wadge, G. (1973). Distance measurements across the Heimaey eruptive fissure. *Nature*, 244(5417):496.

Bretschneider, C. L. (1959). Wave variability and wave spectra for wind-generated gravity waves. Technical report, CORPS OF ENGINEERS WASHINGTON DC BEACH EROSION BOARD.

Cerveny, V. (2001). Seismic ray theory: Cambridge.

Dahlen, F., Hung, S.-H., and Nolet, G. (2000). Fréchet kernels for finite-frequency traveltimes—i. theory. *Geophysical Journal International*, 141(1):157–174.

De Berg, M., Van Kreveld, M., Overmars, M., and Schwarzkopf, O. (1997). Computational geometry. In *Computational geometry*, pages 1–17. Springer.

Demuth, A., Ottemöller, L., and Keers, H. (2016). Ambient noise levels and detection threshold in Norway. *Journal of seismology*, 20(3):889–904.

Geiger, L. (1912). Probability method for the determination of earthquake epicenters from the arrival time only. *Bull. St. Louis Univ*, 8(1):56–71.

Hardarson, B., Fitton, J., Ellam, R., and Pringle, M. (1997). Rift relocation—a geochemical and geochronological investigation of a palaeo-rift in northwest Iceland. *Earth and Planetary Science Letters*, 153(3-4):181–196.

Hasselmann, K. (1963). A statistical analysis of the generation of microseisms. *Reviews of Geophysics*, 1(2):177–210.

Havskov, J. and Atakan, K. (1991). Seismicity and volcanism of Jan Mayen Island. *Terra Nova*, 3(5):517–526.

Havskov, J. and Ottemöller, L. (2010). *Routine Data Processing in Earthquake Seismology*. Spinger, Bergen.

Havskov, J. and Ottemöller, L. (1999). SEISAN earthquake analysis software. *Seismol. Res. Lett.*, 70(5):532–534.

Havskov, J., Ottemöller, L., and Voss, P. (2009). Introduction to SEISAN and Computer exercises in processing earthquake data.

IMO (n.d.a). IMO bulletin. `http://hraun.vedur.is/ja/viku/`. [Online; accessed 20-04-2019].

IMO (n.d.b). Storhofdi - weather station - information. `https://en.vedur.is/weather/stations/?sid=6017`. [Online; accessed 20-04-2019].

Jakobsson, S. P. (1968). The geology and petrography of the Vestmann Islands: A preliminary report. *Surtsey Res Prog Rep*, 4:113–129.

Jakobsson, S. P. et al. (1979). Petrology of recent basalts of the Eastern Volcanic Zone, Iceland.

Jóhannesson, H. (1980). Jardlagaskipun og thróun rekbelta á Vesturlandi (English summary: Evolution of rift zones in Western Iceland). *Náttúrufrædingurinn*, 50:13–31.

Johnson, G. L. and Heezen, B. C. (1967). Morphology and evolution of the Norwegian-Greenland Sea. In *Deep Sea Research and Oceanographic Abstracts*, volume 14, pages 755–771. Elsevier.

Kandilarov, A., Mjelde, R., Pedersen, R.-B., Hellevang, B., Papenberg, C., Petersen, C.-J., Planert, L., and Flueh, E. (2012). The northern boundary of the Jan Mayen microcontinent, North Atlantic determined from ocean bottom seismic, multichannel seismic, and gravity data. *Marine Geophysical Research*, 33(1):55–76.

Kodaira, S., Mjelde, R., Gunnarsson, K., Shiobara, H., and Shimamura, H. (1998). Structure of the Jan Mayen microcontinent and implications for its evolution. *Geophysical Journal International*, 132(2):383–400.

Köhler, A. and Weidle, C. (2019). Potentials and pitfalls of permafrost active layer monitoring using the HVSR method: a case study in Svalbard. *Earth Surface Dynamics*, 7(1):1–16.

Kumar, D. and Ahmed, I. (2011). *Seismic Noise*, pages 1157–1161. Springer Netherlands, Dordrecht.

Kuna, V. M., Nábělek, J. L., and Braunmiller, J. (2019). Mode of slip and crust–mantle interaction at oceanic transform faults. *Nature Geoscience*, 12(2):138.

Lawver, L. A. and Muller, R. D. (1994). Iceland hotspot track. *Geology*, 22(4):311–314.

Li, L. K. (2017). *Location and Relocation of Seismic Sources*. PhD thesis, Uppsala University.

Lienert, B. R., Berg, E., and Frazer, L. N. (1986). HYPOCENTER: An earthquake location method using centered, scaled, and adaptively damped least squares. *Bulletin of the Seismological Society of America*, 76(3):771–783.

Lomax, A., Michelini, A., and Curtis, A. (2009). Earthquake location, direct, global-search methods. *Encyclopedia of complexity and systems science*, pages 2449–2473.

Madariaga, R. (2007). Seismic Source Theory. *Treatise on Geophysics, 4*, pages 59–82.

Mattsson, H. and Höskuldsson, Á. (2003). Geology of the Heimaey volcanic centre, south Iceland: early evolution of a central volcano in a propagating rift? *Journal of volcanology and geothermal research*, 127(1):55–71.

McNamara, D. E. and Boaz, R. (2005). Seismic noise analysis system, power spectral density probability density function: stand-alone software package. Technical report.

McNamara, D. E. and Buland, R. P. (2004). Ambient noise levels in the continental United States. *Bulletin of the seismological society of America*, 94(4):1517–1527.

Myhre, A. M., Eldholm, O., and Sundvor, E. (1984). The Jan Mayen Ridge: present status. *Polar Research*, 2(1):47–59.

Ottemöller, L., Voss, P., and Havskov, J. (2017). Seisan earthquake analysis software for Windows, Solaris, Linux and MacOsX. *Dept. Earth Sci., Univ. Bergen, Bergen, Norway*, 335.

Peterson, J. et al. (1993). Observations and modeling of seismic background noise.

Pierson Jr, W. J. and Moskowitz, L. (1964). A proposed spectral form for fully developed wind seas based on the similarity theory of SA Kitaigorodskii. *Journal of geophysical research*, 69(24):5181–5190.

Press, W. H., Teukolsky, S. A., Vetterling, W. T., and Flannery, B. P. (1992). Numerical recipes in C++. *The art of scientific computing*, 2:1002.

Pujol, J. (2003). *Elastic wave propagation and generation in seismology*. Cambridge University Press.

Rawlinson, N. and Sambridge, M. (2005). The fast marching method: an effective tool for tomographic imaging and tracking multiple phases in complex layered media. *Exploration Geophysics*, 36(4):341–350.

Rodríguez-Pérez, Q. and Ottemöller, L. (2014). Source study of the Jan Mayen transform fault strike-slip earthquakes. *Tectonophysics*, 628:71–84.

Roland, E. and McGuire, J. J. (2009). Earthquake swarms on transform faults. *Geophysical Journal International*, 178(3):1677–1690.

Sæmundsson, K. (1974). Evolution of the axial rifting zone in northern Iceland and the Tjornes fracture zone. *Geological Society of America Bulletin*, 85(4):495–504.

Sæmundsson, K. (1979). Outline of the geology of Iceland. *Jokull*, 29:7–28.

Sauer, T. (2014). *Pearson New International Edition: Numerical Analysis*. Pearson.

Schipper, C. I., Jakobsson, S. P., White, J. D., Palin, J. M., and Bush-Marcinowski, T. (2015). The Surtsey magma series. *Scientific reports*, 5:11498.

Sethian, J. A. (1999). *Level set methods and fast marching methods: evolving interfaces in computational geometry, fluid mechanics, computer vision, and materials science*, volume 3. Cambridge university press.

Snieder, R. (2002). General theory of elastic wave scattering. In *Scattering*, pages 528–542. Elsevier.

Sørensen, M. B., Ottemöller, L., Havskov, J., Atakan, K., Hellevang, B., and Pedersen, R. B. (2007). Tectonic processes in the Jan Mayen Fracture Zone based on earthquake occurrence and bathymetry. *Bulletin of the Seismological Society of America*, 97(3):772–779.

Sørne, A. and Navrestad, T. (1975). Seismie survey of Jan Mayen.

Stein, C. A. and Stein, S. (2003). Mantle plumes: heat-flow near Iceland. *Astronomy & Geophysics*, 44(1):1–8.

Stein, S. and Wysession, M. (2003). *An Introduction To Seismology, Earthquakes, and Earth Structure*. Blackwell Publishing Ltd., Malden.

Sylvester, A. (1975). History and surveillance of volcanic activity on Jan Mayen island. *Bulletin Volcanologique*, 39(2):313–335.

Talwani, M. and Eldholm, O. (1977). Evolution of the Norwegian-Geenland sea. *Geological Society of America Bulletin*, 88(7):969–999.

trac (n.d.). Earthworm Module: carlstatrig. `http://love.isti.com/trac/ew/wiki/carlstatrig`. [Online; accessed 20-11-2018].

Tryggvason, A., Rögnvaldsson, S. T., and Flóvenz, O. G. (2002). Three-dimensional imaging of the P-and S-wave velocity structure and earthquake locations beneath Southwest Iceland. *Geophysical Journal International*, 151(3):848–866.

Waldhauser, F. and Ellsworth, W. L. (2000). A double-difference earthquake location algorithm: Method and application to the northern Hayward fault, California. *Bulletin of the Seismological Society of America*, 90(6):1353–1368.

Chapter 9

Appendix

Figure 9.1: Additional pictures from the field installations of HEM1.

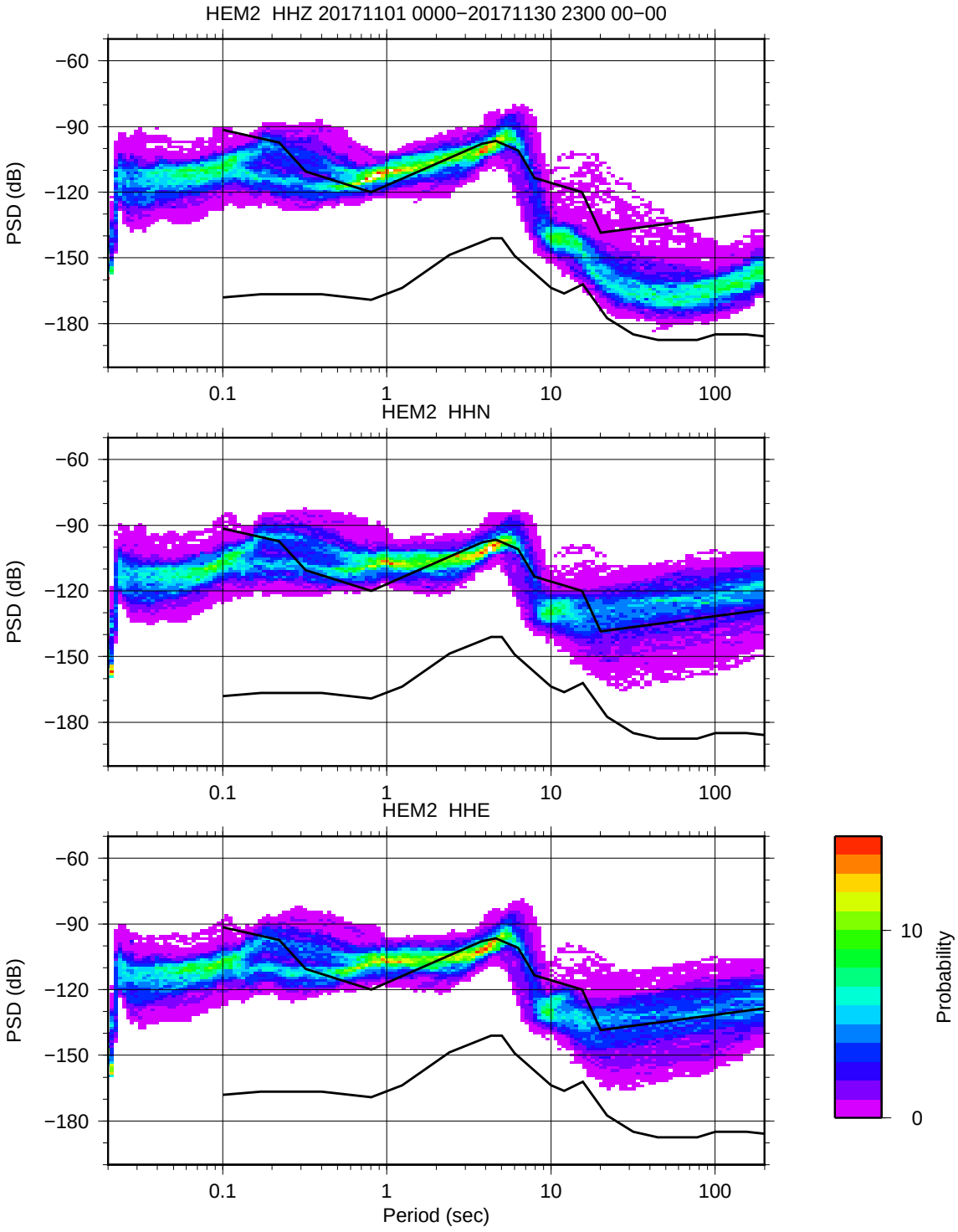

Figure 9.2: Noise plot for November 2017 for HEM2 (the temporary indoor UoB station).

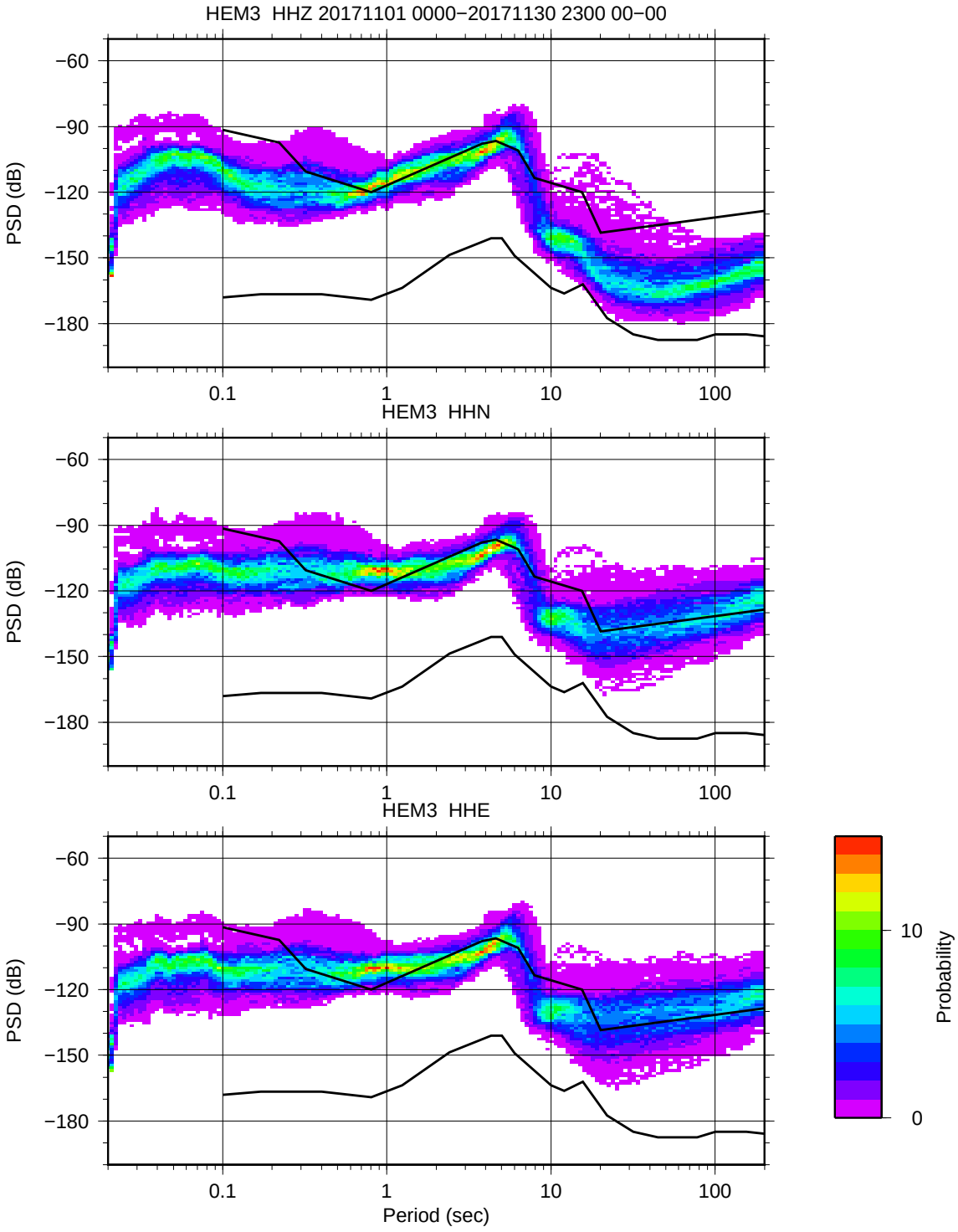

Figure 9.3: Noise plot for November 2017 for HEM3 (the temporary indoor UoB station).

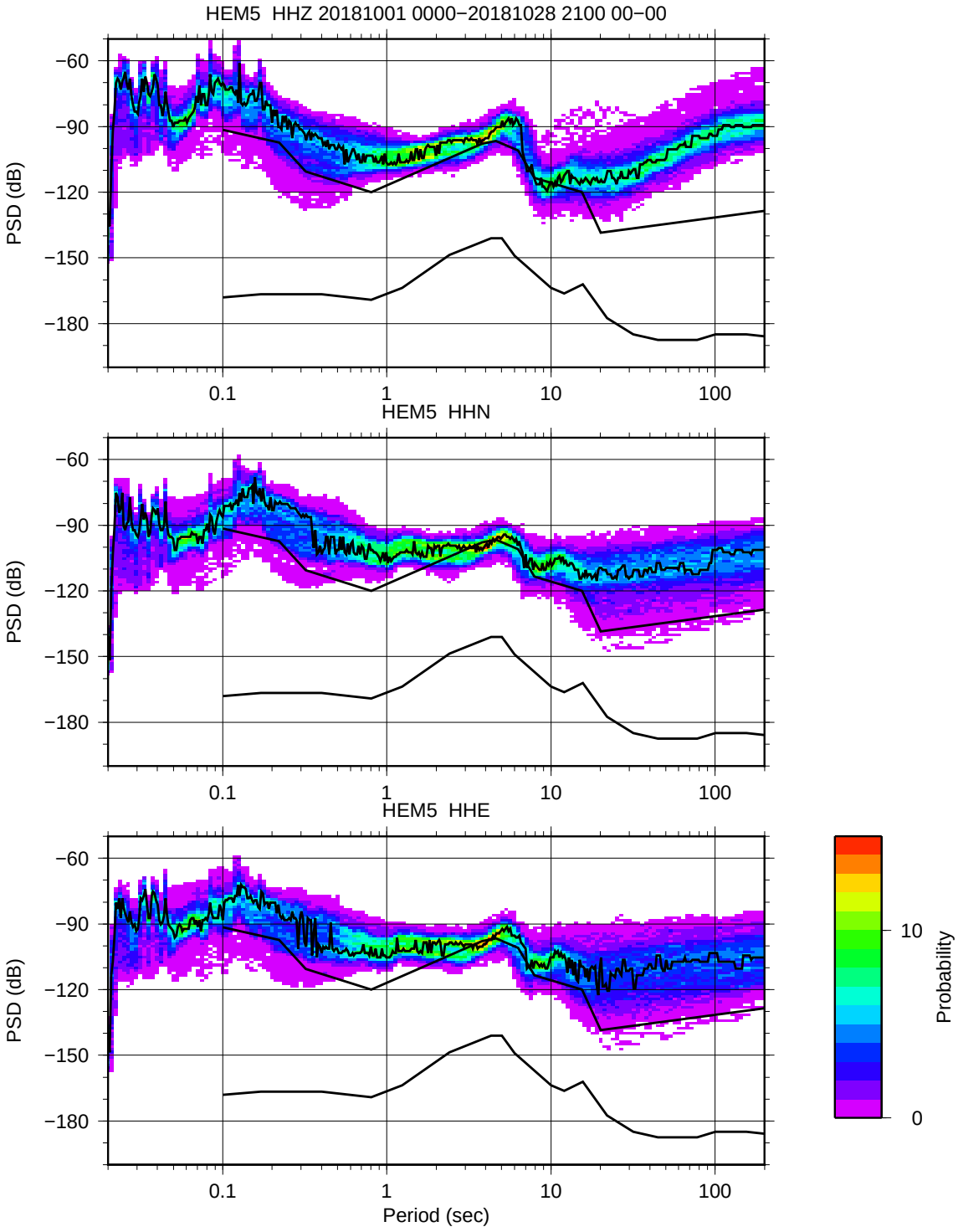

Figure 9.4: Noise plot for October 2018 for HEM5 (the temporary indoor UoB station).

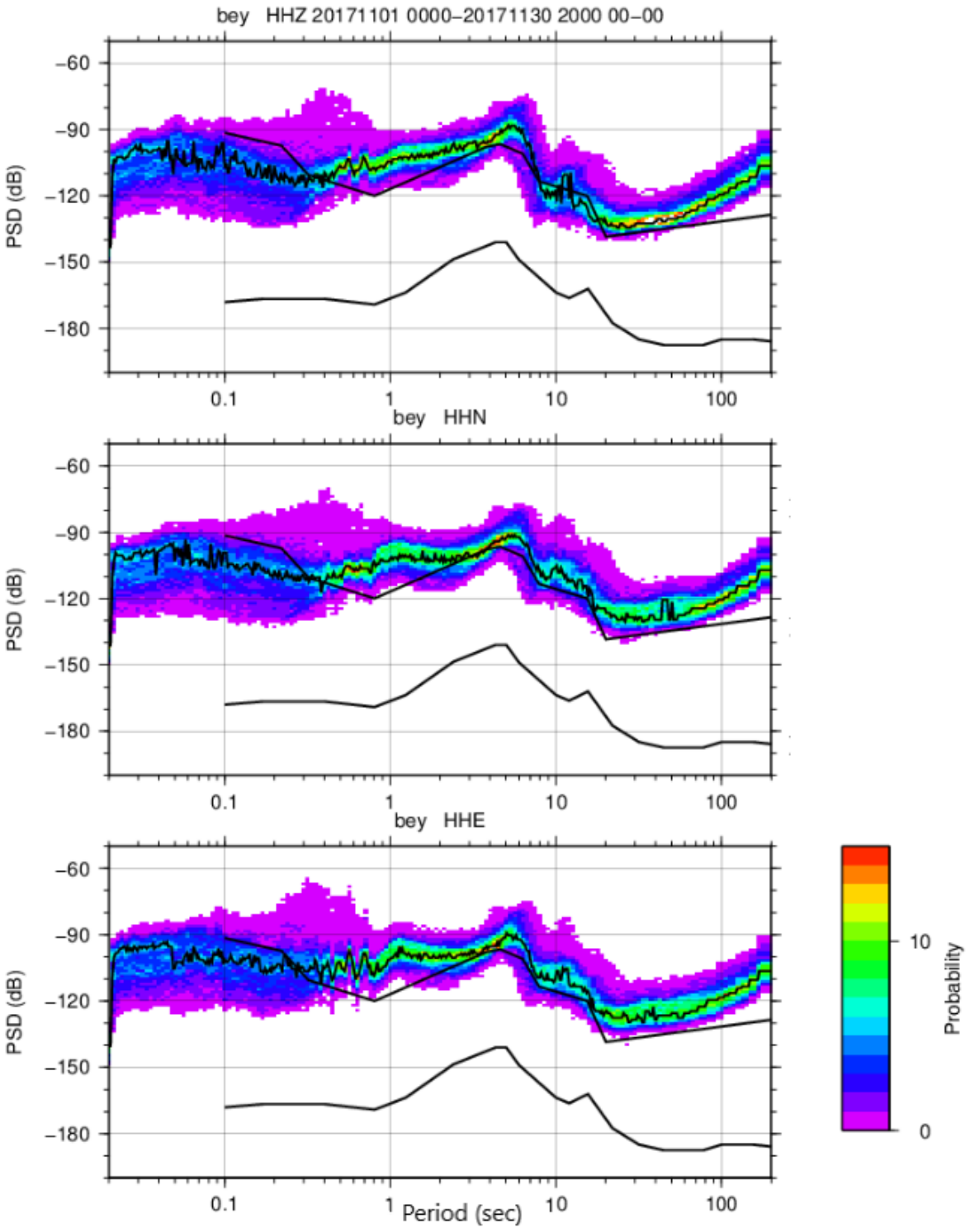

Figure 9.5: Noise plot for November 2017 for bey (the temporary outdoor IMO station). Note that the response does not seem correct. The microseismic peaks should have the same amplitude as the other stations. IMO was not able to help find the correct response.

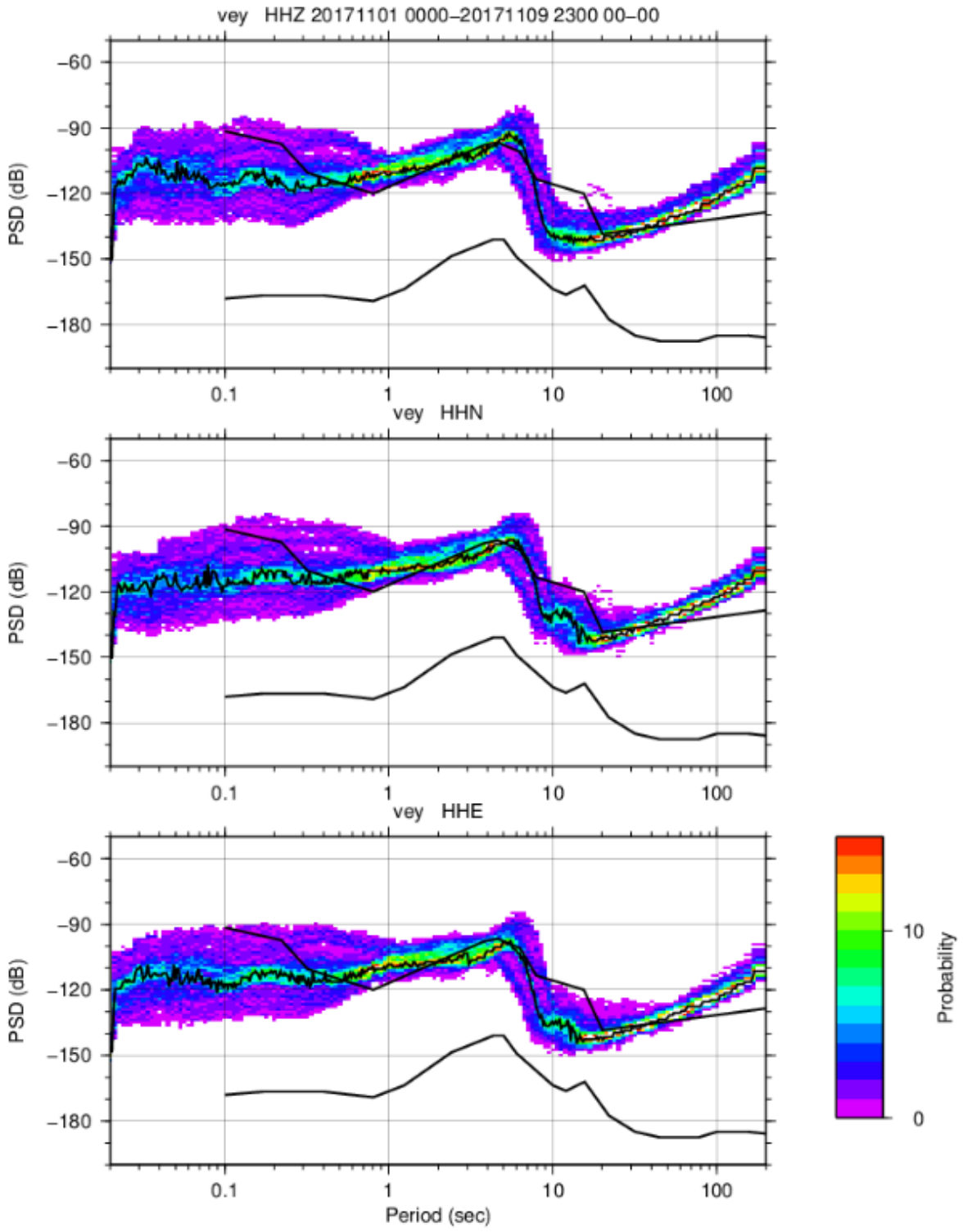

Figure 9.6: Noise plot for November 2017 for vey (the temporary outdoor IMO station).

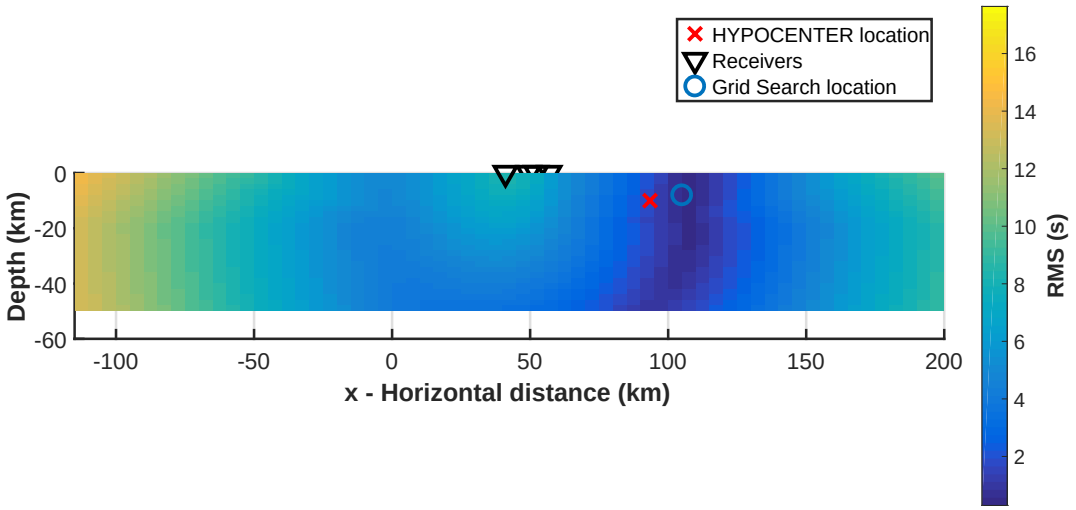

Figure 9.7: Contour plot of the misfit function of the magnitude 3.6 event which occurred on November 08, 2018 at 13:47:34. The contour plot illustrates the low depth resolution for an event east of Jan Mayen. The black triangles indicate the receivers, the blue circles denotes the location of the event after relocation and the red cross denotes the catalog location.

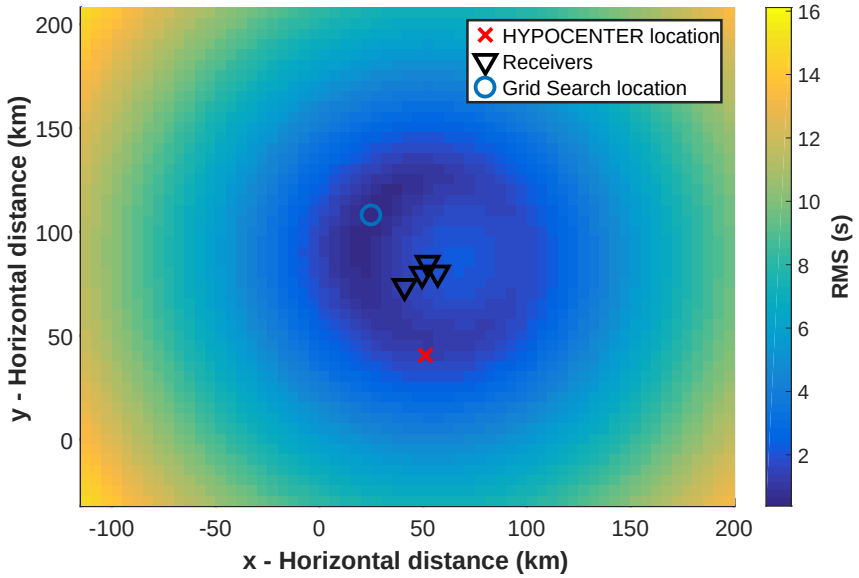

Figure 9.8: Contour plot of the misfit function of the magnitude 1.9 event which occurred on November 14, 2018 at 21:31:21. The figure shows that the location is highly uncertain. The high probability zone stretches from the relocated event in the north-west to the catalog event south of Jan Mayen.

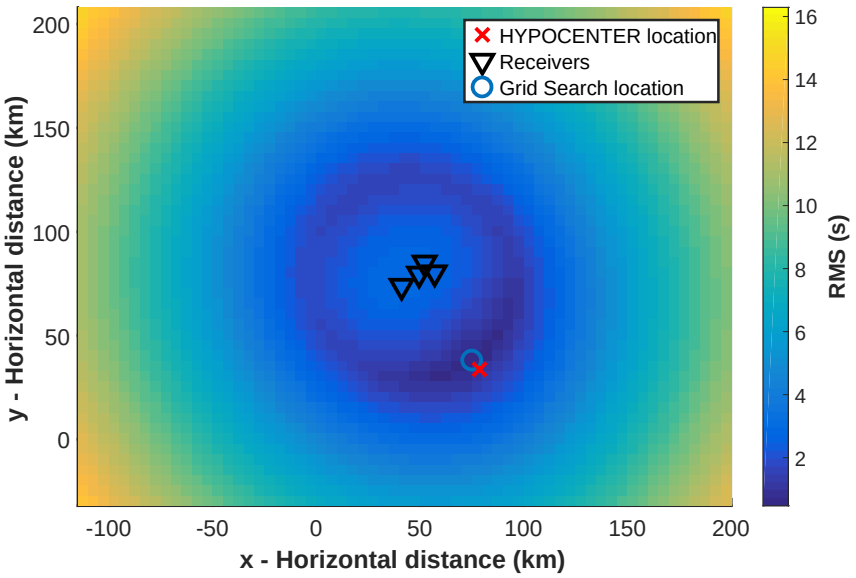

Figure 9.9: Contour plot of the misfit function of the magnitude 1.4 event which occurred on November 24, 2018 at 18:22:56. The figure illustrates an event that do not relocate from the south to the north-west Jan Mayen.

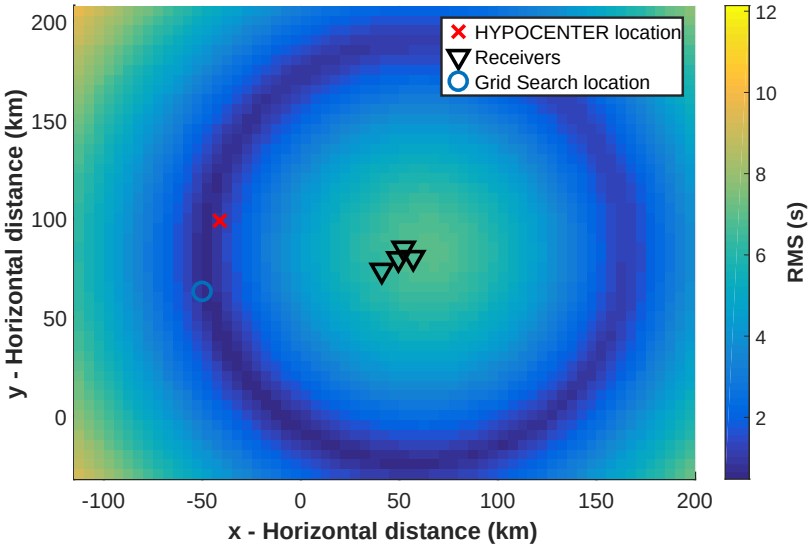

(a) Contour plots of the misfit function of the magnitude 2.1 event which occurred on November 9, 2018 at 05:36. The contour shows a direction insensitive location.

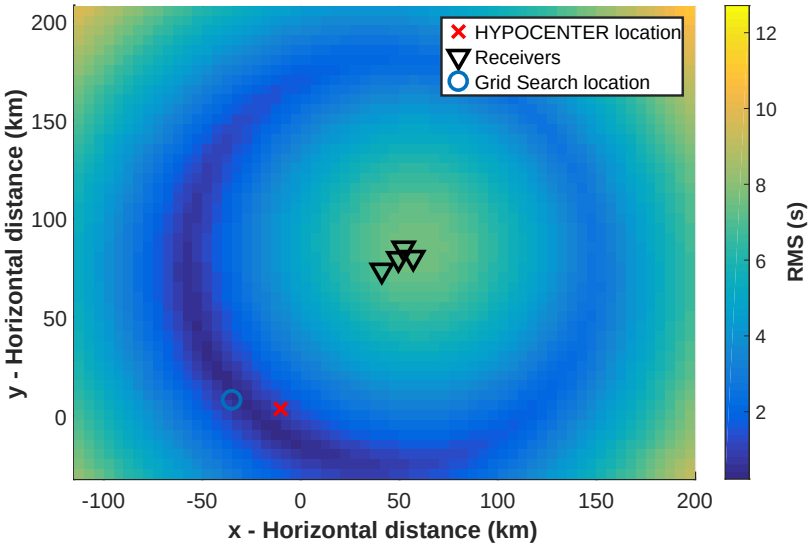

(b) Contour plot of the misfit function of the magnitude 2.2 event which occurred on January 8, 2019 at 20:41:32. The contour shows a direction insensitivity in the location.

Figure 9.10: Contour plots of the misfit function for two events that corresponds to outliers in the data. The misfit functions are calculated by the traditional grid search method.

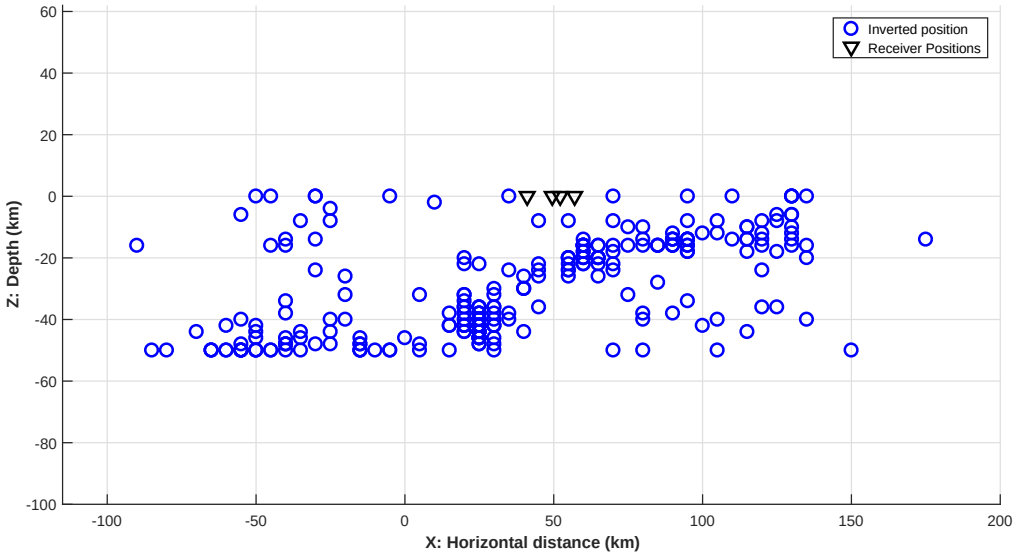

Figure 9.11: Depth plot of the relocated events after applying the single-difference method. The coarse grid search is applied to find the depths. An increment of (5,5,2)km was used.

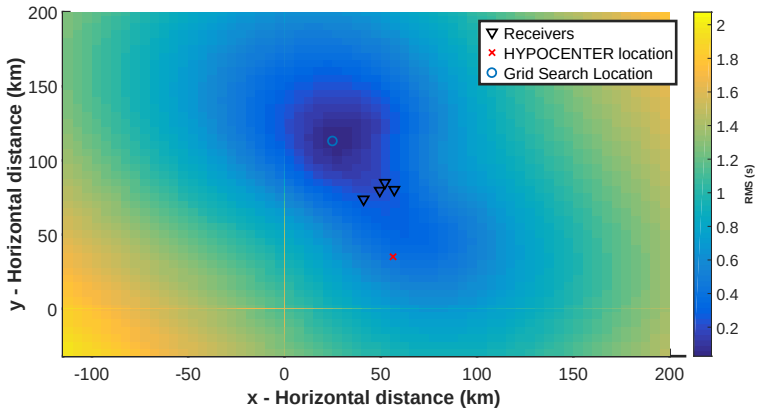

(a) Contour map of the misfit function for the magnitude 2.1 event which occurred on November 12, 2018 at 01:30:17.

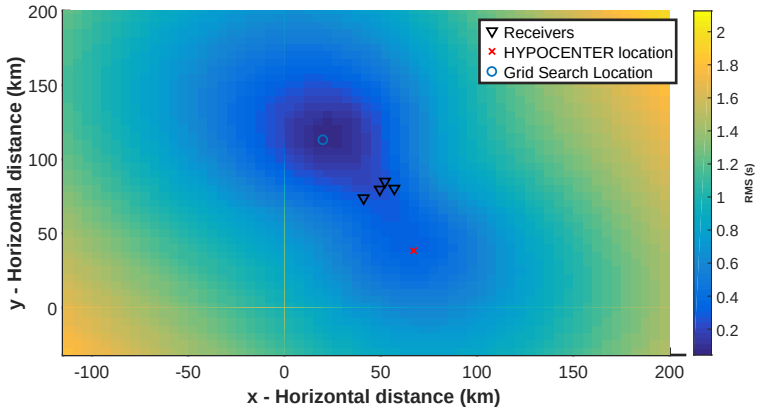

(b) Contour map of the misfit function for the magnitude 2.0 event which occurred on November 13, 2018 at 10:22:18.

Figure 9.12: Examples of two events that are relocated from the south of Jan Mayen to swarm 2 north-west of Jan Mayen. The misfit function was computed using the single-difference grid search method.

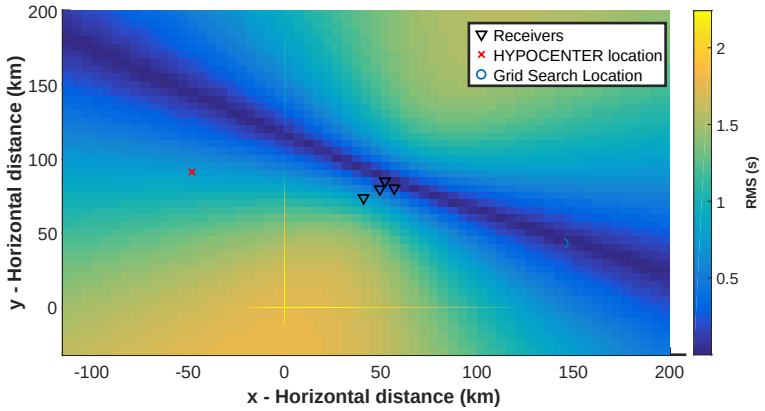

(a)

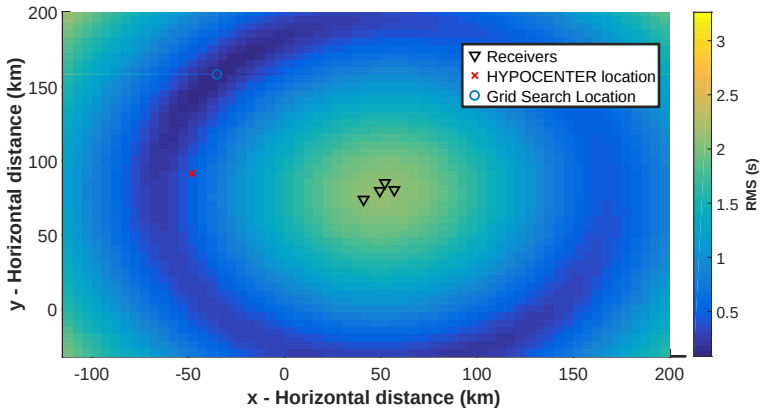

(b)

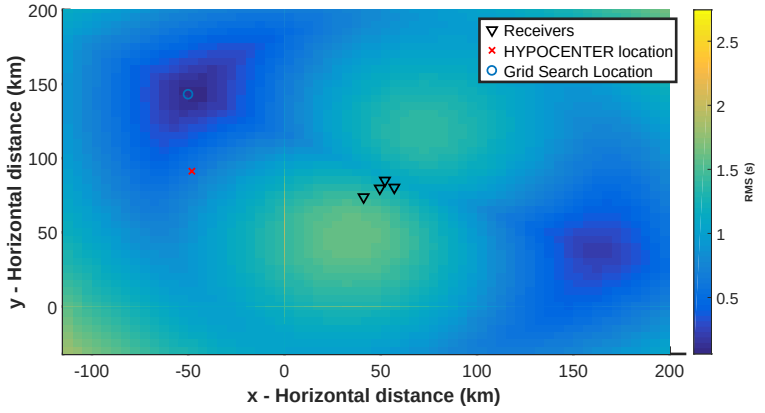

(c)

Figure 9.13: Example of an event relocated by the single-difference method. Figures (a), (b), and (c) show the contour plots of the misfit function for a magnitude 2.2 event with origin time November 09, 2018 at 03:07:3. Figure (a) shows the contour map of the single P-P difference grid search. Figure (b) shows the contour map of the single S-P difference grid search. Figure (c) shows the combination of single P-P difference and single S-P differences.

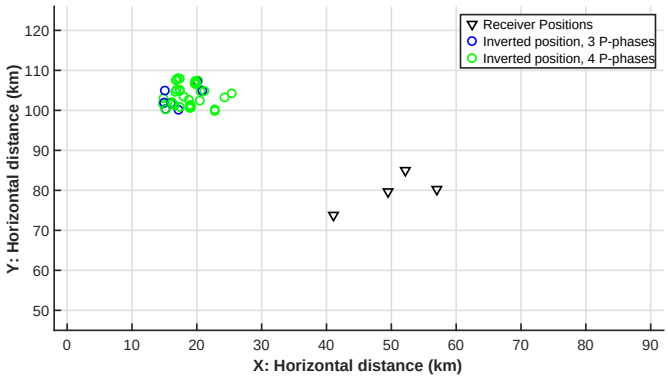

(a)

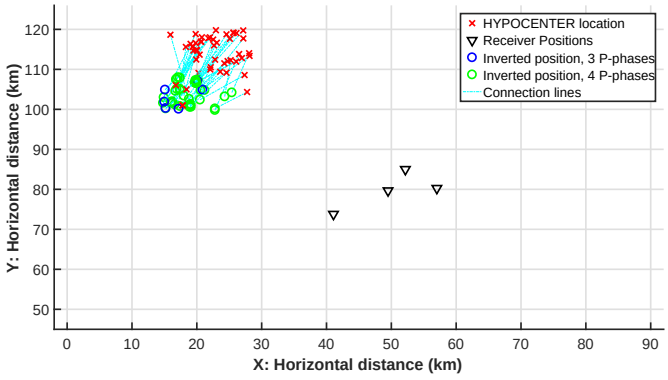

(b)

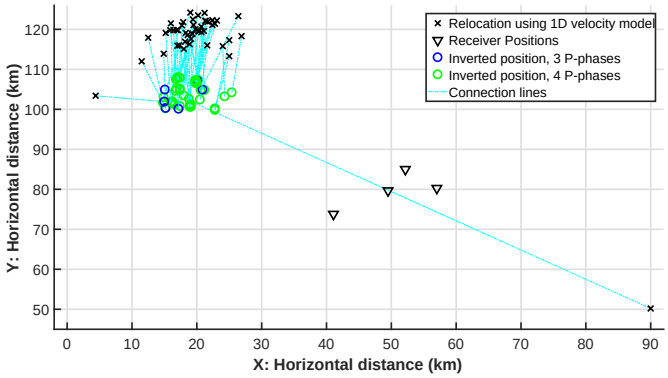

(c)

Figure 9.14: Relocation results using the 3D velocity model and the traditional grid search method. Figure (a) shows the relocated positions using the 3D velocity model. Figure (b) shows the 3D velocity model relocations relative to the catalog locations. Figure (c) shows the 3D velocity model relocations relative to the 1D velocity model relocations. The labels denote events with four-selected P-arrivals with a green circle, three-selected P-arrivals with blue circles, the receivers as black triangles, red crosses as the catalog events, the black crosses as the 1D positions after relocation, and the cyan dashed lines connect the relocated event with its corresponding catalog event.

Table 9.1: List of the relocations using HYPOCENTER, the traditional grid search method and the single-difference grid search method. The 1D velocity model for Jan Mayen has been used. The catalog locations are shown in columns 1 and 2. The traditional grid search relocations are given in columns 3 to 6 and the single difference in columns 7 to 10, columns 3 and 7 give the date (yyyy:mm:dd) of the event, columns 4 and 8 the origin time (OT) (hh:mm:ss), columns 5 and 9 the latitude (Lat°), columns 6 and 10 the longitude (Long°) and columns 11 and 12 show the number of selected P- and S-phases for the events.

Catalog location		**Traditional grid search relocation**				**Single-Difference grid search relocation**				**Phase**	
Lat (°)	Long (°)	Date	OT (GMT)	Lat (°)	Long (°)	Date	OT (GMT)	Lat (°)	Long (°)	P	S
71.175	-8.326	2018:11:6	19:31:46.8	71.247	-8.342	2018:11:6	19:31:46.8	71.238	-8.362	4	4
71.027	-7.299	2018:11:8	13:47:32.5	71.094	-7.036	2018:11:8	13:47:32.5	71.095	-7.025	4	4
71.703	-11.628	2018:11:9	1:49:38.0	71.624	-11.727	2018:11:9	1:49:38.2	71.630	-11.742	4	1
71.357	-11.912	2018:11:9	2:4:37.8	71.630	-11.705	2018:11:9	2:4:37.8	71.663	-11.636	4	4
71.561	-10.707	2018:11:9	2:10:10.0	71.710	-11.016	2018:11:9	2:10:10.0	71.715	-10.971	4	4
71.364	-10.768	2018:11:9	2:11:8.2	71.424	-11.150	2018:11:9	2:11:8.2	70.265	-6.774	3	3
71.332	-10.719	2018:11:9	2:26:27.9	71.455	-11.084	2018:11:9	2:26:28.1	71.460	-11.090	3	4
71.963	-11.099	2018:11:9	2:30:47.0	71.859	-11.822	2018:11:9	2:30:47.3	69.972	-5.833	4	4
71.539	-11.053	2018:11:9	2:39:0.7	71.692	-11.367	2018:11:9	2:39:0.8	71.651	-11.452	4	4
71.451	-9.711	2018:11:9	2:44:3.2	71.522	-9.849	2018:11:9	2:44:3.2	71.547	-9.808	4	4
71.496	-11.054	2018:11:9	2:52:26.1	71.643	-11.394	2018:11:9	2:52:26.1	71.588	-11.511	4	4
71.073	-11.205	2018:11:9	3:7:3.1	71.634	-11.179	2018:11:9	3:7:3.2	71.588	-11.511	2	4
71.477	-10.253	2018:11:9	3:48:21.6	71.583	-10.474	2018:11:9	3:48:21.6	71.597	-10.464	4	2
71.403	-11.307	2018:11:9	4:6:42.8	71.566	-11.303	2018:11:9	4:6:42.8	71.597	-10.464	4	4
71.513	-11.036	2018:11:9	4:11:37.2	71.634	-11.430	2018:11:9	4:11:38.1	70.092	-10.814	2	4
71.436	-7.207	2018:11:9	4:18:58.6	71.272	-6.403	2018:11:9	4:18:58.5	71.228	-6.341	4	3
71.48	-10.715	2018:11:9	4:32:6.0	71.714	-10.762	2018:11:9	4:32:6.0	71.710	-10.762	4	4
71.518	-10.933	2018:11:9	5:21:24.0	71.631	-11.099	2018:11:9	5:21:24.1	71.602	-11.166	4	4
71.145	-11.022	2018:11:9	5:36:40.3	70.873	-11.356	2018:11:9	5:36:39.6	70.945	-11.391	2	3
71.381	-12.402	2018:11:9	5:45:27.5	71.595	-12.236	2018:11:9	5:45:27.6	71.910	-11.588	4	4
71.416	-12.383	2018:11:9	5:56:54.1	72.059	-11.287	2018:11:9	5:56:54.9	72.045	-11.308	3	4
71.376	-10.995	2018:11:9	6:24:18.0	71.511	-11.414	2018:11:9	6:24:18.1	71.688	-11.030	4	4
71.517	-10.843	2018:11:9	7:35:37.4	71.803	-10.758	2018:11:9	7:35:38.0	71.811	-10.725	2	3
71.132	-12.905	2018:11:9	8:6:7.7	71.792	-12.065	2018:11:9	8:6:7.7	71.829	-12.012	3	4
71.326	-10.825	2018:11:9	8:27:38.3	71.471	-11.238	2018:11:9	8:27:38.3	71.443	-11.279	4	4
71.471	-10.635	2018:11:9	9:20:32.2	71.608	-10.519	2018:11:9	9:20:32.2	71.616	-10.498	4	4
71.45	-10.291	2018:11:9	10:32:55.5	71.564	-10.393	2018:11:9	10:32:55.3	71.560	-10.432	3	4
71.477	-9.853	2018:11:9	10:33:52.8	71.544	-10.111	2018:11:9	10:33:52.0	71.726	-8.761	2	4
71.366	-12.009	2018:11:9	13:20:45.1	71.482	-12.375	2018:11:9	13:20:45.8	71.797	-11.851	3	4
71.636	-10.851	2018:11:9	14:42:26.7	71.792	-11.133	2018:11:9	14:42:26.7	71.801	-11.097	4	4
71.328	-11.21	2018:11:9	21:38:34.0	71.614	-10.702	2018:11:9	21:38:35.1	70.072	-7.353	2	4
71.414	-11.58	2018:11:9	22:31:15.4	71.726	-11.044	2018:11:9	22:31:15.4	71.715	-11.079	4	4
71.628	-11.316	2018:11:9	23:2:56.1	71.767	-11.648	2018:11:9	23:2:56.3	71.752	-11.686	3	4
71.389	-12.371	2018:11:10	1:46:33.0	71.904	-11.524	2018:11:10	1:46:33.0	71.902	-11.518	4	4

71.502	-11.92	2018:11:10	4:38:25.2	71.708	-11.978	2018:11:10	4:38:26.0	71.883	-8.221	3	4
71.161	-10.572	2018:11:10	6:50:10.5	71.507	-10.159	2018:11:10	6:50:10.5	71.505	-10.164	4	4
71.29	-9.829	2018:11:10	19:6:38.3	71.369	-9.249	2018:11:10	19:6:38.3	71.360	-9.286	4	4
70.58	-7.36	2018:11:10	19:30:36.6	70.516	-7.054	2018:11:10	19:30:37.7	70.264	-8.819	2	3
71.364	-11.406	2018:11:11	12:20:20.3	71.845	-10.623	2018:11:11	12:20:20.3	71.868	-10.516	3	3
70.938	-7.457	2018:11:11	12:28:27.4	71.018	-7.218	2018:11:11	12:28:27.4	71.043	-7.269	4	4
71.251	-9.324	2018:11:11	17:15:29.3	71.370	-9.311	2018:11:11	17:15:29.2	71.362	-9.375	4	4
71.341	-9.164	2018:11:11	18:43:2.2	71.352	-9.333	2018:11:11	18:43:2.2	71.348	-9.324	4	4
70.589	-8.324	2018:11:12	1:30:16.9	71.336	-9.310	2018:11:12	1:30:16.8	71.345	-9.321	4	3
71.309	-9.635	2018:11:12	1:54:57.8	71.260	-9.616	2018:11:12	1:54:57.8	71.260	-9.624	3	3
71.318	-9.339	2018:11:12	2:10:39.5	71.351	-9.408	2018:11:12	2:10:39.5	71.359	-9.400	4	3
71.341	-9.177	2018:11:12	3:33:37.6	71.365	-9.283	2018:11:12	3:33:37.6	71.366	-9.289	4	3
71.326	-9.264	2018:11:12	3:59:24.9	71.367	-9.308	2018:11:12	3:59:24.9	71.363	-9.286	4	4
71.44	-10.917	2018:11:12	5:5:46.9	71.560	-11.339	2018:11:12	5:5:47.2	71.536	-11.395	3	4
71.316	-9.361	2018:11:12	6:49:58.7	71.355	-9.462	2018:11:12	6:49:58.7	71.358	-9.442	4	3
71.338	-9.34	2018:11:12	7:10:36.8	71.384	-9.376	2018:11:12	7:10:36.9	71.381	-9.368	4	2
71.292	-9.321	2018:11:12	14:22:7.0	70.722	-7.410	2018:11:12	14:22:6.9	70.722	-7.413	3	2
71.132	-9.412	2018:11:12	14:29:46.9	71.319	-9.264	2018:11:12	14:29:46.8	71.317	-9.278	4	4
71.357	-9.228	2018:11:12	14:32:31.6	71.401	-9.234	2018:11:12	14:32:32.0	71.405	-9.228	4	1
71.29	-9.106	2018:11:12	15:51:5.8	71.373	-9.174	2018:11:12	15:51:5.7	71.383	-9.138	4	3
71.214	-9.374	2018:11:12	18:23:15.1	71.348	-9.324	2018:11:12	18:23:15.1	71.361	-9.311	4	3
71.209	-9.114	2018:11:12	22:4:22.2	71.287	-9.182	2018:11:12	22:4:22.2	71.285	-9.188	4	3
71.281	-9.254	2018:11:12	23:52:0.9	71.338	-9.360	2018:11:12	23:52:1.1	71.336	-9.371	4	2
71.392	-10.005	2018:11:13	3:43:41.0	71.443	-10.254	2018:11:13	3:43:41.0	71.466	-10.169	2	4
70.647	-7.984	2018:11:13	5:52:35.7	71.361	-9.342	2018:11:13	5:52:35.7	71.360	-9.328	4	4
71.281	-9.335	2018:11:13	5:59:27.5	71.330	-9.536	2018:11:13	5:59:27.3	71.353	-9.445	4	2
71.329	-9.134	2018:11:13	8:37:28.2	71.309	-9.353	2018:11:13	8:37:28.2	71.312	-9.359	3	3
70.649	-8.369	2018:11:13	9:4:4.7	71.349	-9.341	2018:11:13	9:4:4.7	71.360	-9.294	4	3
71.31	-9.648	2018:11:13	9:6:12.5	71.351	-9.308	2018:11:13	9:6:12.5	71.336	-9.341	4	4
71.254	-9.231	2018:11:13	10:9:59.0	71.321	-9.396	2018:11:13	10:9:59.0	71.343	-9.327	4	3
70.618	-8.035	2018:11:13	10:22:18.6	71.340	-9.388	2018:11:13	10:22:18.6	71.338	-9.399	4	4
71.264	-9.272	2018:11:13	11:6:54.8	71.278	-9.586	2018:11:13	11:6:54.8	71.272	-9.592	3	3
71.303	-9.335	2018:11:13	12:17:37.1	71.343	-9.402	2018:11:13	12:17:37.2	71.349	-9.344	4	4
70.656	-7.995	2018:11:13	13:46:35.8	71.349	-9.310	2018:11:13	13:46:35.8	71.350	-9.299	4	4
71.301	-9.333	2018:11:13	19:4:3.5	71.339	-9.475	2018:11:13	19:4:3.3	71.352	-9.437	4	3
71.347	-9.135	2018:11:13	21:19:48.9	71.332	-9.354	2018:11:13	21:19:48.8	71.368	-9.241	3	3
71.223	-9.42	2018:11:13	21:50:36.0	71.191	-9.771	2018:11:13	21:50:36.0	71.309	-9.557	3	3
70.648	-8.455	2018:11:14	3:38:34.0	71.322	-9.429	2018:11:14	3:38:34.0	71.334	-9.399	4	3
71.559	-10.897	2018:11:14	5:28:9.7	71.663	-11.052	2018:11:14	5:28:9.7	71.666	-11.061	3	4
71.252	-9.204	2018:11:14	5:55:41.1	71.305	-9.392	2018:11:14	5:55:40.9	71.342	-9.349	4	3
71.329	-9.285	2018:11:14	6:44:20.3	71.387	-9.323	2018:11:14	6:44:20.3	71.374	-9.353	4	2
71.321	-9.317	2018:11:14	8:6:1.3	71.356	-9.392	2018:11:14	8:6:1.3	71.359	-9.384	4	4
71.087	-7.777	2018:11:14	10:20:34.3	71.111	-7.574	2018:11:14	10:20:34.3	71.125	-7.601	4	4
71.347	-9.253	2018:11:14	16:57:10.1	71.370	-9.364	2018:11:14	16:57:10.1	71.370	-9.356	4	3
71.338	-9.207	2018:11:14	21:12:1.4	71.353	-9.308	2018:11:14	21:12:1.4	71.355	-9.313	4	3
70.638	-8.465	2018:11:14	21:31:20.8	71.333	-9.441	2018:11:14	21:31:20.6	71.374	-9.328	4	3
71.104	-7.604	2018:11:14	23:15:33.7	71.114	-7.369	2018:11:14	23:15:33.9	71.062	-7.331	3	4
71.331	-9.313	2018:11:14	23:59:48.7	71.364	-9.401	2018:11:14	23:59:48.7	71.373	-9.353	4	2
71.336	-9.449	2018:11:15	0:9:6.5	71.337	-9.360	2018:11:15	0:9:6.7	71.338	-9.355	4	2

71.28	-9.187	2018:11:15	0:15:57.9	71.317	-9.231	2018:11:15	0:15:57.8	71.320	-9.206	4	4
71.386	-8.516	2018:11:15	0:37:17.4	71.417	-8.211	2018:11:15	0:37:17.6	71.372	-9.073	3	2
71.285	-9.139	2018:11:15	0:46:56.0	71.368	-9.244	2018:11:15	0:46:56.0	71.349	-9.338	4	4
70.885	-6.649	2018:11:15	1:4:48.9	70.908	-6.269	2018:11:15	1:4:48.6	71.009	-6.244	4	3
71.298	-9.412	2018:11:15	11:4:55.5	71.340	-9.509	2018:11:15	11:4:55.5	71.347	-9.464	4	4
71.278	-9.2	2018:11:15	1:27:48.4	71.351	-9.344	2018:11:15	1:27:48.3	71.357	-9.319	4	3
71.24	-9.014	2018:11:15	3:57:52.0	71.316	-9.099	2018:11:15	3:57:51.7	71.315	-9.105	4	1
71.313	-9.26	2018:11:15	4:20:51.4	71.349	-9.319	2018:11:15	4:20:51.4	71.344	-9.307	4	3
71.413	-8.701	2018:11:15	5:14:21.1	71.462	-8.625	2018:11:15	5:14:21.3	71.379	-9.183	3	2
71.366	-9.112	2018:11:15	5:35:52.5	71.346	-9.383	2018:11:15	5:35:52.5	71.337	-9.422	3	3
71.309	-9.352	2018:11:15	7:54:38.2	71.356	-9.367	2018:11:15	7:54:38.2	71.361	-9.350	4	4
71.319	-9.248	2018:11:15	8:35:28.9	71.368	-9.272	2018:11:15	8:35:29.0	71.369	-9.275	4	2
71.331	-9.278	2018:11:15	8:47:47.1	71.387	-9.323	2018:11:15	8:47:47.2	71.376	-9.348	4	2
71.444	-8.546	2018:11:15	9:51:42.2	71.495	-8.278	2018:11:15	9:51:42.8	71.368	-9.303	3	2
71.178	-9.389	2018:11:15	10:53:54.3	71.342	-9.321	2018:11:15	10:53:54.2	71.347	-9.302	4	4
71.187	-9.406	2018:11:15	13:38:15.1	71.315	-9.412	2018:11:15	13:38:14.9	71.340	-9.327	4	3
71.209	-10.034	2018:11:15	14:34:19.7	71.365	-9.333	2018:11:15	14:34:19.7	71.370	-9.342	4	4
71.24	-9.763	2018:11:15	16:53:20.1	71.328	-9.393	2018:11:15	16:53:20.1	71.352	-9.341	4	3
71.159	-8.286	2018:11:15	22:6:23.1	71.222	-8.287	2018:11:15	22:6:23.1	71.227	-8.317	4	4
71.313	-9.307	2018:11:17	12:1:47.5	71.317	-9.415	2018:11:17	12:1:47.3	71.349	-9.355	4	3
71.093	-7.375	2018:11:17	23:38:1.2	71.074	-7.253	2018:11:17	23:38:1.2	71.096	-7.249	4	4
71.149	-8.337	2018:11:18	2:34:31.8	71.217	-8.348	2018:11:18	2:34:31.8	71.212	-8.356	4	4
70.967	-6.407	2018:11:18	12:55:24.5	71.063	-6.174	2018:11:18	12:55:24.3	71.086	-6.169	4	3
71.259	-9.274	2018:11:18	16:54:49.3	71.294	-9.464	2018:11:18	16:54:49.3	71.330	-9.399	4	2
71.294	-9.711	2018:11:19	7:48:20.1	71.343	-9.330	2018:11:19	7:48:20.1	71.337	-9.327	4	4
71.277	-9.163	2018:11:19	11:13:25.7	71.355	-9.294	2018:11:19	11:13:25.7	71.357	-9.288	4	4
71.342	-9.177	2018:11:19	17:37:58.2	71.353	-9.257	2018:11:19	17:37:58.2	71.343	-9.330	3	2
71.472	-10.262	2018:11:19	21:35:44.8	71.600	-10.357	2018:11:19	21:35:44.6	71.592	-10.384	3	4
71.273	-9.214	2018:11:20	9:34:41.5	71.338	-9.363	2018:11:20	9:34:41.5	71.344	-9.330	4	3
70.91	-8.569	2018:11:21	5:15:32.9	70.856	-8.405	2018:11:21	5:15:33.0	70.862	-8.446	3	2
71.633	-10.387	2018:11:21	5:45:35.2	71.645	-10.854	2018:11:21	5:45:35.2	71.930	-9.445	3	3
71.515	-11.061	2018:11:21	12:24:38.8	71.643	-11.445	2018:11:21	12:24:38.8	71.676	-11.371	4	3
71.571	-10.564	2018:11:22	6:56:30.5	71.677	-10.723	2018:11:22	6:56:30.8	71.666	-10.756	1	3
71.119	-7.91	2018:11:23	6:9:27.6	71.127	-7.656	2018:11:23	6:9:27.6	71.141	-7.692	4	3
71.023	-9.263	2018:11:23	19:56:8.2	71.036	-9.499	2018:11:23	19:56:8.6	71.044	-9.494	3	4
71.391	-6.641	2018:11:24	5:4:55.6	71.193	-6.083	2018:11:24	5:4:55.5	71.193	-6.083	4	3
71.533	-11.812	2018:11:24	6:40:16.6	71.502	-12.317	2018:11:24	6:40:16.6	72.040	-11.142	3	3
71.321	-9.315	2018:11:24	16:50:32.0	71.346	-9.419	2018:11:24	16:50:32.0	71.361	-9.384	4	3
70.575	-7.724	2018:11:24	18:22:56.6	70.519	-7.800	2018:11:24	18:22:57.7	70.434	-8.466	2	4
71.084	-7.624	2018:11:24	18:28:31.7	71.143	-7.473	2018:11:24	18:28:31.7	71.136	-7.473	4	4
71.273	-11.452	2018:11:25	8:17:4.2	71.497	-11.717	2018:11:25	8:17:4.3	71.592	-11.528	4	4
71.289	-7.677	2018:11:25	19:42:26.2	71.255	-7.473	2018:11:25	19:42:25.5	71.357	-7.722	4	4
71.09	-7.365	2018:11:25	20:27:41.2	71.143	-7.332	2018:11:25	20:27:41.2	71.162	-7.389	4	4
71.051	-7.855	2018:11:26	13:19:12.3	71.140	-7.955	2018:11:26	13:19:12.3	71.134	-7.944	3	3
71.537	-11.54	2018:11:26	18:20:10.4	71.629	-11.952	2018:11:26	18:20:11.0	71.385	-12.325	3	4
71.232	-8.659	2018:11:27	19:18:19.4	71.297	-8.713	2018:11:27	19:18:19.6	71.284	-8.741	4	2
71.135	-8.169	2018:11:27	20:5:56.6	71.206	-8.176	2018:11:27	20:5:56.6	71.200	-8.176	3	3
70.924	-6.445	2018:11:28	6:25:13.6	71.131	-6.205	2018:11:28	6:25:13.6	71.162	-6.226	4	4
71.057	-8.109	2018:11:28	7:41:4.6	71.077	-7.965	2018:11:28	7:41:4.7	71.088	-7.940	3	3

71.286	-6.886	2018:11:30	12:49:41.0	71.289	-6.658	2018:11:30	12:49:41.7	71.320	-6.694	4	3
71.55	-10.642	2018:11:30	23:45:43.1	71.686	-11.007	2018:11:30	23:45:43.1	71.674	-11.031	4	4
71.485	-10.913	2018:12:1	17:8:35.3	71.624	-11.269	2018:12:1	17:8:35.8	71.424	-11.651	3	4
71.15	-8.239	2018:12:3	0:34:25.7	71.195	-8.173	2018:12:3	0:34:25.6	71.200	-8.181	3	4
70.708	-7.165	2018:12:4	1:22:15.0	70.726	-6.835	2018:12:4	1:22:14.7	70.780	-6.784	3	4
70.869	-6.972	2018:12:4	2:2:13.8	70.994	-6.589	2018:12:4	2:2:14.0	70.934	-6.617	3	4
71.065	-6.82	2018:12:4	3:16:13.5	70.935	-6.592	2018:12:4	3:16:13.8	70.825	-6.663	2	3
71.168	-8.014	2018:12:5	11:2:37.5	71.189	-7.884	2018:12:5	11:2:40.1	71.200	-7.884	2	3
71.425	-9.741	2018:12:5	18:32:49.4	71.515	-9.947	2018:12:5	18:32:49.4	71.517	-9.933	3	3
70.862	-6.859	2018:12:6	0:8:33.7	71.045	-6.424	2018:12:6	0:8:33.7	71.050	-6.435	4	4
71.462	-10.858	2018:12:6	4:21:5.4	71.655	-10.954	2018:12:6	4:21:5.3	71.639	-11.001	3	4
71.477	-10.678	2018:12:6	21:45:7.1	71.593	-10.944	2018:12:6	21:45:7.1	71.585	-10.968	4	4
71.234	-10.883	2018:12:6	22:4:50.8	71.385	-11.263	2018:12:6	22:4:50.9	70.844	-11.433	2	3
71.403	-10.603	2018:12:6	22:10:4.2	71.540	-10.985	2018:12:6	22:10:4.2	71.482	-11.096	4	4
71.134	-8.099	2018:12:7	7:43:18.3	71.207	-8.109	2018:12:7	7:43:18.3	71.209	-8.101	4	4
71.138	-8.225	2018:12:7	10:39:45.2	71.205	-8.245	2018:12:7	10:39:45.2	71.210	-8.254	4	4
71.503	-10.473	2018:12:8	22:10:20.7	71.558	-10.358	2018:12:8	22:10:20.9	71.561	-10.373	3	4
70.919	-6.952	2018:12:9	8:33:30.5	71.002	-6.814	2018:12:9	8:33:30.2	70.969	-6.814	1	3
71.382	-6.333	2018:12:9	11:16:27.9	71.401	-5.807	2018:12:9	11:16:28.8	71.265	-5.639	3	4
71.385	-11.107	2018:12:10	7:51:55.5	71.607	-11.323	2018:12:10	7:51:55.5	71.600	-11.351	4	4
71.405	-11.28	2018:12:19	21:42:29.5	71.573	-11.233	2018:12:19	21:42:29.5	71.847	-10.419	4	4
70.635	-8.646	2018:12:23	6:54:54.7	70.616	-8.609	2018:12:23	6:54:53.2	70.660	-7.549	3	3
70.985	-6.981	2018:12:23	6:55:6.4	71.002	-6.842	2018:12:23	6:55:6.3	70.849	-6.917	4	4
71.012	-8.45	2018:12:24	8:59:34.6	71.181	-7.982	2018:12:24	8:59:34.6	71.186	-8.034	4	4
71.181	-8.859	2018:12:24	8:59:34.6	71.162	-7.955	2018:12:24	8:59:34.5	71.169	-7.990	4	4
71.025	-7.593	2018:12:27	3:2:33.4	71.060	-7.428	2018:12:27	3:2:33.4	71.068	-7.460	4	4
71.473	-10.381	2018:12:27	18:43:22.1	71.622	-10.746	2018:12:27	18:43:22.2	71.607	-10.786	4	4
71.095	-7.663	2018:12:29	23:3:26.8	71.075	-7.441	2018:12:29	23:3:26.8	71.076	-7.457	3	3
71.019	-8.808	2018:12:30	2:51:36.3	71.046	-9.003	2018:12:30	2:51:36.7	70.955	-8.841	2	3
71.301	-9.348	2018:12:30	3:37:39.0	71.350	-9.439	2018:12:30	3:37:39.0	71.355	-9.411	4	4
71.436	-11.128	2019:1:2	21:21:31.8	71.568	-10.850	2019:1:2	21:21:31.9	71.578	-10.817	4	4
71.132	-8.262	2019:1:2	23:27:59.7	71.175	-8.218	2019:1:2	23:27:59.8	71.168	-8.193	4	4
71.424	-11.601	2019:1:5	14:15:9.8	71.707	-11.509	2019:1:5	14:15:9.8	71.745	-11.410	4	4
71.089	-7.484	2019:1:5	17:59:59.8	71.154	-7.289	2019:1:5	17:59:59.8	71.154	-7.336	4	4
71.016	-6.635	2019:1:8	6:22:54.7	71.183	-6.310	2019:1:8	6:22:54.7	71.181	-6.310	4	4
70.299	-10.097	2019:1:8	20:41:32.4	70.321	-10.898	2019:1:8	20:41:32.7	70.324	-10.925	2	4
70.957	-11.285	2019:1:8	21:5:52.7	71.051	-11.602	2019:1:8	21:5:52.6	71.063	-11.621	3	4
71.174	-8.362	2019:1:9	3:17:4.1	71.231	-8.348	2019:1:9	3:17:4.1	71.233	-8.367	4	4
71.309	-9.381	2019:1:9	5:22:11.9	71.353	-9.451	2019:1:9	5:22:11.8	71.362	-9.409	4	4
71.199	-8.638	2019:1:18	7:2:4.6	71.262	-8.771	2019:1:18	7:2:4.6	71.245	-8.897	4	4
71.207	-8.172	2019:1:23	7:32:25.1	71.198	-8.034	2019:1:23	7:32:25.1	71.195	-8.023	4	4
71.11	-6.409	2019:1:25	8:6:49.8	71.214	-6.187	2019:1:25	8:6:49.8	71.212	-6.178	4	4
71.305	-12.416	2019:1:25	11:29:8.1	72.007	-11.506	2019:1:25	11:29:7.9	72.015	-11.481	4	3
71.021	-7.479	2019:1:30	16:49:0.3	71.099	-7.312	2019:1:30	16:49:0.3	71.100	-7.301	4	4
71.356	-9.917	2019:1:31	14:37:26.7	71.456	-9.968	2019:1:31	14:37:27.0	71.458	-9.926	3	4
71.175	-8.224	2019:2:6	7:44:21.9	71.220	-8.153	2019:2:6	7:44:21.9	71.228	-8.161	4	4
71.572	-10.736	2019:2:7	14:24:36.9	71.729	-11.027	2019:2:7	14:24:36.9	71.730	-11.030	4	4
71.017	-6.643	2019:2:8	12:30:35.4	71.217	-6.362	2019:2:8	12:30:35.4	71.218	-6.350	4	4
71.487	-10.84	2019:2:8	16:18:38.1	71.627	-11.201	2019:2:8	16:18:38.1	71.635	-11.171	3	4

71.222	-8.202	2019:2:9	19:50:31.5	71.234	-8.095	2019:2:9	19:50:31.8	71.246	-8.169	3	4
71.149	-8.371	2019:2:11	6:44:41.3	71.221	-8.434	2019:2:11	6:44:41.3	71.229	-8.481	4	4
70.975	-6.959	2019:2:12	18:42:35.2	71.144	-6.630	2019:2:12	18:42:35.2	71.142	-6.625	4	3
71.105	-7.586	2019:2:13	15:39:26.4	71.147	-7.412	2019:2:13	15:39:26.4	71.141	-7.412	4	4
71.13	-7.38	2019:2:17	17:15:17.2	71.193	-7.192	2019:2:17	17:15:17.2	71.200	-7.214	4	4
70.969	-6.593	2019:2:20	2:20:57.1	71.153	-6.208	2019:2:20	2:20:57.1	71.151	-6.222	4	4
71.035	-6.466	2019:2:20	2:32:35.7	71.218	-6.256	2019:2:20	2:32:35.7	71.218	-6.236	4	4
71.046	-7.531	2019:2:21	5:0:57.4	71.080	-7.504	2019:2:21	5:0:57.4	71.098	-7.525	4	4
71.054	-7.681	2019:2:21	7:19:40.4	71.102	-7.533	2019:2:21	7:19:40.4	71.104	-7.516	4	4
71.296	-9.108	2019:2:28	7:16:0.5	71.334	-9.145	2019:2:28	7:16:0.5	71.334	-9.167	4	4
70.981	-6.467	2019:3:2	7:56:27.2	71.141	-6.209	2019:3:2	7:56:27.5	71.023	-6.184	3	4
71.535	-11.147	2019:3:4	11:45:2.0	71.664	-11.503	2019:3:4	11:45:2.5	70.667	-12.082	2	4
71.052	-7.214	2019:3:4	17:28:10.2	71.060	-6.539	2019:3:4	17:28:10.2	71.072	-6.546	4	4
71.476	-11.967	2019:3:5	0:57:18.4	71.772	-11.729	2019:3:5	0:57:18.4	71.760	-11.750	4	4
71.192	-9.665	2019:3:6	6:33:50.6	71.310	-9.135	2019:3:6	6:33:50.6	71.325	-9.172	4	4
71.148	-8.249	2019:3:6	11:37:54.3	71.204	-8.187	2019:3:6	11:37:54.4	71.195	-8.195	4	4
71.331	-6.568	2019:3:7	3:9:36.4	71.312	-6.217	2019:3:7	3:9:36.3	71.312	-6.231	4	4
71.145	-8.23	2019:3:7	4:50:23.5	71.199	-8.148	2019:3:7	4:50:23.5	71.201	-8.173	4	4
71.128	-8.186	2019:3:7	15:5:44.2	71.193	-8.179	2019:3:7	15:5:43.9	71.196	-8.176	3	4
70.974	-6.931	2019:3:7	23:8:33.1	71.123	-6.646	2019:3:7	23:8:33.1	71.122	-6.641	4	4
71.56	-10.491	2019:3:8	11:7:7.7	71.585	-10.684	2019:3:8	11:7:7.7	71.609	-10.622	4	4
71.485	-10.316	2019:3:8	11:9:44.1	71.630	-10.610	2019:3:8	11:9:44.0	71.678	-10.447	3	4
71.125	-8.174	2019:3:8	21:7:34.6	71.193	-8.154	2019:3:8	21:7:34.6	71.190	-8.120	4	4
71.435	-5.341	2019:3:9	4:2:49.1	71.456	-4.934	2019:3:9	4:2:49.1	71.404	-4.910	4	4
71.441	-9.984	2019:3:9	6:44:21.9	71.545	-10.340	2019:3:9	6:44:21.9	71.565	-10.266	4	4
71.189	-8.365	2019:3:10	14:17:42.6	71.251	-8.420	2019:3:10	14:17:42.6	71.254	-8.406	4	4
71.487	-10.164	2019:3:10	16:7:45.9	71.561	-10.243	2019:3:10	16:7:45.9	71.596	-10.155	4	4
71.144	-8.226	2019:3:11	20:27:12.2	71.194	-8.168	2019:3:11	20:27:12.2	71.197	-8.154	4	4
70.976	-6.433	2019:3:13	3:6:8.7	71.263	-6.223	2019:3:13	3:6:8.6	71.261	-6.200	4	4
71	-7.196	2019:3:13	21:47:52.6	71.124	-7.003	2019:3:13	21:47:52.4	71.113	-6.990	3	4
71.049	-6.488	2019:3:14	2:14:57.5	71.234	-6.271	2019:3:14	2:14:57.5	71.230	-6.263	4	4
71.126	-7.965	2019:3:14	22:57:55.8	71.134	-7.759	2019:3:14	22:57:55.8	71.138	-7.767	4	4
70.938	-7.004	2019:3:15	6:33:43.0	71.108	-6.728	2019:3:15	6:33:43.0	71.107	-6.722	4	4
71.198	-10.638	2019:3:15	11:18:58.4	71.403	-9.706	2019:3:15	11:18:58.4	71.405	-9.714	4	4
71.257	-11.245	2019:3:16	17:56:42.6	71.640	-10.753	2019:3:16	17:56:42.6	71.660	-10.701	4	4
71.258	-9.016	2019:3:19	7:3:33.7	71.331	-9.119	2019:3:19	7:3:33.5	71.353	-9.044	4	4
71.14	-8.212	2019:3:20	20:20:48.7	71.200	-8.173	2019:3:20	20:20:48.7	71.201	-8.167	4	4
71.007	-6.467	2019:3:25	12:44:43.6	71.234	-6.137	2019:3:25	12:44:43.6	71.239	-6.136	4	4
71.035	-7.424	2019:3:25	13:19:42.6	71.088	-7.393	2019:3:25	13:19:42.6	71.092	-7.398	4	4
71.148	-8.609	2019:3:31	23:38:21.3	71.198	-8.151	2019:3:31	23:38:21.2	71.195	-8.176	4	4
70.954	-6.805	2019:4:5	7:48:30.4	71.139	-6.658	2019:4:5	7:48:30.4	71.135	-6.681	4	4
71.123	-8.223	2019:4:6	10:5:53.6	71.179	-8.154	2019:4:6	10:5:53.6	71.168	-8.140	4	4
71.126	-8.361	2019:4:8	8:59:52.9	71.211	-8.309	2019:4:8	8:59:53.0	71.195	-8.329	3	3
71.021	-7.516	2019:4:9	16:19:11.3	71.091	-7.326	2019:4:9	16:19:11.3	71.095	-7.348	4	4
71.509	-10.422	2019:4:11	0:19:1.4	71.657	-10.738	2019:4:11	0:19:1.4	71.644	-10.788	4	4
71.016	-6.702	2019:4:11	21:13:46.0	71.221	-6.450	2019:4:11	21:13:46.0	71.222	-6.445	4	4
71.167	-8.353	2019:4:12	1:1:32.2	71.226	-8.326	2019:4:12	1:1:32.4	71.214	-8.287	4	4
71.182	-7.509	2019:4:12	8:50:55.1	71.147	-7.353	2019:4:12	8:50:55.1	71.349	-7.952	4	4
71.136	-7.726	2019:4:21	6:24:45.7	71.158	-7.519	2019:4:21	6:24:45.7	71.143	-7.509	4	4

71.216	-8.792	2019:4:28	0:58:24.3	71.287	-8.794	2019:4:28	0:58:24.1	71.268	-8.883	4	2
71.191	-8.704	2019:4:28	1:29:7.4	71.285	-8.844	2019:4:28	1:29:7.4	71.288	-8.853	4	3
71.264	-8.851	2019:4:28	1:29:42.2	71.290	-8.858	2019:4:28	1:29:42.2	71.284	-8.828	4	3
71.15	-7.792	2019:4:29	5:48:55.3	71.146	-7.686	2019:4:29	5:48:55.3	71.141	-7.706	4	4
71.236	-9.025	2019:4:29	10:40:18.4	71.312	-9.113	2019:4:29	10:40:18.4	71.318	-9.111	4	4
71.117	-8.86	2019:4:29	13:7:50.6	71.178	-8.948	2019:4:29	13:7:50.7	71.186	-8.884	4	4
70.955	-6.802	2019:5:4	13:24:54.2	71.127	-6.460	2019:5:4	13:24:54.2	71.125	-6.466	4	4
70.903	-6.825	2019:5:4	13:33:18.1	70.984	-6.494	2019:5:4	13:33:18.2	70.919	-6.520	3	3
71.422	-12.273	2019:5:6	12:42:37.1	71.094	-12.390	2019:5:6	12:42:38.3	71.091	-12.406	2	3
71.133	-7.97	2019:5:7	5:47:9.1	71.223	-8.017	2019:5:7	5:47:9.0	71.223	-8.047	3	4
71.747	-10.434	2019:5:7	12:45:53.2	71.902	-10.727	2019:5:7	12:45:53.8	71.626	-11.559	3	4
71.101	-7.482	2019:5:10	8:39:43.3	71.146	-7.348	2019:5:10	8:39:43.2	71.152	-7.370	4	4
70.704	-7.295	2019:5:11	23:9:32.6	70.760	-6.968	2019:5:11	23:9:32.8	70.762	-6.973	2	3
71.247	-9.126	2019:5:13	11:10:36.4	71.315	-9.273	2019:5:13	11:10:36.3	71.319	-9.248	4	4
71.328	-9.192	2019:5:13	14:16:51.0	71.313	-9.421	2019:5:13	14:16:51.0	71.310	-9.418	3	3
71.14	-8.438	2019:5:13	23:57:44.6	71.223	-8.423	2019:5:13	23:57:44.8	71.210	-8.362	3	3
71.063	-8.191	2019:5:14	3:0:48.2	71.075	-8.101	2019:5:14	3:0:48.2	71.092	-8.070	4	3
71.143	-8.076	2019:5:16	1:27:4.9	71.176	-7.962	2019:5:16	1:27:4.9	71.179	-7.982	4	4
71.048	-7.596	2019:5:16	1:52:37.8	71.117	-7.436	2019:5:16	1:52:37.7	71.112	-7.441	4	4
70.599	-8.397	2019:5:16	12:46:48.3	70.593	-8.159	2019:5:16	12:46:48.3	70.915	-7.208	3	2
71.11	-7.771	2019:5:17	8:5:15.8	71.111	-7.414	2019:5:17	8:5:15.8	71.105	-7.420	4	4
71.004	-7.277	2019:5:17	8:8:3.5	71.102	-7.425	2019:5:17	8:8:3.4	71.080	-7.402	4	4
71.98	-7.963	2019:5:17	14:53:18.9	72.013	-7.248	2019:5:17	14:53:18.9	72.007	-7.263	4	4
70.946	-6.808	2019:5:17	22:6:57.0	71.127	-6.513	2019:5:17	22:6:57.0	71.121	-6.494	4	4
71.041	-7.258	2019:5:18	2:54:19.3	71.156	-7.170	2019:5:18	2:54:19.5	71.175	-7.163	3	4
71.126	-8.631	2019:5:18	16:7:2.3	71.168	-8.740	2019:5:18	16:7:2.0	71.153	-8.762	3	4
71.294	-9.151	2019:5:19	9:4:54.0	71.324	-9.192	2019:5:19	9:4:54.0	71.320	-9.206	4	3
71.148	-8.235	2019:5:19	21:59:17.0	71.197	-8.170	2019:5:19	21:59:16.9	71.192	-9.201	4	4
71.013	-9.584	2019:5:24	21:26:35.6	70.986	-9.834	2019:5:24	21:26:35.6	71.010	-9.850	4	4
71.206	-8.805	2019:5:25	3:30:24.6	71.209	-8.259	2019:5:25	3:30:24.6	71.208	-8.240	3	3
71.194	-8.394	2019:5:25	13:55:45.2	71.244	-8.440	2019:5:25	13:55:45.2	71.232	-8.473	4	4
71.166	-8.41	2019:5:26	9:58:47.7	71.237	-8.454	2019:5:26	9:58:47.7	71.226	-8.404	4	4